Star-Forming Galaxies in the Epoch of Reionization

Silvio Lorenzoni

Department of Physics

University of Oxford

A thesis submitted for the degree of

Doctor of Philosophy

December 2012

To my parents and grandparents, my sister and Laura.

Abstract

This work presents a search for galaxies at $6.5 \lesssim z \lesssim 9.8$ based on the Lyman-break technique, using the latest *HST* WFC3 near-infrared data covering ~ 150 arcmin^2 of the GOODS-South field. With these data, it is possible to find sufficient $z \approx 7{-}9$ galaxies to fit both ϕ^* and M^* of the UV Schechter luminosity function. There is evidence for evolution in this luminosity function from $z = 6{-}7$ to $z = 8{-}9$, in the sense that there are fewer UV-bright galaxies at $z \approx 8 - 9$, consistent with an evolution mainly in M^*. The candidate $z \approx 7 - 9$ galaxies detected have insufficient ionizing flux to reionize the Universe, and it is probable that galaxies below our detection limit provide a significant UV contribution. The faint-end slope, α, is not well constrained. Adopting a similar faint-end slope to that determined at $z = 3 - 6$ ($\alpha = -1.7$), and a Salpeter initial mass function, reionization could be achieved at $z \approx 7$ for an escape fraction of ionizing photons $f_{\mathrm{esc}} = 0.5$ integrating the luminosity function down to $M_{UV} = -15$, while at $z \approx 8$, for the same f_{esc}, the ionizing photon budget still falls short even integrating down to $M_{UV} = -8$. A steeper faint end slope or a low-metallicity population (or a top-heavy IMF) might still provide sufficient photons for star-forming galaxies to reionize the Universe, but confirmation of this might have to await the *James Webb Space Telescope*.

Acknowledgements

I am extremely grateful to my supervisor Andy Bunker for his guidance, support, advice and especially for his patience throughout my Ph.D.

I would also like to thank Steve Wilkins for all the help he provided me. I am grateful to all the members of the ELIXIR network, and in particular Stephane Charlot, for the stimulating discussions during the frequent meetings and schools. Thanks to Joseph Caruana for his excellent company in the office and around Europe, and thanks to Taysun, Adam, Sun Jeong, Phil and Tessa for sharing the office (an my music...) with me, it was fun! I would like to thank the staff at Oxford Astrophysics, especially Ashling Morris and Vanessa Ferraro-Wood. Thanks to Fra, Amy and Francesco for the great company, and to all the other great students that I have met in this three years in Oxford.

To my parents, always supportive, and my loving sister. To Laura and her understanding and support.

My Ph.D. was funded by the Marie Curie Initial Training Network ELIXIR of the European Commission under contract PITN-GA-2008-214227.

Declaration

I declare that no part of this thesis has been accepted or is currently being submitted for any degree or diploma or certificate or any other qualification in this University or elsewhere.

This thesis is the result of my own work unless otherwise stated.

Some of the results I have published in Monthly Notices of the Royal Astronomical Society (MNRAS) as Lorenzoni et al. (2011 MNRAS 414, 1455) and Lorenzoni et al. (MNRAS, *in press*). Part of the data used in this work was reduced and analysed by S. Wilkins, and his results, published in Wilkins et al. (2011a), which I co-author, were used for successive interpretation.

Contents

Chapter 1

Introduction

The term Epoch of Reionization (EoR) refers to the period during which the gas in the Universe turned from almost completely neutral to almost completely ionized, between 150 million and one billion years after the Big Bang (corresponding to the redshift range $6 \lesssim z \lesssim 20$). This period saw the formation of the first stars and galaxies, that with their light contributed to the ionization of the neutral hydrogen that surrounded them. However, it is not clear how and when exactly this process took place and which was the primary source of ionizing photons. It is therefore of extreme interest to observe star-forming galaxies in the EoR, not only to assess their role in the reionization process, but also to acquire information on the evolution of galaxies, their star formation history and their luminosity function, and of the intergalactic medium (IGM) and the structures of the Universe.

1.1 Early stages of the Universe

To better understand the epoch of reionization, a brief “history of the Universe” is described here. The currently accepted theory is that of the hot Big Bang, according to which all the energy and matter that we now see (and even energy and matter that we do not see) was in an extremely hot and dense state, and started expanding and cooling. The expansion rate was extremely high during a short phase called inflation. After inflation, the expansion continued, although at a much lower rate. The continuing expansion obviously coincided with a drop in temperature, thanks to which the first fundamental particles gradually formed. With further decrease in temperature the strong interaction became enough to bond quarks into hadrons, including protons and neutrons, and successively into nuclei. At this stage, only a few minutes after the Big Bang, the temperature is still too high to allow electrons and nuclei to bond, leaving the charged particles free to interact with photons, whose mean free path is consequently short. This continues until about 380,000 years after the Big Bang ($z \approx 1100$), when temperature drops low enough to allow the formation of neutral atoms (recombination). Photons are then able to travel undisturbed forming what we now call the cosmic microwave background (CMB). Dark matter structures begin to form in the matter-dominated Universe, dragging hydrogen into dense regions, where it eventually collapses gravitationally to form the first stars and galaxies, at redshift $z = 20 - 30$. This starts the reionization process, which is over by $z \approx 6$ (see Figure 1.1).

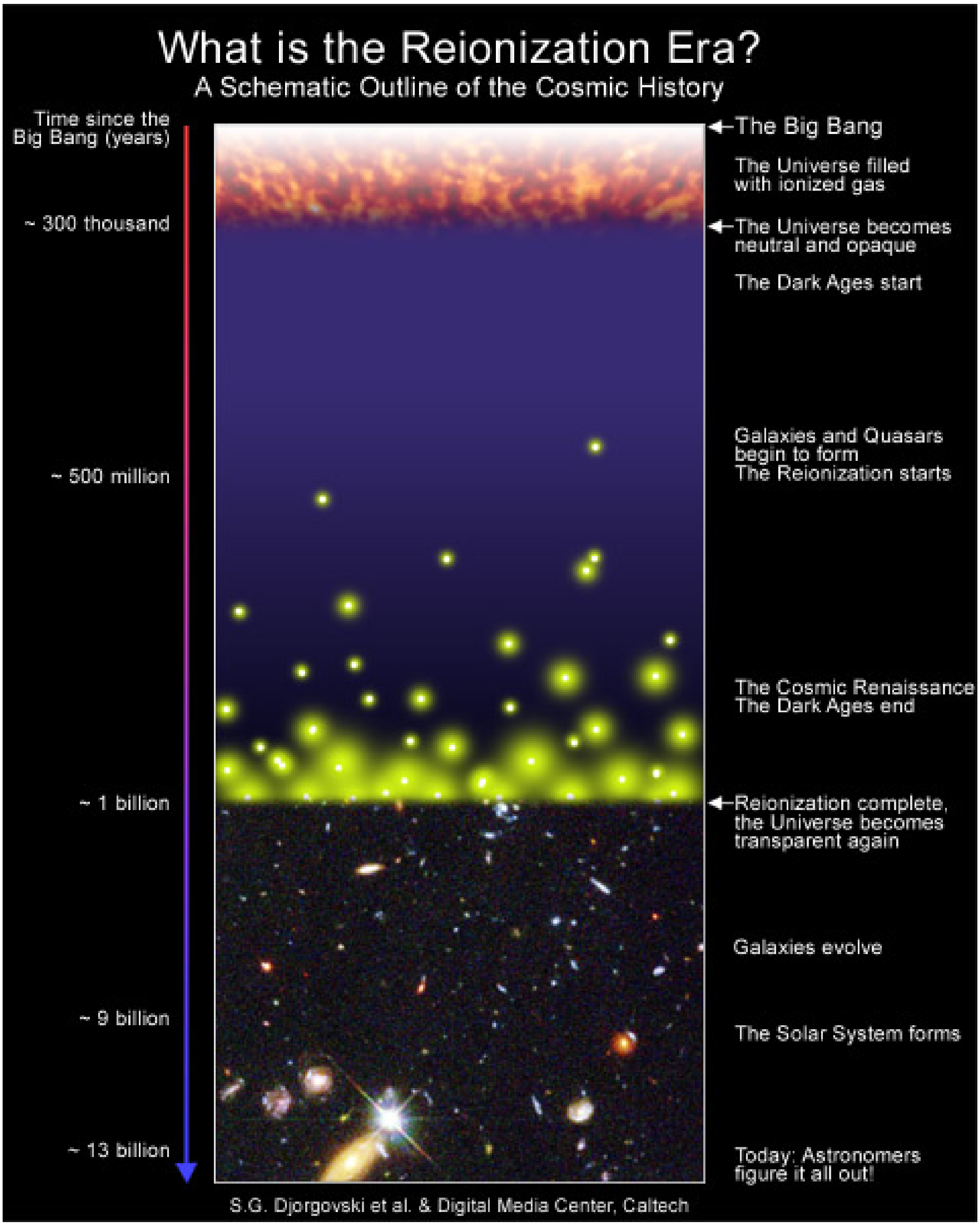

Figure 1.1: Figure credit Djorgovski (http://www.astro.caltech.edu/ george/reion/). Sketch of the history of the Universe.

1.2 The End of the Epoch of Reionization

It is still unclear when the process of reionization started, how long it lasted and what caused it, but strong evidence constraints its completion: The Gunn-Peterson trough (Gunn & Peterson 1965) has been observed in the spectra of quasars at redshift z = 6.28 and above (Becker et al. 2001, Fan et al. 2001, 2006). The Gunn-Peterson trough is the near total absorption of the continuum flux at wavelengths shorter than that of the Lyman-α, 1216 Å caused by the significant amount of neutral hydrogen present at those redshifts: intervening intergalactic clouds of neutral hydrogen along the line of sight absorb the radiation coming from distant galaxies[1], notably at the wavelength of Lyman-α at 1216Å, the $n = 2 \rightarrow n = 1$ transition of atomic hydrogen. Since these clouds are distributed at different distances from the observed galaxy, different sections of its redshifted spectrum are absorbed (Lyman-α forest, see Figure 1.2). When the neutral hydrogen is smoothly distributed along the line of sight (i.e. when the intergalactic medium, or IGM, is largely neutral), nearly all the photons with lower wavelength than that of Lyman-α are at some point absorbed.

Since a small neutral fraction ($X_{HI} \sim 10^{-4}$) is enough to cause complete absorption of Lyα photons, the observation of the Gunn-Peterson trough does not necessarily mean that the source is in the EoR, as towards the end of the reionization process the neutral hydrogen is not uniformly distributed and could be local. There is however evidence of strong evolution in the IGM neutral fraction around redshift $z \approx 6$: a study of 19 quasars of redshift $5.74 < z < 6.42$

---

[1] At wavelengths shortward of the ionization edge of hydrogen at 912Å(the Lyman limit) there is near-total absorption of light from objects over all redshifts due to intervening Lyman limit absorption systems, meaning that ionizing Lyman continuum photons have a short mean free path and are not observed directly.

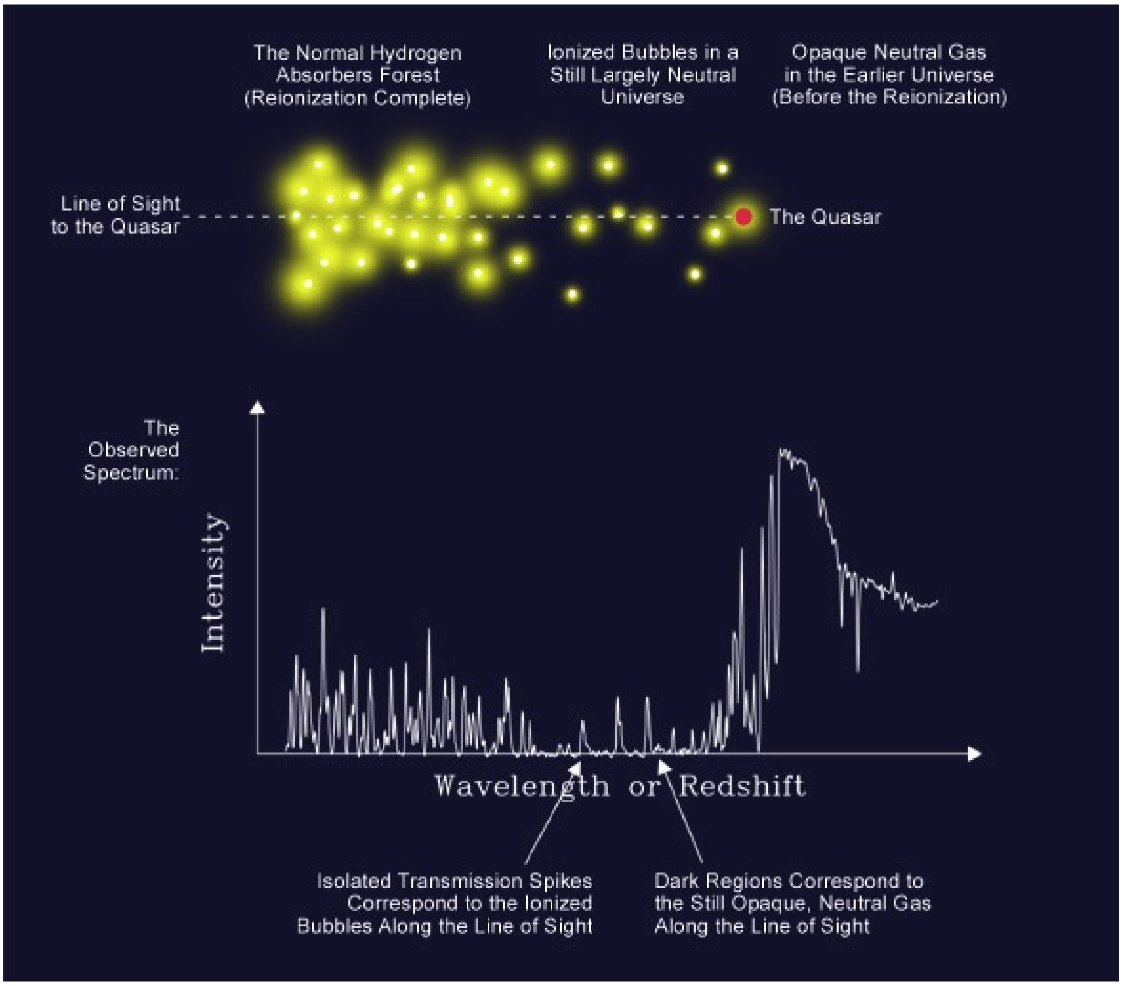

Figure 1.2: Figure credit Djorgovski (http://www.astro.caltech.edu/ george/reion/). QSO spectrum showing Lyman-α forest features due to the radiation absorption by intervening neutral hydrogen clouds.

by Fan et al. (2006) suggests a significant neutral fraction, $X_{HI} > 10^{-3}$, at $z \geq 6$, compared to a $X_{HI} < 10^{-4}$ at $z \sim 5.5$ (see Figure 1.3). These results suggest that given the rapid increase in neutral fraction around $z \approx 6$, if reionization was a sudden process it would have taken place not much earlier than that. However, WMAP data of CMB polarization constrains sudden reionization at $z \approx 11.0 \pm 1.4$ (Dunkley et al. 2009), excluding such a process at $z \approx 6$ at a 3.5σ level. The reionization process appears therefore to be rather slow and gradual, or at successive steps or even repeated (a first reionization followed by recombination and second reionization). This makes the extrapolation of the redshift at reionization from the measured optical depth τ very model-dependent and hence uncertain.

1.3 Galaxies in the Epoch of Reionization

Star-forming galaxies are the most likely candidates for the production of ionizing photons at high redshifts. Other sources like quasars or active galactic nuclei (AGN), even though contributing to reionization, are unlikely to provide enough ionizing photons by themselves (Madau, Haardt & Rees 1999; Bolton & Haehnelt 2007). The importance of high redshift galaxies is not limited to their role in reionization: the UV luminosity function (LF) and the star formation rate (SFR) and their stellar masses, along with the volume-averaged star formation rate density, are crucial quantities to measure if we are to monitor galaxy formation and evolution over cosmic time, and to compare with simulations to determine if our understanding of the physics is complete. The goal of this thesis is to discover candidate galaxies at redshifts $z = 7$ and beyond, and to determine their

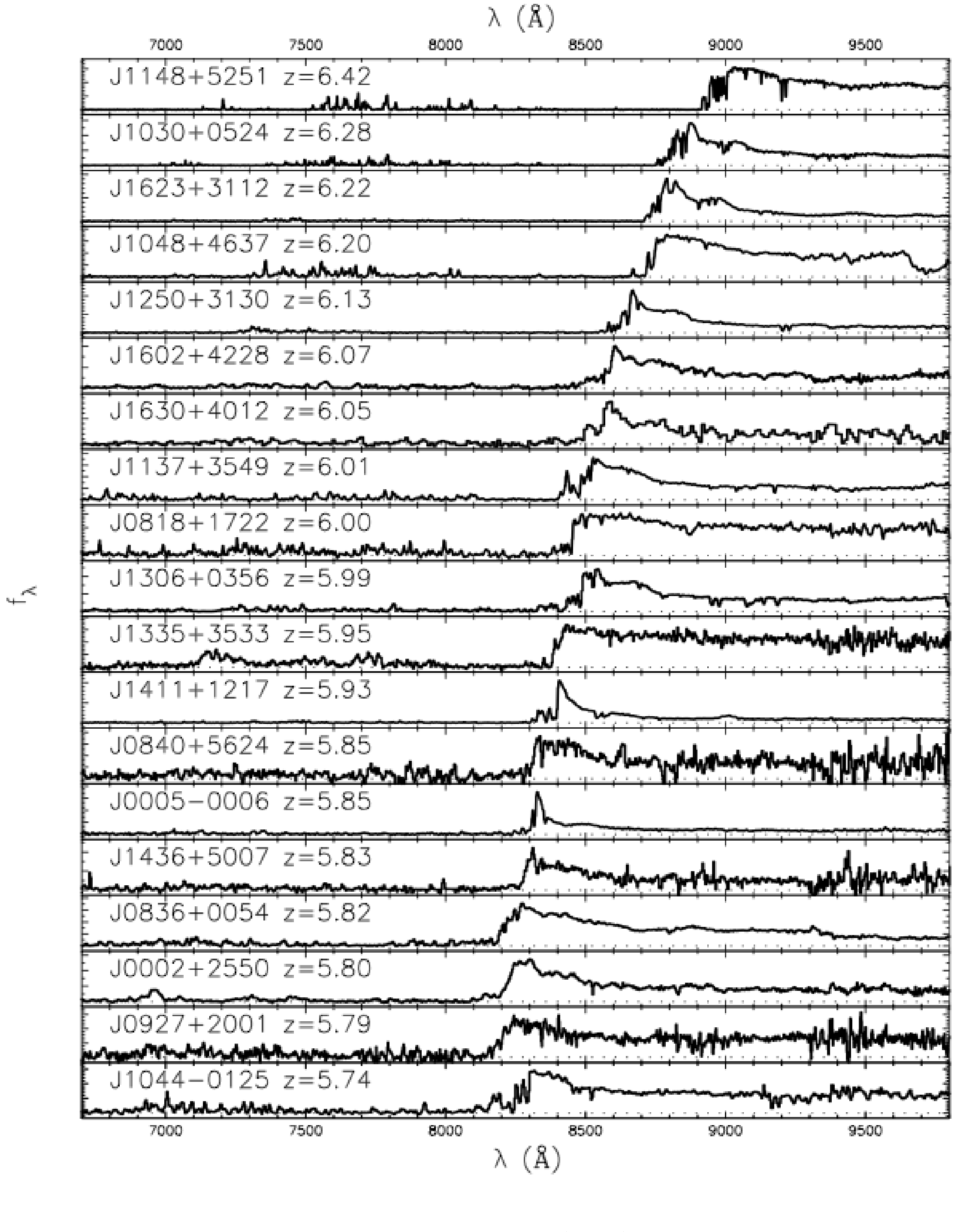

Figure 1.3: Figure and caption from Fan et al. (2006): Spectra of our sample of nineteen SDSS quasars at $5.74 < z < 6.42$. Twelve of the spectra were taken with Keck/ESI, while the others were observed with the MMT/Red Channel and Kitt Peak 4-meter/MARS spectrographs.

individual UV luminosities (and corresponding star formation rates) and study the overall characteristics of the galaxy population at this early epoch.

1.4 Observing High Redshift Galaxies

The detection and observation of high redshift galaxies is challenging: because of their extreme distances, they appear as extremely faint sources, even if their absolute magnitude is bright. There are a number of methods that have been used to search for these galaxies, with different degrees of success. Some have not been successful at $z > 7$ due to technical limitations of current observational data, such as AGN and Balmer break searches, while others are have produced outstanding results in the past few years and are described in detail here.

1.4.1 Lyman-break technique

This technique was initially used by Guhathakurta et al. (1990) to identify galaxies at redshift $z \approx 3$, unsuccessfully: none of the candidates identified were spectroscopically confirmed. The first successful Lyman-break galaxy (LBG) search was carried out by Steidel and collaborators (Steidel et al. 1996 and references therein), who identified many candidates that were spectroscopically confirmed shortly after, still for $z \approx 3$. Even if the Gunn-Peterson trough is not observed at these redshifts, an intrinsic drop in flux is expected at wavelengths shorter than that of the Lyman limit, 912 Å corresponding to the energy necessary to ionize neutral hydrogen, abundant in main sequence star atmospheres. This drop can be further enhanced by absorption from interstellar neutral hydrogen, likely to be abundant in young star-forming galaxies. Additional absorption between 912

Å and 1216 Å is produced by the intervening Lyman-α forest clouds. The attenuating effect due to the Lyman-α forest is of a factor of about 2 at $z \approx 3$ (Madau 1995) and becomes stronger with the increasing of redshift until we observe the Gunn-Peterson trough, at which point the break at 912 Å becomes unimportant because there is no flux below 1216 Å. The observed wavelength at which the break occurs is determined by the redshift of the source and lies in the optical for redshifts $2.5 \lesssim z \lesssim 6$ and in the near IR at higher redshifts. Identification of Lyman-break galaxies is achievable by broad-band imaging either side of the break: at wavelengths shorter than that of the break these galaxies will have a much lower flux than at higher wavelengths. This selection is subject to contamination by objects with a significant decrement in flux at a similar observed wavelength, as will be thoroughly described later on in section 3.2.1, and hence requires spectroscopic confirmation or detailed analysis to reject foreground objects through multi-waveband photometry of the candidates found.

1.4.2 Line Emission Narrow-band Searches

Another (recently) successful method is Lyman-α emission search by narrow band imaging. Lyman-α emission lines with rest frame equivalent widths of a few tens of Ångstroms, typical of Lyman break galaxies at $z \approx 3-6$ (e.g. Stanway et al. 2004), can be identified relatively easily with narrow-band ($\sim$ 100 Å) filters. Galaxies identified in this way are called Lyman-α emitters (LAEs). This technique is complementary with the Lyman break technique: given the smaller filter passbands, narrow-band imaging probes a much reduced redshift range, and hence smaller volumes, and is limited to objects that show bright Lyman-α

emission (Lyman-α emitters, LAEs hereafter). For the same reason, however, it is much more effective in finding cosmic structure, since all the detected objects are in a much narrower redshift range (Capak et al. 2011), and it is also effective for objects with a continuum emission much fainter than that observable with Lyman-break technique. This technique is heavily affected by contaminants, as many longer rest-wavelength lines at lower redshift (such as Hα) are likely to be detected. Broad-band imaging can rule out some lower redshift objects, but spectroscopic follow up is still necessary. The first searches with this technique date back to the early nineties (e.g. Pritchet & Hartwick 1990, Djorgovski & Thompson 1992) with no success, and following studies detected a small number of objects (Hu & McMahon 1996). The first substantial results (hundreds of candidates) with this technique came almost a decade later (Malhotra & Rhodes 2002, Ouchi et al. 2003). The relations between LAEs and LBGs are still unclear and under investigation.

1.4.3 Gamma Ray Bursts

Gamma-ray bursts (GRBs) are extremely powerful, rare and short lived gamma ray emissions associated with the death of massive stars (Woosley & Bloom 2006). A GRB is followed by an “afterglow”, successive emissions at longer wavelengths, from x-ray to optical, attributed to the interaction between the object causing the burst and the external environment. When a GRB is detected (in the higher atmosphere or from space, due to atmospheric attenuation), its afterglow is observed by other instruments at lower frequencies. Absorption features in the afterglow spectrum gives information on the redshift of the source and possibly on the IGM along the line of sight. The highest redshift object spectroscopically confirmed up to date is a GRB, GRB 090423, located at $z = 8.23$ (Tanvir et al. 2009), and other GRBs have confirmed redshifts of $z > 6$. However, follow-up observations of these objects have failed to identify their host galaxies, suggesting that such hosts are mainly galaxies beyond our present detection limits.

1.4.4 Application of the Lyman break technique to the EoR

The rest-frame far-UV spectra of star-forming galaxies at redshift $z > 2$ can be observed at optical wavelengths, allowing for the Lyman break technique to be used with ground-based telescopes. The first searches for Lyman-break galaxies (LBGs) by Guhathakurta et al. (1990) and Steidel & Hamilton (1992) employed a U-band filter centred at around 3600 Å and two filters at longer wavelengths, B_j and R; G and $\mathcal{R}$ respectively. With these sets of filters, objects whose flux drops in the U-band are easily identified: the U-band "dropouts", or more simply "U-drops", are galaxy candidates in the redshift range $2.5 \lesssim z \lesssim 3.5$. Later work by Steidel et al. (1996) identified a larger number of candidates from both ground- and space-based observations and was able to spectroscopically confirm many of them with the 10-m Keck telescope, while Madau et al. (1996) applied the technique using U_{300}, B_{450}, V_{606} and I_{814} images from the Wide Field Planetary Camera 2 (WFPC2) on the *Hubble Space Telescope* (*HST*) to identify U-drops and B-drops, at redshifts $z \approx 4$. Given these successes and the flexibility of this technique, more studies were conducted to increase the samples and to push it to higher redshifts, particularly after the Advanced Camera for Surveys (ACS) was mounted on the *HST* in March 2002. Its advanced technology and wider range of filters (i'_{775} and z'_{850} in particular) allowed a redshift range of $5.6 < z < 6.5$ to be reached by selecting i'-drops (Bunker et al. 2004, Bouwens et al. 2004), and along with large ground-based telescopes made the discovery of $z \approx 6$ almost routine.

The installation of Wide Field Camera 3 (WFC3) on the *HST* in Summer 2009 meant another major leap forward in the use of the Lyman-break technique, making the detection of galaxies at redshifts $z \geq 7$ possible with the infrared channel of WFC3 and led to the discovery of several galaxy candidates at $z \approx 7-10$ (Bunker et al. 2010, Wilkins et al. 2011a, Lorenzoni et al. 2011, Lorenzoni et al. 2012, Bouwens et al. 2011, Oesch et al. 2012b, Bradley et al. 2012; see Chapters 4 and 5). The Near Infrared Camera and Multi-Object Spectrometer (NICMOS), was already available on the *HST* before WFC3 (Bouwens et al. 2006 and 2007), however NICMOS had a smaller field of view and was less sensitive than WFC3. In addition, the filter closer to the optical available is J_{110} at 1.1μm, leaving a significant wavelength gap between the broadband images one could take. This gap is now closed thanks to the two broadband Y-band filters at $\approx 1.0\mu$m available in the WFC3.

This thesis is organised as follows: Chapter 2 briefly describes the data used (instruments and surveys) and analyses in detail the data reduction process. In Chapter 3 the candidate selection criteria and the reasons why they were chosen are shown, along with the resulting high-redshift galaxy candidates lists. Chapter 4 describes the derivation of the UV luminosity function, its evolution, and compares the results with other groups works. The implications for reionization are treated in Chapter 5. Throughout, we adopt the standard concordance cosmology of $\Omega_M = 0.3$, $\Omega_\Lambda = 0.7$ and use $H_0 = 70\,\mathrm{km\,s^{-1}\,Mpc^{-1}}$. All magnitudes are on the AB system (Oke & Gunn 1983).

Chapter 2

Observations and data reduction

In this chapter the instruments and the surveys used in the work that led to this thesis are briefly described, along with a detailed description of the data reduction process.

2.1 Instruments

The data reduced and analysed for this work come from two instrument mounted on the *HST*, ACS for optical data and WFC3 for the near infrared imaging.

2.1.1 Advanced Camera for Surveys

ACS is a third generation instrument mounted on *HST* in March 2002. The data used here are from the Wide Field Channel (WFC) whose field of view is $202'' \times 202''$, covering wavelengths from 3500 Å to 11000 Å with a plate scale of 0.05 arcsec/pixel. The detector is composed of two 2048×4096 pixels CCDs. ACS includes two other channels, the High Resolution Channel (HRC) and the Solar

Blind Channel (SBC). The former has a smaller ($29'' \times 26''$) field of view than WFC, covering a slightly wider (towards the near UV) wavelength range with a plate scale of 0.027 arcsec/pixel, and is no longer operational, while the latter is designed for UV observations, covering the 1150 to 1700 Å range with a field of view of $34.6'' \times 30.5''$ and plate scale of 0.032 arcsec/pixel.

2.1.2 Wide Field Camera 3

WFC3 is a fourth generation instrument installed on *HST* in May 2009, and comprises an infrared (IR) and an ultraviolet-visible (UVIS) channel. The IR channel detector is a Teledyne 1024×1024 pixel HgCdTe detector (a 100-pixel strip on the edge is not illuminated by sky and used for pedestal estimation), with a field of view of $123'' \times 136''$ and pixel scale of $0\overset{''}{.}13$. Unlike CCDs, which to read the charge generated from the collected photons shift it from pixel to pixel, the individual pixels of HgCdTe arrays are independent and can be read non-destructively, so it is possible to see the signal accumulating in each pixel during the course of an observation ("sampling up the ramp"). Repeated non-destructive readouts are also useful for the recovery of pixels hit by cosmic rays, as in that case two adjacent reads would result in a much larger jump in the electron counts than expected. The IR detector operates between 9000 and 17000 Å, an ideal range for the search of galaxies in the EoR: the Lyman-break from a source at $z \approx 8$ is expected to be seen at around 11000 Å. For this reason and for the pre-existing optical coverage of the fields observed, the data used here come from this channel. The UVIS channel uses the same detector package as the ACS/WFC channel, but with a smaller pixel scale (0.04 arcsec/pixel) for a total field of view of $162'' \times 162''$. It covers the range between 2000 and 10000 Å.

2.2 *HST* public surveys

Several surveys have been carried out for the search of Lyman-break galaxies, beginning with those made with WFPC2 briefly described in the introduction. Successive and more advanced surveys in the past decade include imaging with ACS and more recently with WFC3. For this work I have analysed a number of them covering the Hubble Ultra Deep Field (HUDF) and its two flanking fields (see Section 2.2.1), and the Great Observatories Origins Deep Survey (GOODS) South area, whose IR imaging with WFC3 has been carried out in two different programmes, the Early Release Science (ERS, see 2.2.2) and the Cosmic Assembly Near-infrared Deep Extragalactic Legacy Survey (CANDELS, see 2.2.3). See Figure 2.1 for the relative positions of these fields. The HUDF and its flanking fields have a limited area (4.2 arcmin^2 each) with deep coverage in both optical and IR, while the rest of the GOODS-South area (about $10' \times 15'$) has shallower non uniform imaging. Each programme involved in this work is described here.

2.2.1 HUDF and flanking fields

The Hubble Ultra Deep Field (HUDF) is an area selected for deep optical imaging with *HST*/ACS by Beckwith et al. (2006), centred on the coordinates R.A.: 3:32:39.0, Dec.: -27:47:29.1 (J2000). Its location was chosen for a number of reasons: maximise *HST* efficiency (long viewing periods, minimal Galactic absorption sources, mainly dust and neutral hydrogen), making it accessible to other astronomical observatories and overlap with observations (existent or planned at

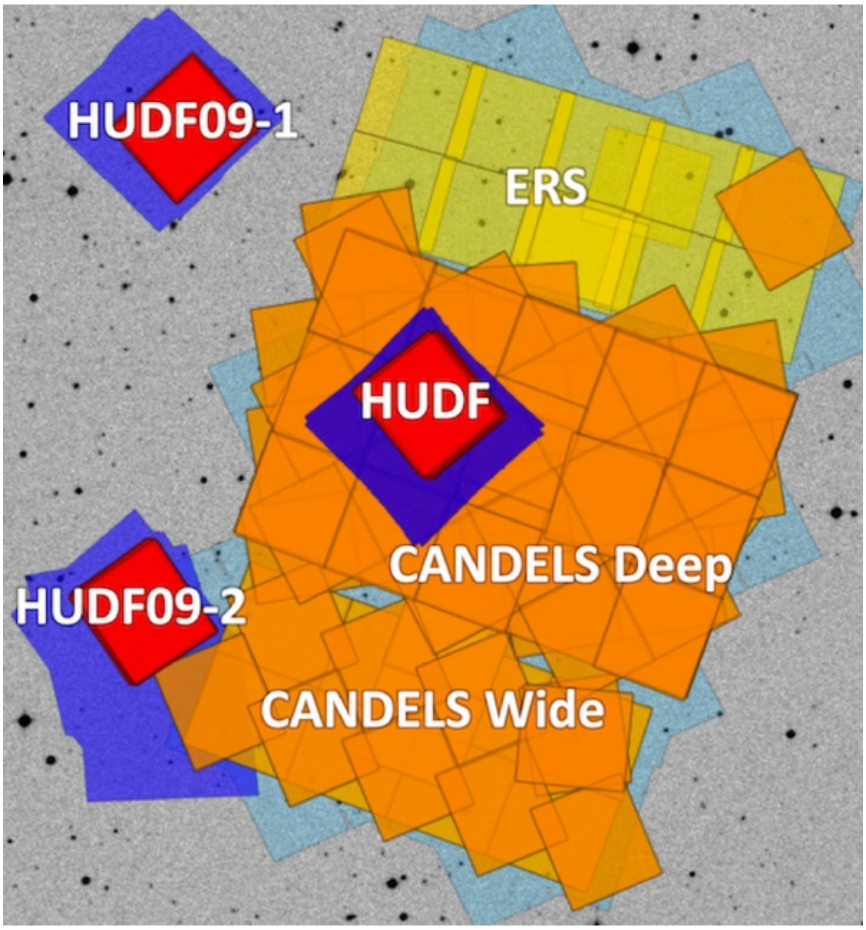

Figure 2.1: Figure from Oesch et al. (2012a). Fields used in this work in the GOODS-South area. ACS observations are marked with cyan for the GOODS-South and blue for HUDF and flanking fields. WFC3 observations are marked in yellow (ERS), orange (CANDELS) and red (HUDF, UDF-P12, UDF-P34)

the time) at different wavelengths. The *Chandra* Deep Field-South (CDF-S, Giacconi et al. 2002) satisfied these criteria, in particular it had already been observed in X-ray (with *Chandra* and *XMM-Newton*), optical (with ACS, Giavalisco et al. 2004) and in the infrared (with *Spitzer Space Telescope*, Dickinson et al. 2004). Observations were carried using the 4 filters F850LP (z'-band), F775W (i'-band), F606W (v-band), F435W (b-band), the same used for the GOODS-South observation (see section 2.2.2), to 10σ limiting magnitudes $m_{AB} \sim 29$ (calculated in an aperture of $0\farcs24$ diameter). These data cover an area of $200'' \times 200''$ (~ 11 arcmin^2) coinciding with ACS's field of view.

The infrared data used here come from the *HST* Treasury programme GO-11563 (P.I. G. Illingworth), which covers the HUDF and two nearby deep flanking fields (UDF-P12 and UDF-P34, also referred to as HUDF09-1 and HUDF09-2 in programme GO-11563) using the WFC3-IR filters F105W (Y-band), F125W (J-band) and F160W (H-band) to a similar depth to the ACS observations (see tables 1 and 2 for depths). This programme also includes parallel observations with ACS of these three deep fields in the v, i' and z' bands. The UDF-P12 and UDF-P34 fields were previously observed with the same ACS filters in the programme GO-10632 (P.I. M. Stiavelli) in 2005-6. These fields, with centres coordinates R.A.: 3:33:01.9, Dec.: -27:41:10 (J2000) and R.A.: 3:32:23.6, Dec.: -27:42:50 (J2000) respectively, were originally parallel fields observed with NICMOS while the HUDF was imaged with the ACS.

The WFC3 data were taken in MULTIACCUM mode using SPARSAMPLE100, which non-destructively reads the array every 100 seconds. There were two exposures per orbit, with each MULTIACCUM comprising 16 reads for a total duration of 1403 sec per exposure (see table 1). For the Y-band images of the HUDF, two visits (8 exposures) were severely affected by image persistence and were excluded from our data reduction.

A preliminary list of z'- and Y-drops in the HUDF only is presented on Bunker et al. (2010), while more complete inspections of all the three deep fields are described in Wilkins et al. (2011a) and Lorenzoni et al. (2011) for z'- and Y-drops respectively.

2.2.2 ERS

The Early Research Science programme (GO/DD-11359, P.I. R. OConnell) covers the northern area of the GOODS-S field with ten pointings for a total area of ~ 37 arcmin^2 at both UV and IR wavelengths with WFC3. The filters used for the IR channel are the same as in the Illingworth programme for J- and H-bands (F125W and F160W), while for the Y-band a slightly narrower filter was used, F098M, that does not overlap with F125W (while F105W does). The effect of this different filter selection is discussed in section 3.2. As for HUDF, SPARSAMPLE100 in MULTIACCUM mode was used. 3 exposures per orbit were taken, each with 9 or 10 reads corresponding to a total time of 803 or 903 s per exposure.

Optical observations of this region were part of the GOODS *Hubble* Treasury Programme (P.I. M. Giavalisco) and employed the filters that were used later by Beckwith et al. (2006) in their HUDF survey. 5σ depths measured in $0\farcs6$ diameter apertures, corrected for aperture loss and reddening as described in section 2.3, reach $m_{AB} \sim 28.0$ in the b- and v-bands, ~ 27.5 in the i-band and ~ 27.3 in the z'-band.

An analysis of the first 6 pointings for z'-drops at $z \approx 7$ was presented in Wilkins et al. (2011a), with the full ERS mosaic used to select z'-drops in Wilkins et al. (2011b). Y-drops from this data are presented in Lorenzoni et al. (2011).

2.2.3 CANDELS

The Cosmic Assembly Near-infrared Deep Extragalactic Legacy Survey (Grogin et al. 2011, Koekemoer et al. 2011) is a very extensive survey, currently underway,

	ACS/WFC3 2σ Detection Limits (AB magnitudes)							
Field ID	Area (sq.arcmin)	b_{435w}	v_{606w}	i_{775w}	z_{850lp}	$Y_{098m/105w}{}^{a}$	J_{125w}	H_{160w}
HUDF	4.2	30.3	30.7	30.6	30.0	29.65	29.70	29.67
P34	4.2	-	29.9	29.5	29.7	29.45	29.58	29.41
P12	4.2	-	29.9	29.6	29.6	29.16	29.50	28.23
ERS	37.0	29.1	29.1	28.5	28.4	28.02	28.39	28.10
CANDELS deep	62.9	29.1	29.1	28.5	28.4	28.77	28.29	28.16
CANDELS wide	32.8	29.1	29.1	28.5	28.4	27.79	27.90	27.57

$^{a}Y_{098m}$ for the ERS field and Y_{105w} for all the remaining fields.

Table 2.1: Summary of observations. All magnitudes are on the AB system, and measured in a $0\farcs6$-diameter aperture with an aperture correction applied to correct to approximate total flux (for compact sources), as described in the text.

that covers different areas of the sky to different depths and with different filters. It includes programmes GO-12060, 12061, 12062, 12063, 12064, 12440, 12442, 12443, 12444 and 12445 (P.I. S. Faber). The majority of the observation time is dedicated to the GOODS-South (completed) and -North (underway) fields, with the rest distributed in the wider fields COSMOS (Scoville et al. 2007), the Extended Groth Strip (EGS, Davis et al. 2007), and the UKIRT Infrared Deep Sky Survey (UKIDSS) Ultra-deep Survey field (UDS, Lawrence et al. 2007, Cirasuolo et al. 2007).

The main focus here is given to the GOODS-S observations, which have been used for this work. This field was defined by the GOODS *Hubble* Treasury Programme within the larger CDF-S, it covers a region of space of approximately $10' \times 16'$ and it is centred at the coordinates R.A.: 3:32:30, Dec.: -27:48:20 (J2000). It provides the optical *b*-, *v*-, *i*-, and *z*-band images used for our work.

The GOODS-S area not surveyed by the ERS is divided in two regions, a *Deep* region, consisting of 3×5 WFC3/IR tiles (~ 65 arcmin^2) where pre-existent *Spitzer* data are deeper, and a *Wide* region of ~ 34 arcmin^2 covered by 9 pointings. The filters used are the same IR filters used for the HUDF programme, plus shallow coverage with F350LP for supernovae discrimination. Parallel observations with ACS filters F814W, F850LP and F606W were also included in the programme. The IR depths (5σ) reach $m_{AB} \sim 27.5$ and 26.5 for *Deep* and *Wide* areas.

The strategy for the GOODS-N field is very similar to the one adopted for the GOODS-S, with a *Deep* central area and two *Wide* areas, with similar depths and the same filters. For the other wider fields, no Y-band observations are scheduled, making them less amenable for the search of redshfit $z \approx 7-9$ star forming galaxies.

2.2.4 Pure-Parallel Programmes

Pure-parallel programmes only include data taken from instruments that are not employed by the primary observation. Two of these programmes were designed for high redshift galaxies searches: the Brightest of Reionization Galaxies (BoRG, Trenti et al. 2011) and the Hubble Infrared Pure Parallel Imaging Extragalactic Survey (HIPPIES, Yan et al. 2011). Both programmes include random pointings at high galactic latitudes ($|b| > 30°$) and use the WFC3/IR filters used in the ERS observations, plus a UVIS v-band filter, F606W for BoRG, F600LP for HIPPIES. These kinds of surveys have some advantages: they are relatively ‘cheap’, as they use instruments’ ‘spare time’, cover a wide area (~ 274 arcmin^2 BoRG, ~ 123 arcmin^2 HIPPIES) and given the random nature of the pointings are virtually unaffected by cosmic variance. On the other hand, the imaged fields do not necessarily already have coverage in the optical bands, so that imaging in an optical band is required and the total exposure for each filter is reduced, resulting in observation whose depth is about half a magnitude shallower than the CANDELS *Wide* areas. The presence of only one optical band also leads to a heavier contamination of the sample. Other issues are the non uniform exposure times for different fields because of the different duration of the primary programmes, and the absence of dithering when such programmes are spectroscopic (which is the majority of the time). Data from these programmes were not used in this work, although we compare our results with those from the parallel-time surveys in section 4.3.

2.3 Data Reduction

Initially, the IRAF.STSDAS calibration pipeline `calwfc3` was used on each raw frame to calculate the count rate and reject cosmic rays through gradient fitting, as well as subtracting the zeroth read and flat-fielding, producing an `flt` image. The Space Telescope Science Institute (STScI) team applies the same pipeline and makes the results available, so this step has been skipped after thoroughly checking that the resulting files from both reductions coincide, working directly on the `flt` files. Analogously, IRAF.STSDAS pipeline `calacs` was used to process ACS raw frames (See Figure 2.2 for a comparison between ACS raw and `flt` frames). Each single `flt` file has two extensions: ‘sci’, which is the actual image of the sky, and ‘dq’, standing for data quality, a map of the bad pixels for that specific frame (this includes dead pixels, hot pixels and pixels affected by cosmic rays). As can be seen in Figure 2.2, a single `flt` frame looks far from ideal for science, however the final images include a number of frames varying from a few

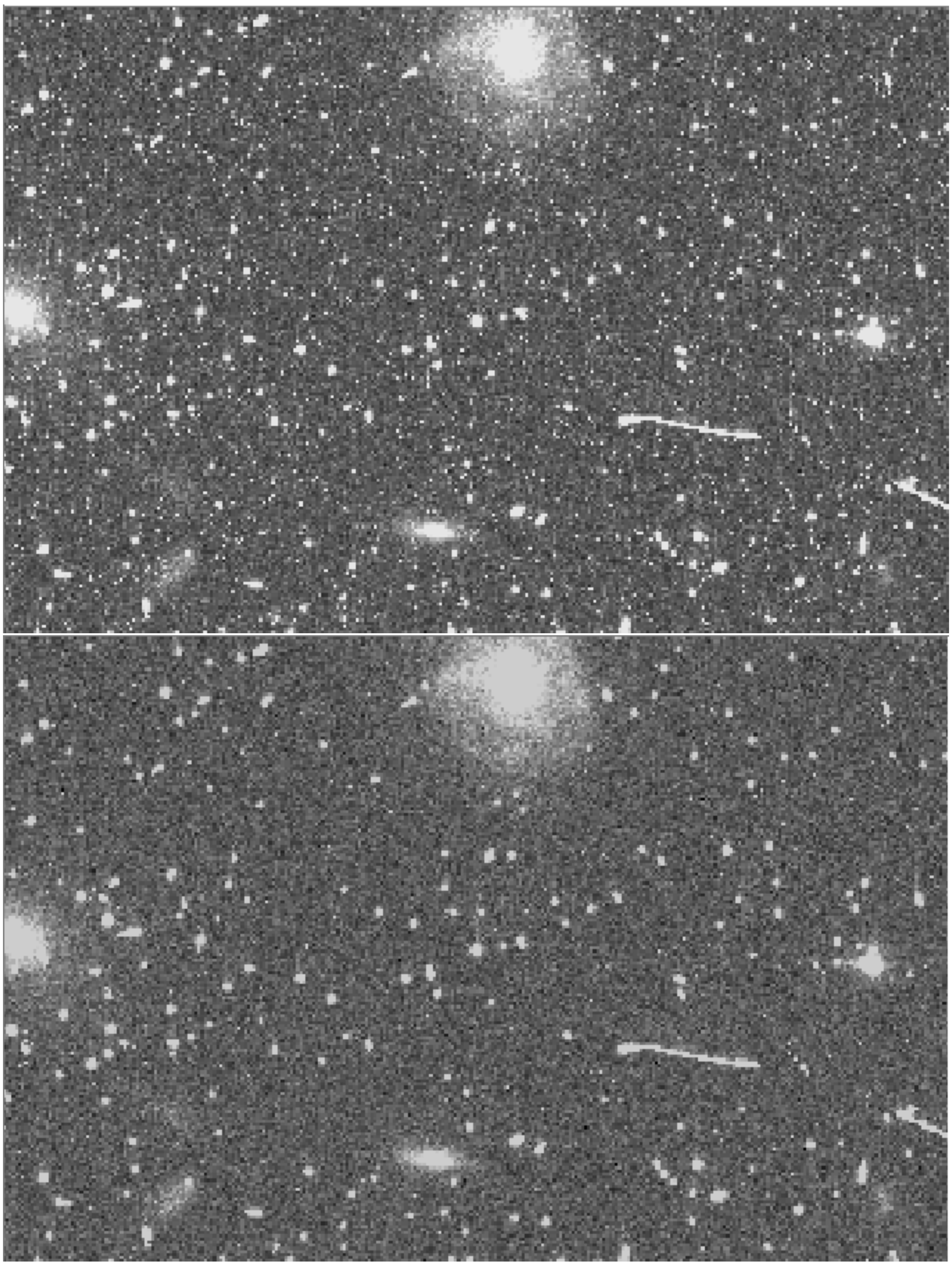

Figure 2.2: Differences between a raw (top) and a `flt` frame (bottom) from ACS: the calibrated `flt` frame background looks much smoother than that of the uncalibrated raw frame. Cosmic rays still affect the `flt` frames, and will be dealt with in successive steps (MULTIDRIZZLE, see text). Both images cover the same area of $\sim 14'' \times 10''$.

units to several tens. The individual exposures of a same area are taken with slightly different pointings, shifted by a small size compared to the total size of the detector. This process, referred to as dithering, avoids that the same bad pixels repeating on the same point in the sky, which would result in a loss of data. It also minimises the impact of flat-fielding errors and, if a sub-pixel dithering is applied, partially recovers information lost due to undersampling. The size of the shifts depends on the observed object and the detector used; for example the ACS dithering must take into account the strip between the two CCDs to avoid a portion of the sky getting no coverage at all.

2.3.1 MULTIDRIZZLE

We used MULTIDRIZZLE (Koekemoer et al. 2003), a PyRAF-based script, to combine the single exposures taken through the same filter in each pointing. While combining images, MULTIDRIZZLE eliminates geometric distortions, rejects cosmic rays and can also recover information lost because of undersampling (when the point spread function, PSF, has a size comparable to or smaller than the pixel size). For a visual representation of the effect of undersampling and of the drizzling process see Figure 2.3.

The code establishes an output grid whose parameters such as pixel size and orientation are set by the user. The input pixels are shrunk to a smaller size, determined by the parameter 'pixfrac' that can vary between 0 and 1, and overlapped onto the output grid (see Figure 2.4). The flux value of each shrunk input pixel, or "drop", is distributed to the corresponding smaller output pixels with weights proportional to the area of overlap between them. A pixfrac value of

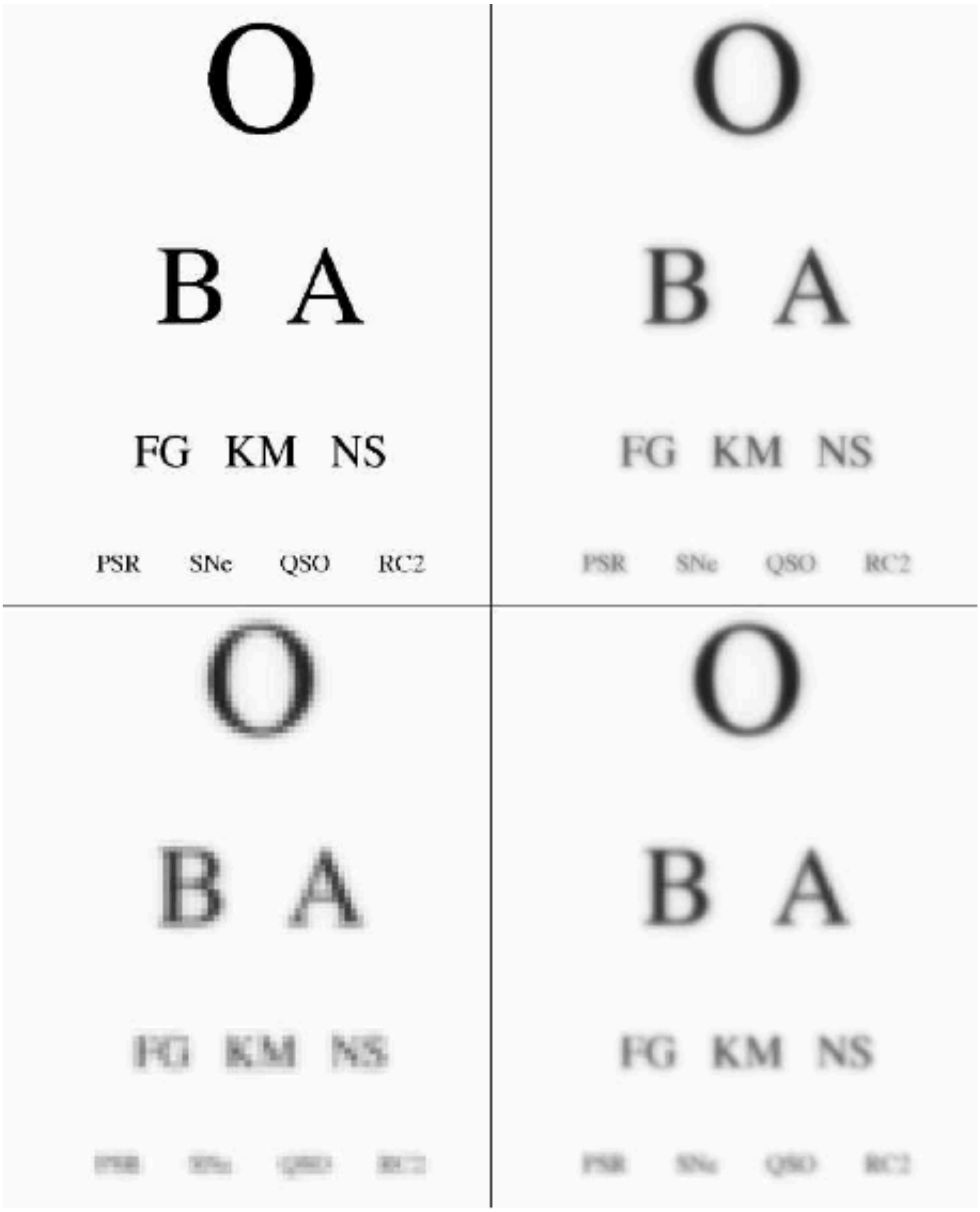

Figure 2.3: Figure from Fruchter & Hook (1997). Upper left corner shows the "true image", *i.e.* the image one would see with an infinitely large telescope. The upper right shows the image after convolution with the telescope's optics. The lower left shows the image after CCD sampling, and the lower right shows a linear reconstruction of dithered CCD images.

1 would mean that the input pixels are not shrunk at all and just distributed onto the output grid, so that the image would not improve its spatial resolution, while a value of zero would concentrate each pixel's information in one point. In this case, the finer output pixel grid would not be completely populated and the resulting image would show a number of blank pixels. It is therefore important to choose a suitable "drop" size for the data being processed with MULTIDRIZZLE. The output image has 2 extensions, a 'sci' image, which is the actual image of the sky used for science, and a 'wht' (weight) image, generated from the 'dq' extensions of the `flt` frames, which carries the relative weight of the output pixels and can also be used as an exposure map and to determine the actual quality of the scientific image: the latter can in fact look reasonably good even if the registration of the frames is not perfect, but the wht image would not appear smooth at the spatial locations corresponding to bright objects, where a smudge can be seen (Figure 2.6).

To obtain deep images it is necessary to stack many frames, generally taken during different orbits. The *HST* pointing accuracy varies from $\sim 0\farcs002 - 0\farcs005$ within a single orbit to $\sim 0\farcs005 - 0\farcs020$ in case of target reacquisition for successive orbits in the same visit (Gilliland 2005). Between different visits, using the same guide targets with the same angular orientation, precision is about $\sim 0\farcs05 - 0\farcs10$, comparable to the ACS pixel scale. When a large number of parallel observations is included in the data, like in the case of HUDF and its flanking fields, it is likely to have different observation angles in different visits, while for wider programmes like ERS the different pointings might have relied on different guide-stars. Both cases can result in an offset of several pixels for the same object in different frames.

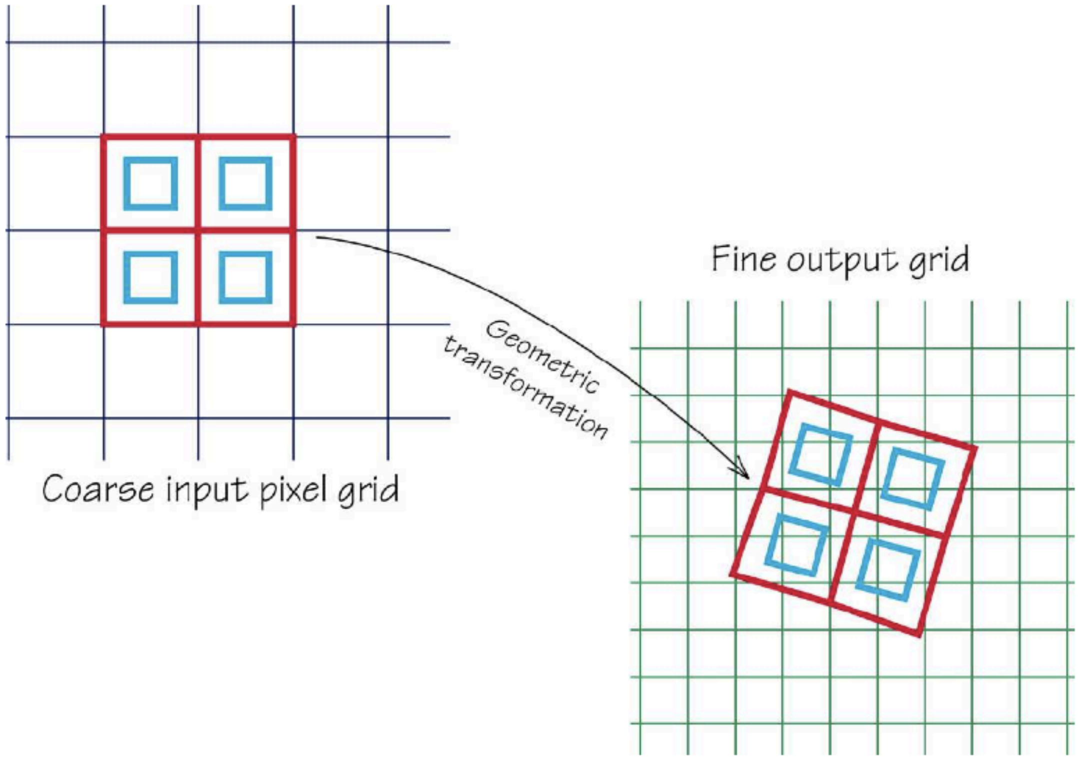

Figure 2.4: Figure from Fruchter & Hook (1997). Schematic representaion of drizzling: the pixels of the original grid (red) are shrunk (cyan) and projected onto a finer output grid.

2.3.2 Data reduction pipeline

It is crucial to determine these pointing inaccuracies between the frames before stacking them with MULTIDRIZZLE, and given the very faint nature of the objects we are looking for, a sub-pixel precision registration is needed. Several IRAF routines are used to evaluate the inter-frame shifts; the basic idea is to measure the position of a certain number of objects from a reference image, identify those objects in all the other single frames and measure the average coordinates shift for each frame. The best option for the reference image is to use the result of a first plain "drizzling" of the frames. This works if the shifts between the frames are small (one pixel or less) and the resulting multidrizzled image is of decent quality. If the shifts are larger, the resulting image is blurred (see Figure 2.5, top panel) and the coordinates of the objects measured on it would not be the correct ones. The list of coordinates used as reference is created using the IRAF task `daofind` and generally includes from several tens to a few hundred objects. The IRAF task `center` searches an image for objects within a certain radius (set by the user) from a list of given coordinates, and returns the centre coordinates of the objects in that image. This routine is used on intermediate products of the MULTIDRIZZLE process, the “single_sci” images: each of these images correspond to a single `flt` frame corrected for distortion and cosmic rays, and oriented like the final multidrizzled image.

If the shifts between the single frames are too high (a few pixels) to obtain a good stacked image with a first run, one of the “single_sci” resulting images can be used. However, the quality of these images is proportional to the number of frames involved in the MULTIDRIZZLE process because of better cosmic ray rejection: if only a few (less than 5) frames are stacked, the “single_sci” images can still present some cosmic rays that can be picked up as sources from `daofind`. In this case, an already reduced image of the same field (usually in a different spectral band) can be used to determine the list of references.

The average coordinates difference between each single image and the reference image can then be easily calculated (IRAF task `geomap` is used here), giving the relative shift between the single frames as a result. MULTIDRIZZLE allows for a shift file to be entered as input, however there have been several times when this shift file did not appear to work. To avoid any malfunction, instead of entering a shift file, the central coordinates in the header of the single frames are

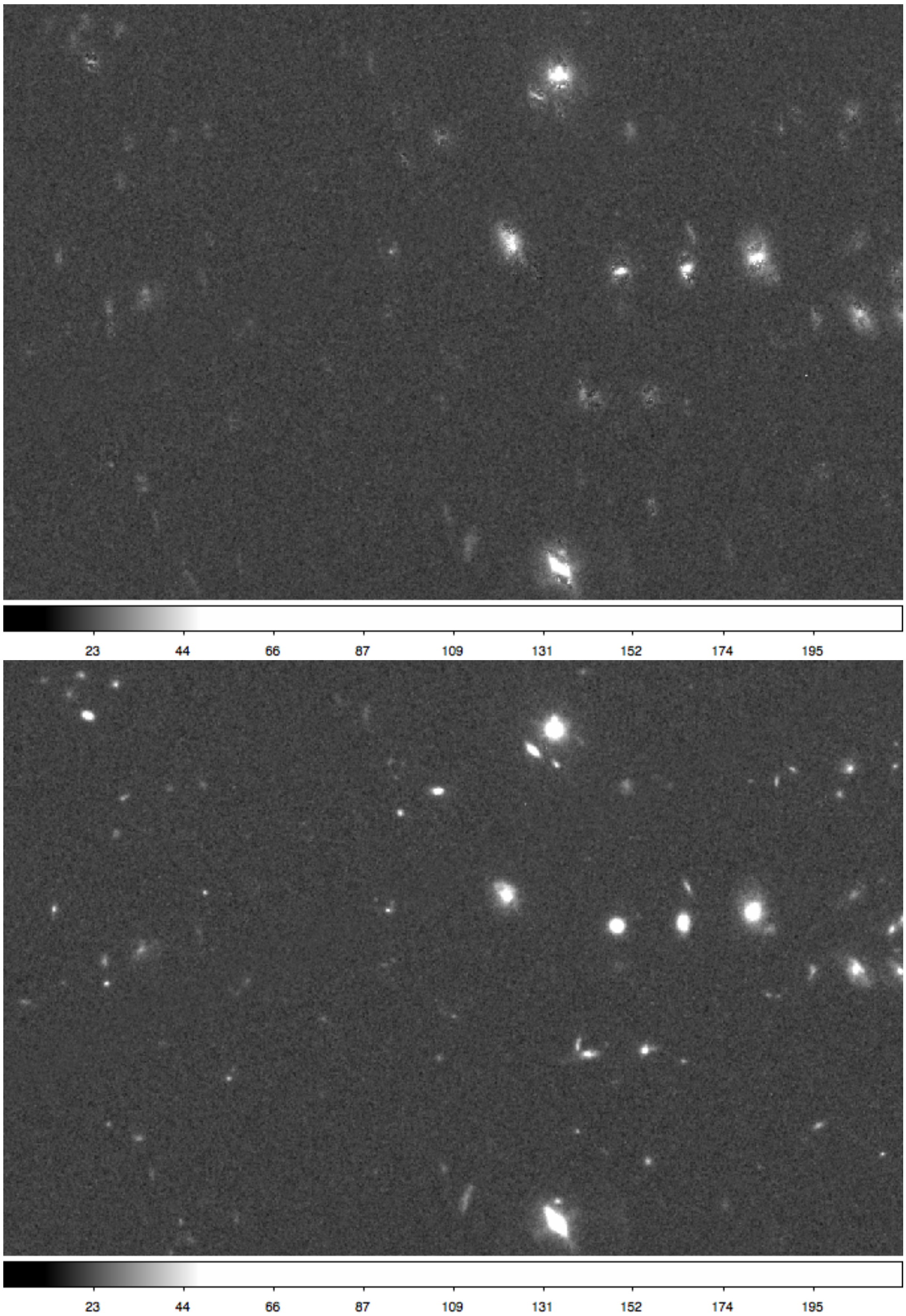

Figure 2.5: Top panel: drizzle output with no correction for the inter-frame shifts of the order of a few pixels. Bright objects profiles are not well defined, while fainter ones just appear as diffuse objects. Bottom panel: drizzle output obtained from the same frames as the top panel, corrected for shifts. Images size is $\sim 60'' \times 36''$.

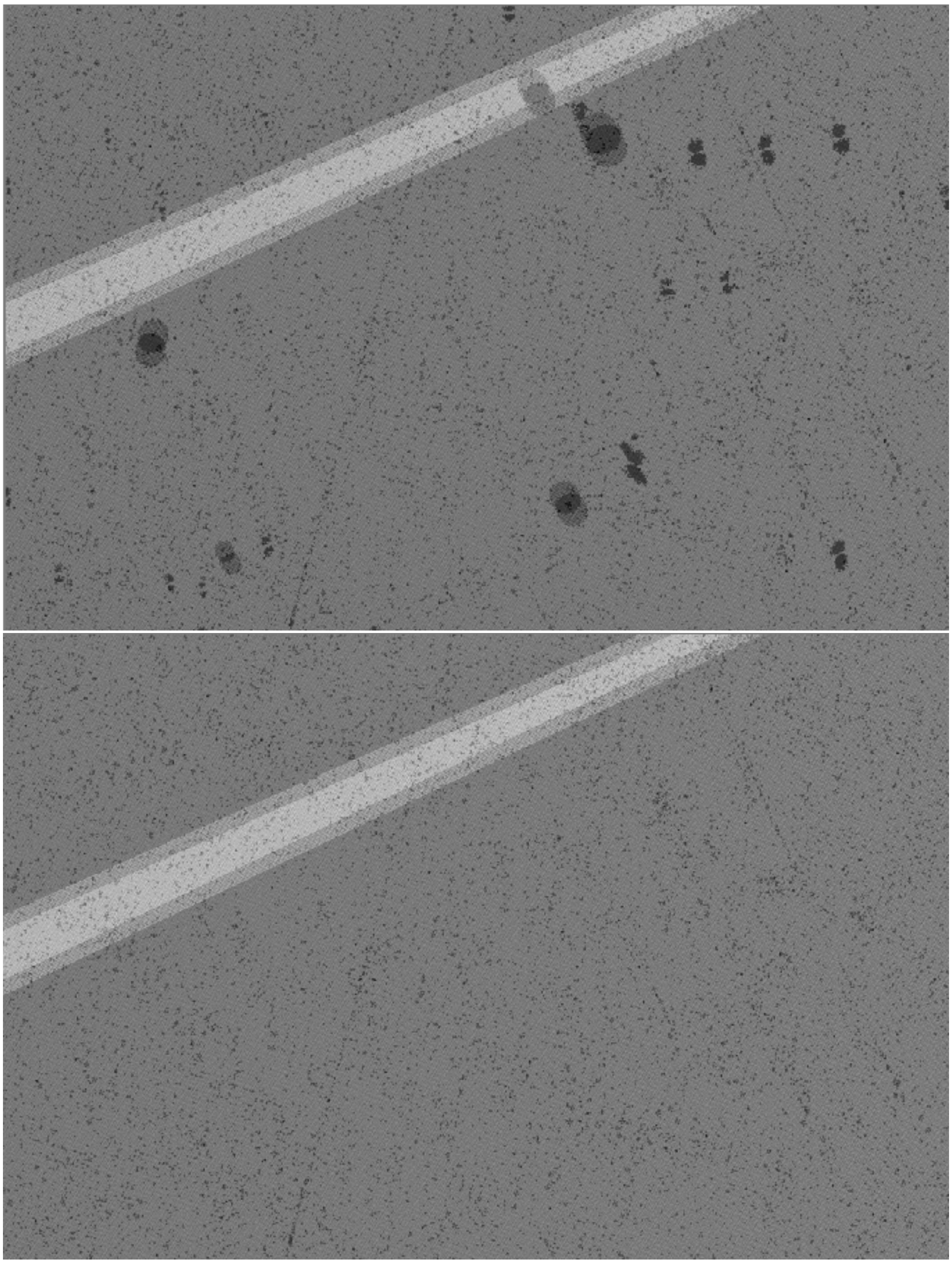

Figure 2.6: Weight images corresponding to the ‘sci’ images in Figure 2.5. Top panel: wht image from a drizzling with no shift correction. Typical patterns due to poor registration can be seen as shadows across the image. The perfectly circular dark areas correspond to a circular masking in the ‘sci’ image. The white stripe is the overlap between two sets of frames with different (adjacent) pointings. Bottom panel: image from a drizzling with shift correction. The absence of shadows implies a correct alignment of the contributing frames.

modified by the opposite of the calculated shift. Processing these altered frames with MULTIDRIZZLE should now result in a perfectly registered image, although some iterations of this process can be required, especially when the starting shifts are large. At the end of the process, the weight image will be smooth and without smudges due to poor registration (with the only exception of very bright objects, especially those with diffraction spikes). Figures 2.5 (‘sci’) and 2.6 (‘wht’) show the difference between MULTIDRIZZLE outputs not corrected for frames shift (top panels) and corrected for the shift (bottom panels).

To successfully use the Lyman-break technique it is very important that the IR images are registered with extreme precision (sub-pixel) to the optical images, which in this case are the GOODSv2.0 ACS drizzled images. To achieve such precision, the shift between the ACS and WFC3 images is calculated in an analogous way as the inter-frame shifts, and it is then subtracted from the central coordinates of the multidrizzled image: the resulting coordinates are imposed as new central coordinates for a final MULTIDRIZZLE run.

Another problem for a correct registration of optical and IR images is given, especially for the data collected in the first months of activity of WFC3, by a rotation offset between the two sets of images. If this offset is present, it is usually of a few decimals of degree, and the rotation angle can be easily calculated by `geomap` along with the shifts between the images. This angle is added to the input list for the last MULTIDRIZZLE run.

As we have just seen, at least three MULTIDRIZZLE runs and the use of several IRAF routines are necessary for each pointing and for each spectral band. MULTIDRIZZLE can require up to a couple of hours to run if many frames are processed, it is therefore advisable to minimise the interactions with the reduction process. In order to do that, I created a PYTHON script that calls the needed IRAF routines and performs the desired calculations. There are two versions of this script, `drizzler.py` and `shifter.py`. The first is used to stack frames from a single pointing (HUDF and flanking fields) and follows the procedure just described, and is easily adaptable to the ERS observations: the ERS area is in fact covered by ten distinct adjacent pointings, with each exposure of a certain pointing (also called ‘tile’) taken during the same visit (in two consecutive orbits). It is therefore reasonable to stack the frames of each pointing and then combine the results together. CANDELS observation strategy is different: each visit covers the whole field (either GOODS-S *Wide* or *Deep*), and since ACS and WFC3 are used at the same time, the observation angle of the main target varies according to the areas to be covered by the parallel observation. As a result, the tiles covering the field have different centres each visit and cannot be isolated in pointing groups like in the ERS case. Combining all the tiles from each visit together is not advisable, as a large total area heavily affects the run time of MULTIDRIZZLE and the corrections for pointing inaccuracy would be much more difficult. The adopted data reduction strategy is to combine together all the frames overlapping an ACS tile. The `shifter.py` script is modified to automatically select the WFC3 tiles to be ‘drizzled’ given a certain ACS tile, before running the procedure. This is easily done by reading the central coordinates of each WFC3 tile in the database and selecting those whose centre is within a certain distance from the centre of the ACS tile. Beside this addition, there are two other main differences in these script: the reference image used to register the frames, and a loop on the shift evaluation procedure. Both these variations are due to the high shifts (up to ten pixels) between the frames, a consequence of the observation strategy (as the pointing precision decreases for frames taken in different visits). These shifts make a plain (with no attention taken to the shifts) 'drizzle' useless as the resulting image is not suitable for the detection of reference objects (see Figure 2.5, top panel). The use of one of the 'single_sci' files is also not possible for different reasons: if the resulting multidrizzled image is flawed, the intermediate images generated in the process are also flawed, and even if they were reasonably good, there would be an incomplete overlap (or no overlap at all) between the different frames to stack, and a list generated from a single tile would not cover all the others. For these reasons, the list of reference objects is taken from the ACS tiles (z'-band). Since many of the combined frames lie mostly outside of the ACS tile of interest, objects from ACS tiles adjacent to it must be included in the list, that can include up to more than a thousand objects. These big shifts are also difficult to exactly quantify with a single measurement, so the procedure is iterated: the original reference object grid is shifted by the amount found with the first iteration, shifts from this new grids are calculated and added to the first ones, and so on. Usually, two iterations are enough to obtain a registration within 0.15 pixels, but sometimes three or four are necessary to reach this precision.

The new WFC3 images of fields HUDF, UDF-P12 and UDF-P34 were reduced using the latest version of `calwfc3` (29 October 2009 release). An earlier reduction of the HUDF WFC3 images was presented in Bunker et al. (2010), where the WFC3 pixels were split into a 3×3 grid and the frames were shifted and added, and fits to the geometric distortion were used, due to MULTIDRIZZLE not then being available for the newly-commissioned WFC3. For the UDF and flanking fields, we used a pixel fraction of 0.6 to recover some of the undersampling. In each of these three fields we survey 4.18 arcmin^2 in all exposures, with another 0.67

arcmin^2 surveyed at half the maximum depth in each field. For the ERS project, a pixfrac of 1 was used because of the small number (6) of frames per pointing. The ten different pointings in each filter were then mosaicked together, using inverse-variance weighting for the overlap regions (i.e. weighting each pixel by its exposure time), producing a field of fairly uniform depth covering 37 arcmin^2, with a further 8 arcmin^2 going less deep. CANDELS data were 'drizzled' with a pixfrac of 0.8 for the *Deep* and 1.0 for the *Wide* area. We used our own reduction of all the WFC3 data for the CANDELS GOODS-S *Wide* area and of the Y-band data of the *Deep* region. For the J- and H-bands covering the *Deep*, we used the reduced single epoch images made available by the CANDELS team[1] and co-added these together with inverse variance weighting. The resulting areas are 65.0 arcmin^2 and 34.4 arcmin^2 for *Deep* and *Wide*, respectively.

All the WFC3 data used for this work were combined with MULTIDRIZZLE to an output pixel size of $0.''06$ from the original $0.''13\,\mathrm{pix}^{-1}$, which corresponds to a 2×2 block-averaging of the GOODSv2.0 ACS drizzled images in b-, v-, i- and z'-band. In our final combined HUDF J-band image, we measure a FWHM of $\approx 0.''1$ for point sources in the field.

For the optical *HST* ACS data, publicly-available reductions of b, v, i, z' bands were used for the HUDF (Beckwith et al. 2006), the GOODS-South (GOODSv2.0 ACS from the GOODS team) and flanking field UDF-P12 (provided by the UDF05 team, Oesch et al. 2007). We reduced the v, i, z ACS data for UDF-P34 from the *HST* archive, using MULTIDRIZZLE to combine a large subset of the data comprising blocks of data taken close in time with similar telescope roll angles, using an output $0.''03$ pixel scale. These subsets of drizzled images were

---

[1] See `http://candels.ucolick.org/data_access/GOODS-S.html`

then registered and combined with `IRAF.imcombine`. All the ACS images were then block-averaged 2×2, resulting in a $0\farcs06$ pixel scale, and registered with our drizzled WFC3 frames.

2.3.3 Aperture photometry

As most high-redshift galaxies are likely to be barely resolved (e.g., Bunker et al. 2004, Ferguson et al. 2004) we measure the flux of the sources with circular apertures centred on the objects. The determination of the aperture's size has to consider two main factors: the aperture should be large enough to enclose a significant fraction of the flux, but should also be small enough to limit the sky background noise (and to avoid flux contamination from other objects). Assuming point sources, their point spread function (PSF) is approximated by a gaussian profile, whose standard deviation σ is related to the FWHM by the relation FWHM= $2\sqrt{2ln2}\,\sigma \approx 2.355\sigma$. The fraction of flux enclosed in an aperture as a function of the aperture radius is shown in Figure 2.7 (left panel): for an aperture diameter of 2×FWHM, more than 90% of the flux is collected, and virtually all the flux is enclosed in 3×FWHM diameter apertures, therefore a larger aperture would not improve the signal, already at its maximum, but it would include more sky background increasing the noise, which grows linearly with the aperture radius. As we can see in Figure 2.7(right panel), S/N has a maximum for apertures with a diameter of 1.34×FWHM (or a 1.58σ radius), including $\sim 72\%$ of the total flux. Since the average FWHM measured for point sources in our IR data is of $\approx 0\farcs15$ (in the H-band), an aperture of $0\farcs15$ diameter would seem ideal. However, we cannot assume that our targets are point sources,

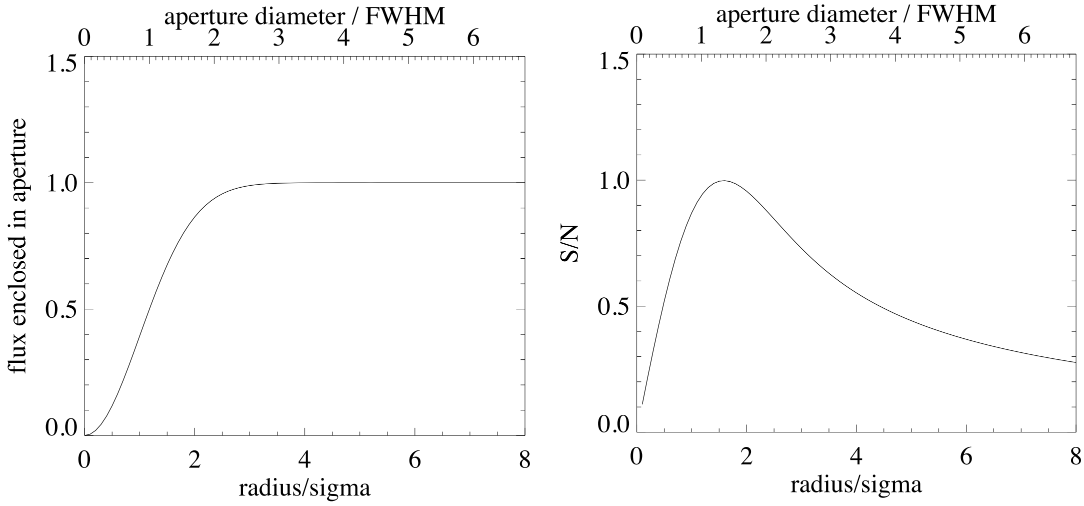

Figure 2.7: Left panel shows the fraction of flux from a gaussian PSF enclosed in an aperture as a function of the aperture radius. Right panel shows the normalised signal to noise ratio as a function of aperture radius in a sky background noise dominated regime.

so the actual PSF will depend on the spatial profile and the size of the object . To allow for larger FWHM, we chose an aperture diameter of $0\farcs6$, corresponding to 10 pixels on our images.

To correct for the loss of flux, we apply an aperture correction, a magnitude value to be subtracted from the magnitudes measured in apertures. The value of this correction can be found measuring the difference between the total flux and the aperture flux of several bright but unsaturated point sources, relatively isolated in the images, for each spectral band. The correction was determined to be ≈ 0.2 mag for our WFC3 Y-band images and ≈ 0.25 mag for J- and H-band. We note that the H-band images display significant Airy diffraction rings around point sources. For the ACS images, the better resolution and finer pixel sampling require a smaller aperture correction of ≈ 0.1 mag. All the magnitudes reported in this thesis have been corrected to approximate total magnitudes (valid for compact sources), and we have also corrected for the small amount of foreground Galactic extinction toward these fields using the *COBE*/DIRBE & *IRAS*/ISSA dust maps of Schlegel, Finkbeiner & Davis (1998). The optical reddening is $E(B-V) = 0.009$, equivalent to extinctions of $A_{850lp} = 0.012$, $A_{105w} = 0.010$, $A_{125w} = 0.008$ & $A_{160w} = 0.005$.

2.3.4 Noise

As in the case with CCDs, the counts received by HgCdTe detectors are subject to different kinds of noise: photon shot noise, intrinsic in the photon detection process and governed by Poisson statistics; dark noise, due to electrons generated by thermal processes, Poissonian; read out noise, produced in the conversion from analog to digital numbers, time independent. These noises are uncorrelated and can hence be combined in quadrature to obtain the total noise. However, the geometric transformation and image re-gridding described earlier produce an output where a pixel is not independent from all the others: the signal allocated to it comes from different pixels of the input images, and fractions of these pixels can also contribute to the signal in adjacent output pixels. The signal is therefore correlated and measuring the standard deviation in blank areas of the final drizzled image will underestimate the noise.

To ascertain the true significance of object detections, the real noise is determined using several different techniques. A crude combination of the individual flat-fielded images using integer-pixel shifts was produced. While this was not used for our science (as the significant geometric distortions were not accounted for, and it did not address the under-sampling of the PSF as “drizzle” does), this output frame has the advantage that the noise properties are preserved and adjacent pixels were uncorrelated. The limiting magnitudes found using these uncorrelated "true-noise frames" are in good agreement with the STScI *HST*/WFC3 Exposure Time Calculator (ETC) – Table 2.1 presents our $2\,\sigma$ limits in a 0.″6-diameter aperture, with the aperture correction applied.

The decreasing of the of the noise (normalized per unit time) as the square root of the number of frames combined was verified by measuring the standard deviation of the counts in blank areas of sky in this shift-and-add mosaic and of single `flt` images.

A more complete noise model based on the detector gain (the conversion between electrons accumulated and counts recorded by the detector), readout noise and Poisson counts of the measured background (including the instrument dark current) was also produced:

$$\sigma_{e^-} = \sqrt{N_{ro}^2 + N_P^2} \tag{2.1}$$

where σ is the standard deviation, N_{ro} is the readout noise and N_P is the Poisson noise. The square of the Poisson noise is equal to the pixel value (in electrons), giving:

$$\sigma_{e^-} = \sqrt{N_{ro}^2 + \bar{n}_{e^-} \cdot t_{exp}} \tag{2.2}$$

with t_{exp} the exposure time and $\bar{n}_{e^-}$ the measured average number of background electrons per pixel per second. Dividing by the exposure time gives the noise normalized to unit time, that can be obtained from the images by selecting an area free from objects and artefacts and measuring the standard deviation in that area (the frame output by the `calwfc3` pipeline has units of electrons per second, so has already been corrected for the gain and normalized by the exposure time). Discrepancies between the expected and measured values are well within 10%.

Finally, the predicted noise for the combined image is given by:

$$\sigma_{e^-} = \frac{\sqrt{N_{ro}^2 + \bar{n} \cdot t_{exp}}}{t_{exp} \cdot \sqrt{n_F}} \tag{2.3}$$

where n_F is the number of frames contributing to the final image. Again, there is good agreement between the expected and measured values.

Another way of evaluating the noise is to apply a correction factor F_A to the correlated noise measured in areas of the multidrizzled images. The derivation of this correction factor is fully described in appendix A of Casertano et al. (2000). This factor depends on the chosen pixel scale and pixfrac parameters, and on the placement of the area where photometry is performed onto the output grid, meaning that it can vary across the image. However an average correction factor is derived in the same paper:

$$\sqrt{F_A} = \begin{cases} 1 - \frac{p}{3s} & \text{for } s > p \\ (\frac{s}{p})(1 - (\frac{s}{3p})) & \text{for } s < p \end{cases} \tag{2.4}$$

where s is the the ratio between the output and input pixel scale and p is the pixfrac value. Dividing the measured correlated error by F_A gives a very good approximation of the uncorrelated errors: a good agreement (at the 0.05 mag level) was found with the sensitivity measurements using the true-noise frames described earlier, except for the HUDF data where the corrected drizzle noise underestimated the true noise by 0.1-0.2 mag, perhaps because of the large number of frames combined with small sub-pixel shifts. The sensitivity measurements from the true-noise frame were adopted, having checked that consistent results were produced by the ETC, the noise model, and the noise in the drizzle frame corrected for pixel correlations. Our measured noise in the HUDF is in good agreement with Bouwens et al. (2010a), but we note that McLure et al. (2010) appear to be $\approx 0.3\,\mathrm{mag}$ less sensitive (although we note that their $5\,\sigma$ magnitude limit in a $0\farcs4$-diameter aperture appears not to have been corrected to total magnitudes with an aperture correction, unlike in Bouwens et al. 2010a).

Chapter 3

Selection of Candidates

Once the WFC3 frames are stacked with sub-pixel precision and registered to the ACS images, block-averaged 2×2, obtaining the same pixel scale of $0\farcs06$ set as MULTIDRIZZLE output for the WFC3 images, high redshift galaxy candidates can be selected. The process requires several steps and all the criteria used are described in this chapter.

3.1 Construction of Catalogues

The first step of candidate selection is to create catalogues of the sources in the observed fields. The SExtractor (Source-Extractor) photometry package (Bertin & Arnouts 1996) version 2.5.0 was used for this purpose: it estimates the background, detects sources and performs photometry.

The program recognises as a source every object showing at least a number of contiguous pixels with a signal of a certain σ or higher. Both the number of contiguous pixels and the σ threshold are set by the user. Given the compact nature of primeval galaxies, the chosen number of contiguous pixels for this work is 5, with a signal of 2σ. We carried out comparisons of catalogues obtained with different parameters (12 and 24 contiguous pixels with 1.5σ). These catalogues are of course different, but once our selection criteria are applied (see Section 3.2) the resulting lists of objects are very similar to each other. After the objects are selected, the program is capable of both isophotal and circular aperture photometry (see Figure 3.1), and also estimates the total apparent magnitude. Aperture photometry with $0\farcs6$ diameter (ten pixels) with an aperture correction is adopted for this work. It is preferable to the isophotal photometry that would not be reliable given the faintness of the objects we are looking for. These objects are also compact so an aperture does not usually cut out a significant portion of the PSF, while a total magnitude calculation could include other objects (or parts) in the computation.

SExtractor can be operated in two different modes: single-image and dual-image. In single-image mode it simply identifies sources and performs photometry of a specified image while in dual-image mode it identifies sources on a "training" image and performs photometry at the same coordinates but in another image. The dual-image mode is clearly suited for the use of the Lyman-break technique, since it relies on multiple images at different wavelength and it is particularly handy for the photometry in the optical bands, where minimal flux is expected.

Both the images taken with the first and second filters longwards of the expected break wavelength can be used as training images. The first filter can be affected by the break for objects in the far end of the redshift range probed resulting in a lower flux, so these objects might not be picked up by SExtractor. However, if such objects are so faint not to be selected, they are unlikely to be

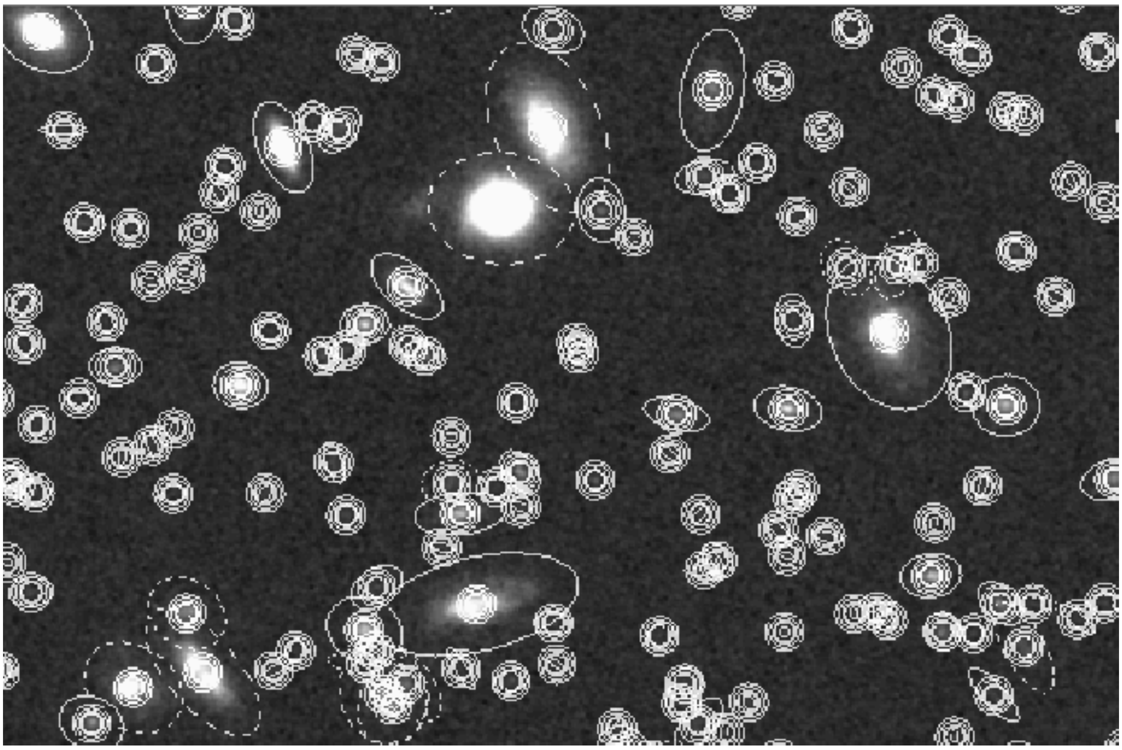

Figure 3.1: An image produced by SExtractor, with apertures for photometry traced around the selected targets. The number and diameter of apertures around targets are set by the user.

suitable dropouts (they could be actual dropouts, but at higher redshifts). The second filter longwards of the break will not be contaminated by the break, but given the 'blue' UV spectral slope of these objects, meaning that flux density (f_{v}) decreases with the increase of the wavelength (Wilkins et al. 2011b), its signal might be weaker than that in the lower wavelength filter. It is however rare to have such steep spectral slopes that an object to disappears between two consecutive broadband filters, and indeed a single detection longwards of the break is not considered as strong proof for being a high redshift galaxy.

SExtractor is run in single-mode for the training image, and then in dual-image mode between the training image and all the other available broad band images for that field (or area of the field). The result is a number of catalogues equal to the number of different images, with magnitudes computed for each aperture used in the training image. The respective aperture corrections are applied to these magnitudes, while the magnitude errors are divided by the factor given by equation 2.4. The aperture corrections are 0.1 magnitudes for the ACS images, 0.2 for Y-band and 0.25 for the J- and H-band (see section 2.3.3). The aforementioned reddening corrections are also applied.

3.2 Candidate Selection

As already mentioned, the identification of candidates is achieved using the Lyman break technique (e.g. Steidel et al. 1996), where a large colour decrement is observed between filters either side of Lyman-α in the rest-frame of the galaxy. At $z \approx 8-9$ the location of the Lyman-α break is redshifted to $\sim 1.1\mu$m the WFC3 Y_{105w} and J_{125w} are suitably located such that a $7.6 < z < 9.8$ star forming galaxy will exhibit a significant flux decrement between these two filters, while for $z \approx 7$ the break lies at $\sim 1.0\mu$m, between filters WFC3 Y_{105w} and ACS z_{850lp}, with a redshift range of $6.5 < z < 8.0$. It is important to know that the selection efficiency drops at the extremes of these ranges, as will be shown later.

3.2.1 Contaminants

Searching for distant galaxies using only broadband photometry means that contamination of the sample of high redshift galaxies by other kinds of sources is a potentially serious issue. There are two main sources of contamination: objects whose intrinsic colours are similar to those of the target population; and faint objects with intrinsically different colours but whose observed colours scatter into our selection because of photometric noise. A third source of contamination, transient phenomena, might occur when different broadband images are separated by many years: a transient such as a supernova or high-proper-motion object which entered the Y-band but was absent at that location in the ACS could be erroneously identified as a Lyman-break galaxy. These contaminants might be an issue in this search for z'-drops, as the WFC3 Y-band images of the GOODS-South field were taken several years after the ACS z'-band images, and indeed a probable supernova was identified in the WFC3 imaging of the HUDF (e.g., Bunker et al. 2010), while it is not significant for the Y-drop selection, since the WFC3 Y-, J- and H-band images were taken close in time.

3.2.1.1 Intrinsically Red Objects

There are two distinct types of objects whose apparent $z_{850lp} - Y_{105w}$ ($Y_{105w/098m} - J_{125w}$) colours are similar to those of Lyman- break galaxies at $z \approx 7$ ($z \approx 8 - 9$): lower-redshift galaxies at $z \approx 1.5$ ($z \approx 2$) have the Balmer/4000Å break feature between the filters used, while some low mass dwarf stars, especially those of L and T spectral class, have low temperatures and broad absorption features that can mimic a spectral break at the right point of the spectrum. Given the direction of observations, well outside the Galactic plane, the main contribution to contaminants is expected from lower redshift galaxies rather than Galactic dwarfs. Examples of the spectral energy distributions (SEDs) of each of these types of object (a model 3.5 Gyr old single aged stellar population at $z = 2.5$ and a T4.5 dwarf star) are shown in Figure 3.2 along with the filters used for imaging and a synthetic $z = 8.0$ galaxy SED.

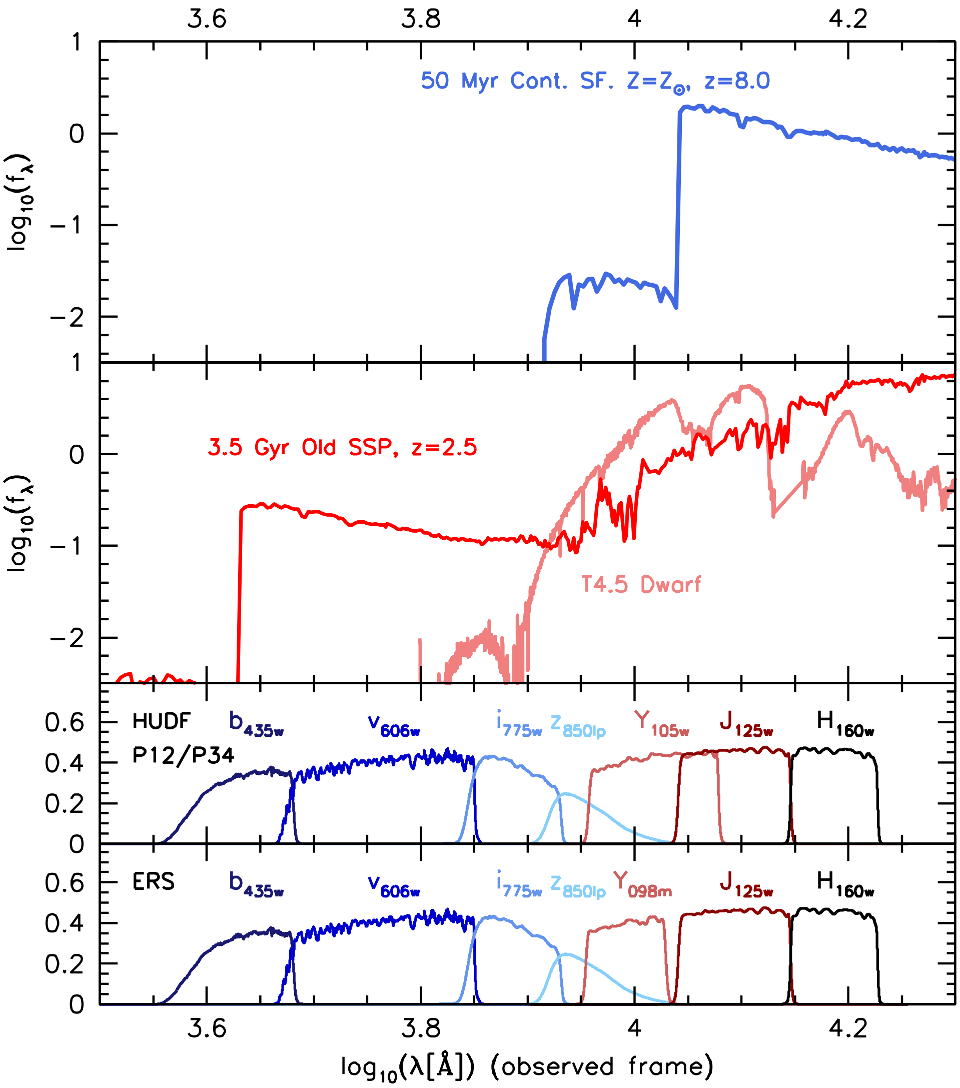

Figure 3.2: Top panel - Model (from the Starburst99, Leitherer et al. 1999) spectral energy distribution (SED) of a redshifted $z = 8$ star forming galaxy. Middle panel - Potential contaminants: Observed SED of a low-mass dwarf star (class: $T4.5$, Knapp et al. 2004) together with the model (Starburst99) SED of a 3.5Gyr Single-aged Stellar Population (SSP) at $z = 2.5$. The bottom two panels show the transmission functions of the combination of filters available to each field.

The similarities between these objects' SEDs are however limited to the two filters either side of the break, particularly for the lower-redshift interlopers: as said, $z \approx 7 - 9$ star forming galaxies tend to have blue spectral slopes, while the lower redshift galaxies appear to be redder. The addition of a further filter at longer wavelengths (J_{125w} for z'-drops and H_{160w} for Y-drops in this work) can then be used to discriminate between high-z and lower redshift galaxies: with an additional filter it is possible to plot the expected location of both actual targets and interlopers on a colour – colour diagram (see Figures 3.3, 3.4 and 3.5) where these objects occupy different areas and can then be discriminated against. To predict where in the colour – colour diagram the high-z galaxies and the lower redshift interlopers would be placed, a synthetic galaxy spectrum is convolved with the transmission functions of the filters used for the observations. The areas enclosed in the resulting functions (one for each filter) are proportional to the flux collected with each filter, an insufficient information to infer a magnitude, but enough to calculate the flux differences between filters, i.e. the colours, which are the matter of interest in this case. This operation is performed for a range of different redshifts and for both high-z galaxies and lower redshift interlopers synthetic spectra to obtain the tracks (blue and red, respectively) in the colour – colour diagrams (Figures 3.3, 3.4 and 3.5).

The synthetic galaxy spectra used reproduce the drop in flux at the Lyman break are obtained using PEGASE.2 (Fioc & Rocca-Volmerange 1997) and present no flux below 912 Å and 99% absorption between 1216 and 912 Å and blue rest-frame UV colours. A Gaussian distribution of spectral slopes have been used, with $\langle\beta\rangle = -2.2$ and $\sigma(\beta) = 0.5$, reflecting the generally blue spectral slopes observed in Lyman-break galaxies at $z \geq 6$ (Stanway, McMahon & Bunker 2005; Bouwens et al. 2010b; Wilkins et al. 2011b; Bunker et al. 2010). β is the UV spectral slope parameter, defined as $f_\lambda = \lambda^\beta$, with f_λ flux density per wavelength interval and λ the rest wavelength. $\beta = -2$ implies no decrement in flux in the two successive filters longwards of the Lyman-break (i.e. for Y-drops $J - H = 0.0$).

L and T dwarfs contamination to the Y-drop sample in the HUDF, CANDELS, P12 and P34 fields is mostly ruled out by the $Y - J$ colour selection adopted, but the addition of the of a longer wavelength filter (H_{160w}) is still important in excluding these objects in the ERS field, where the different Y-band filter used results in larger $Y - J$ colours for Galactic dwarfs (Figure 3.4, bottom right panel). For the z'-drop sample, the additional filter (J_{125w} in this case) is necessary in all fields (Figure 3.3) to rule out Galactic contaminants.

3.2.1.2 Photometric Scatter

Even with the addition of a third filter, some contaminants will be scattered into the area where our targets are located because of photometric noise and could be selected as candidates. At low signal to noise ratio, this contamination could be significant and has to be taken care of. To do that, the optical images of the analysed fields are used: intrinsically, $z \approx 7 - 9$ galaxies should not have any significant flux in the b_{435w}, v_{606w} and i_{775w} bands, so objects with a $> 2\sigma$ detection in one or more of these spectral bands will be excluded from the candidates selection.

3.2.2 Selection criteria

In this section, the selection criteria used for both z'- and Y-drops in the analysed fields are described in detail.

3.2.2.1 z'-drops in HUDF, P12, P34 and ERS

In order to select robust $z \approx 7$ star-forming galaxy candidates, a J-band magnitude cut is imposed: only objects with a signal stronger than 6σ are selected. The noise varies for each field and is reported in Table 2.1. The J-band is chosen as it will be unaffected by either the drop in flux due to the Lyman-break or the possible Lyman-α emission, being therefore a good indication of the rest-frame UV luminosity of the candidates.

As already mentioned, the observations of the ERS field employed a different Y-band filter (F098M) from those of the deeper fields (HUDF, P12 and P34, where F105W was used). This affects the expected colours for high-z galaxies, so two different windows are drawn in the colour – colour diagrams for the deep fields and ERS. The colour selection criteria for HUDF, P12 and P34 are:

$$\begin{aligned}(z_{850lp} - Y_{105w}) &> 1.0\\ (z_{850lp} - Y_{105w}) &> 2.4 \times (Y_{105w} - J_{125w}) + 0.4\\ (Y_{105w} - J_{125w}) &< 1.0\end{aligned}$$

while for the ERS field the colour cuts are:

$$\begin{aligned}(z_{850lp} - Y_{098m}) &> 1.2\\ (z_{850lp} - Y_{098m}) &> 0.9 \times (Y_{098m} - J_{125w}) + 0.7\\ (Y_{098m} - J_{125w}) &< 2.0\end{aligned}$$

Colour – colour diagrams for each field including the expected position of interlopers, of high-z galaxy and candidates actually selected are shown in Wilkins et al. (2011a).

In case of a non-detection in the z'-band (i.e. the signal at the specified coordinates found by SExtractor in the J-band image is less than 2σ), the 2σ limit is quoted in the tables, and the same limit is used to determine the $z - Y$ colour.

3.2.2.2 z'-drops in CANDELS

For the selection of candidates in the CANDELS area, the brightness cut imposed is different: candidates have to be detected at at least 5σ in both Y- and J-bands. This cut is comparable to a 7σ cut on a combination of these two waveband images, but minimises the influence that either Lyman-break and Lymanα emission in the Y-band or a declining spectral slope in the J-band might have on the selection. The filters used for the CANDELS observations are the same used in the Illingworth programme (HUDF and flanking fields), so the same colour cuts are used as in Wilkins et al. (2011b). In addition, a selection of candidates is performed using Bouwens' group selection window (Bouwens et al. 2011, Oesch et al. 2012):

$$\begin{aligned}(z_{850lp} - Y_{105w}) &> 0.7\\ (z_{850lp} - Y_{105w}) &> 1.4 \times (Y_{105w} - J_{125w}) + 0.42\end{aligned}$$

$$(Y_{105w} - J_{125w}) \quad < \quad 0.45$$

This “double” selection is carried out to allow for a better comparison with other groups as well as to assess the influence of the colour selection window on the determination of a luminosity function. The colour – colour diagram including both the “Deep” and “Wide” CANDELS areas is shown in Figure 3.3.

To determine the $z - Y$ colour, the effective signal of the z'-band is used if it is stronger than 1σ. If the signal is less than 1σ, the lower limit applied to the z'-band magnitude is determined by adding to the measured signal the average background noise of the z'-band image in the same-sized aperture.

3.2.2.3 Y-drops in HUDF, P12, P34 and ERS

The Y-drop candidates in these fields are selected imposing a J-band magnitude 6σ cut, although only candidates with a 7σ detection will be considered for the calculation of the luminosity function. The catalogues for the selection were also based on the J-band image, even though it is immediately before (i.e. at longer wavelengths than) the expected wavelength of the Lyman-break and it could be contaminated by the spectral break or possible Lyman-α emission. As explained earlier, this does not heavily affect the SExtractor selection, but it could have a bigger influence on the inferred continuum luminosity. The choice of applying a brightness cut in the J-band was however necessary as the H-band images for ERS and P12 are particularly shallow and magnitudes in that band would have a large uncertainty anyway. Moreover, most of the selected objects are also weakly detected in the Y-band: for these objects the break occurs either completely

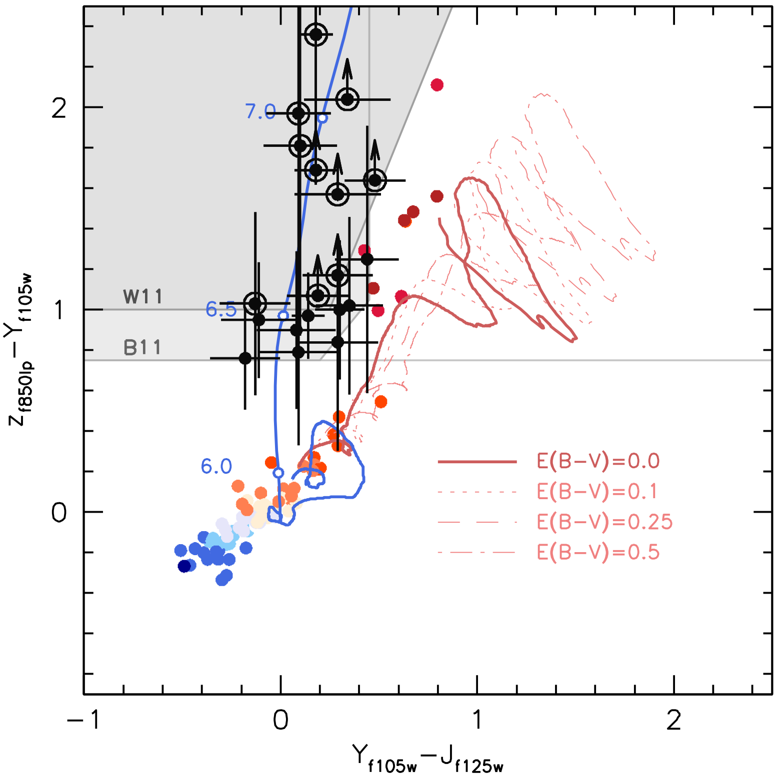

Figure 3.3: Colour - colour diagram for z'-drops selected in the CANDELS wide and deep areas. The shaded areas are the selection windows used, defined in Section 3.2.2 (light shading for the B11z selection window, darker shading for W11). The objects we found are shown as grey dots (objects not meeting any of the colour - colour windows we are considering), black dots (objects in B11z) and black circled dots (objects meeting W11). The coloured dots denote the position of potential L and T dwarfs stars contaminants. The solid red line shows the colours that lower redshift galaxies (modelled as an instantaneous burst of star formation at $z = 20$ and no dust) would have, and the dotted, dashed and dot-dashed lines show this low-redshift template with reddenings of $E(B - V) = 0.1$, 0.25 & 0.5 respectively. The blue line is the predicted path taken by high-redshift galaxies (constant star formation from $z = 20$, no dust). For the red and blue tracks, numbers in correspondence with open circles indicate the redshift.

outside the J-band or in the small overlap region of filters J_{125} and Y_{105}. In the former case, only Lyman-α emission (if any) could affect the absolute continuum magnitude calculation from the J-band, and only if the break occurs just outside the J-band filter, while in the latter the break would only affect a minor portion of the whole filter, minimising the magnitude inaccuracy.

For the fields observed with the Y_{105} filter, the colour selection criteria are:

$$\begin{aligned}
(Y_{105w} - J_{125w}) &> 0.9 \\
(Y_{105w} - J_{125w}) &> 0.73 \times (J_{125w} - H_{160w}) + 0.9 \\
(J_{125w} - H_{160w}) &< 1.5
\end{aligned}$$

while for ERS field, where the Y_{098} was employed, are:

$$\begin{aligned}
(Y_{098m} - J_{125w}) &> 0.9 \\
(Y_{098m} - J_{125w}) &> 0.64 \times (J_{125w} - H_{160w}) + 1.28 \\
(J_{125w} - H_{160w}) &< 0.8
\end{aligned}$$

Colour – colour diagrams for these four fields are shown in Figure 3.4. The non-detection criterion on the optical bands could in theory be extended for Y-drops to include the z'-band, however the z_{850} filter does have a red tail which overlaps with the Y-band filters used, so it is conceivable that a Y-drop towards the lower end of the redshift selection range might have residual z'-band flux, so the optical non-detection criterion is maintained the same as for the z'-drops.

One of Y-drops selected in this work (P34.YD5) does have a $\sim 2\sigma$ detection in the z'-band. In case the object is not detected in the Y-band ($< 1\sigma$), the average background noise is added to the measured signal and the resulting magnitude is used as a lower limit on the Y magnitude.

3.2.2.4 Y-drops in CANDELS

Analogously to the z'-drops case, the brightness lower limit for the Y-drops in the CANDELS areas is different from the one used for Y-drops in other fields, and it is a 5σ limit in both H- (where catalogues were based on) and J-band. The colour selection cuts though remain unchanged from the deep fields Y-drop selections, and for the same aims of comparing and different selection window effects (as described for z'-drops), a selection on Bouwens' window is also derived:

$$\begin{aligned}(Y_{105w} - J_{125w}) &> 0.45\\ (J_{125w} - H_{160w}) &< 0.5\end{aligned}$$

Figure 3.5 shows the CANDELS Y-drops colour – colour diagram. All the candidates identified in these fields are detected in the Y-band, hence no lower limits on the Y-band magnitude are needed to determine the $Y - J$ colour.

3.2.3 Candidate Galaxies at $z \approx 7 - 9$

The search of the described fields produced 64 z'-drops and 30 Y-drops, analysed in the following sections.

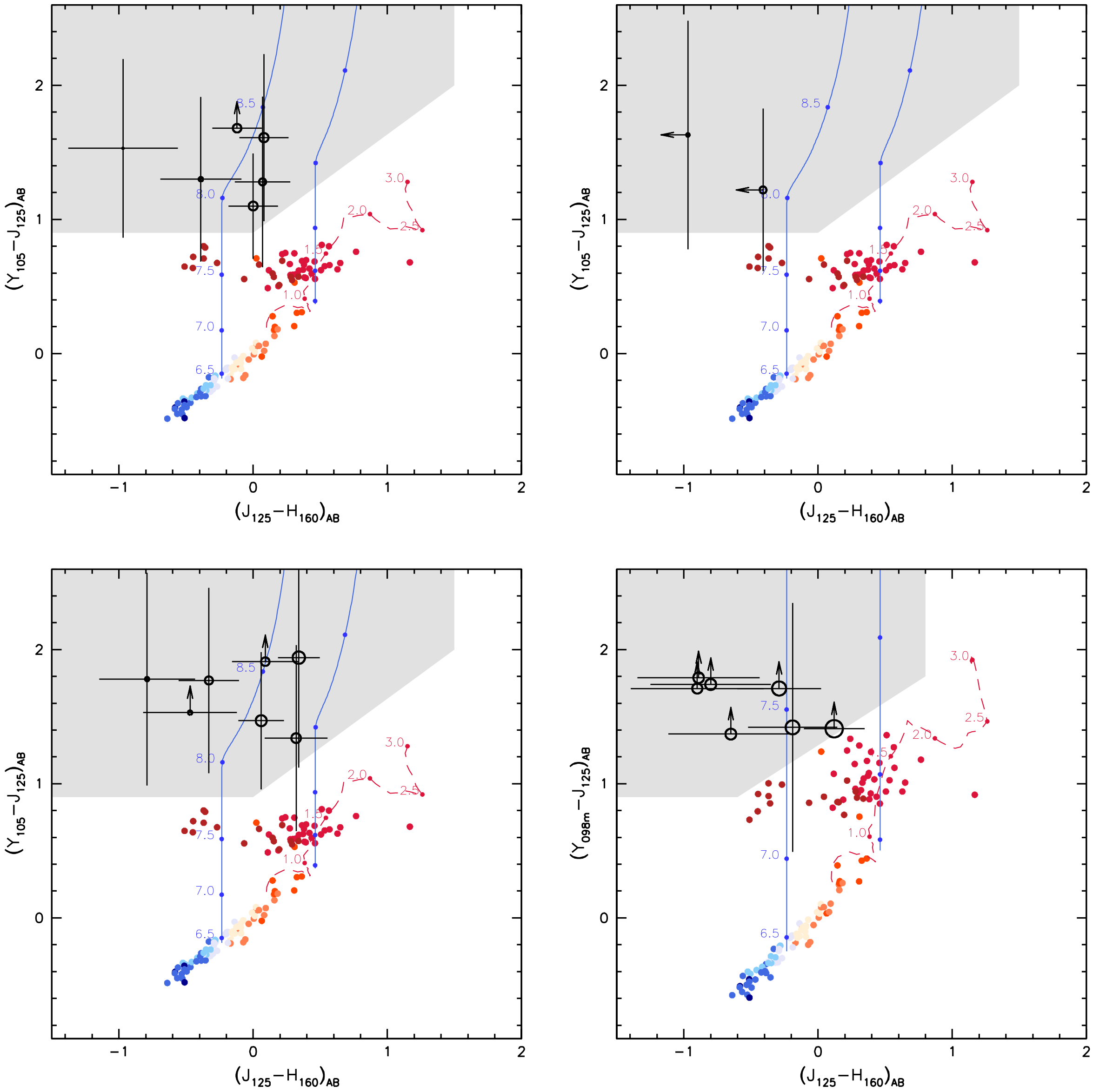

Figure 3.4: $J_{125w} - H_{160w}$ and $Y_{105w} - J_{125w}$ colour - colour figures for the HUDF (top left), flanking fields P34 (bottom left) and P12 (top right) and ERS (bottom right), showing our YJH colour selection window (grey shaded area), the location of our candidates, the predicted paths taken by high-redshift galaxies (solid lines, $\beta = -3.0$, left, and $\beta = 0.0$, right) and the location of possible contaminating sources. Contaminating sources include Galactic stars (O - T dwarf stars, with L and T stars being redder, denoted by filled circles) and a passively evolving 'early-type' galaxy (modelled as an instantaneous burst of star formation at $z = 10$ followed by passive luminosity evolution, denoted by the dashed line). High-redshift candidates are denoted by black circles (where the size of the circle is an indication of the apparent J_{AB} magnitude, with bigger circles indicating brighter sources). Limits and error bars are $1\,\sigma$.

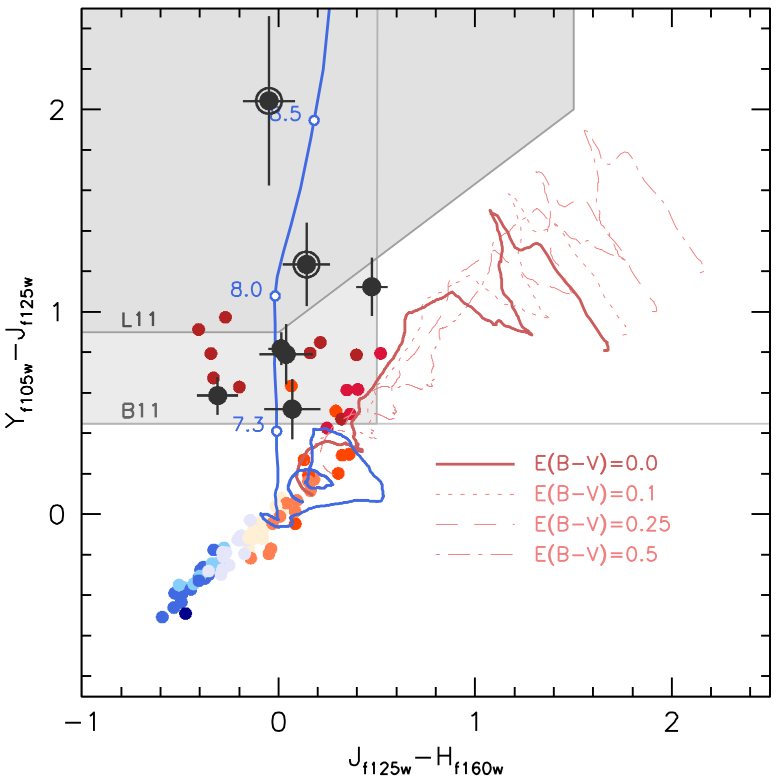

Figure 3.5: Colour - colour diagram for Y-drops selected in the CANDELS deep area. The shaded areas are the selection windows used, defined in Section 3.2.2 (light shading for the B11Y selection windows, darker shading for L11). The objects we found are shown as grey dots (objects not meeting any of the colour - colour windows we are considering), black dots (objects in B11Y) and black circled dots (objects meeting L11). The coloured dots denote the position of potential L and T dwarfs stars contaminants. The solid red line shows the colours that lower redshift galaxies (modelled as an instantaneous burst of star formation at $z = 20$ and no dust) would have, and the dotted, dashed and dot-dashed lines show this low-redshift template with reddenings of $E(B-V) = 0.1$, 0.25 & 0.5 respectively. The blue line is the predicted path taken by high-redshift galaxies (constant star formation from $z = 20$, no dust). For the red and blue tracks, numbers in correspondence with open circles indicate the redshift.

3.2.3.1 z'-drops

With the selection criteria just described, a total of 64 $z \approx 7$ galaxy candidates are found (HUDF: 11, P34: 15, P12: 7, ERS: 11, CANDELS-Deep: 17, CANDELS-Wide: 2). Images of the candidates in all the wavebands found in the CANDELS area are shown in Figure 3.6, with their photometry presented in Table 3.1. For images and photometry of the z'-drops in HUDF, UDF-P12, UDF-P34 and ERS please refer to Wilkins et al. (2011a). The apparent J-band magnitudes of these candidates range from 25.87 (GS.D-zD1) to 28.36 (HUDF.z.3650). For the CANDELS fields, 18 of the 19 candidates satisfy Bouwens' selection window, and 10 satisfy our more conservative window. Only one of these objects (GS.D-zD3) is selected by our criteria but not by Bouwens's.

3.2.3.2 Y-drops

The total number of candidate $z \approx 8 - 9$ galaxies identified with this work is 30 (HUDF: 6, P34: 7, P12: 2, ERS: 9, CANDELS-Deep: 6, CANDELS-Wide: 0). Images of these candidates in the $bviz'YJH$ filters used are shown in Figures 3.7 and 3.8 and their photometry is listed in Tables 3.2 and 3.3. There are 9 (of the 30) objects in the Y-drop list flagged with a '*' as being more marginal than the other candidates as they sit at the limits of our selection, although they are plausible$z \approx 8 - 9$ galaxies (the effective volume calculation already corrects for actual high-redshift galaxies excluded as lying just outside the selection region, see Section 4.1). Objects ERS.YD2, ERS.YD5, ERS.YD9 and P34.YD7 are flagged because using a 1σ lower limit on the $Y - J$ colour these candidates fully meet our colour selection criteria, while a more conservative 2σ lower limit on Y

$\mathbf{z \approx 7}$

ID	RA (J2000)	Dec (J2000)	z_{AB}	Y_{AB}	J_{AB}	H_{AB}	$(z-Y)_{AB}$	$(Y-J)_{AB}$	β
GS.D-zD1	03:32:55.930	-27:49:38.59	26.98 ± 0.21	26.01 ± 0.044	25.87 ± 0.071	26.25 ± 0.15	0.97	0.14	-3.63 ± 0.74
GS.D-zD2[1]	03:32:37.181	-27:48:56.68	28.88 ± 0.74	26.52 ± 0.043	26.34 ± 0.074	26.46 ± 0.12	2.36	0.18	-2.51 ± 0.64
GS.D-zD3[1,2]	03:32:08.130	-27:46:40.88	> 28.49	26.85 ± 0.12	26.37 ± 0.10	26.39 ± 0.15	> 1.64	0.48	-2.09 ± 0.82
GS.D-zD4[1]	03:32:36.006	-27:44:41.74	> 28.26	26.57 ± 0.067	26.39 ± 0.085	26.52 ± 0.14	> 1.69	0.18	-2.56 ± 0.74
GS.D-zD5	03:32:25.447	-27:50:53.36	27.76 ± 0.33	26.76 ± 0.094	26.46 ± 0.084	26.44 ± 0.12	1.0	0.3	-1.91 ± 0.67
GS.D-zD6	03:32:09.583	-27:46:32.06	28.01 ± 0.42	26.99 ± 0.13	26.64 ± 0.11	26.01 ± 0.10	1.02	0.35	$0.70 \pm 0.73^{*}$
GS.W-zD1	03:32:57.390	-27:53:21.77	27.51 ± 0.25	26.56 ± 0.18	26.67 ± 0.16	26.84 ± 0.24	0.95	−0.11	-2.7 ± 1.2
GS.W-zD2	03:32:36.729	-27:54:42.12	27.35 ± 0.21	26.59 ± 0.17	26.77 ± 0.14	26.58 ± 0.17	0.76	−0.18	-1.19 ± 0.94
GS.D-zD7	03:32:36.240	-27:46:31.37	28.51 ± 0.65	27.26 ± 0.12	26.82 ± 0.11	26.78 ± 0.15	1.25	0.44	-1.83 ± 0.85
GS.D-zD8[1]	03:32:40.693	-27:44:16.72	> 28.09	27.02 ± 0.11	26.83 ± 0.12	26.71 ± 0.16	> 1.07	0.19	-1.49 ± 0.91
GS.D-zD9[1]	03:32:28.859	-27:49:12.63	> 28.35	27.18 ± 0.12	26.89 ± 0.14	26.88 ± 0.20	> 1.17	0.29	-1.96 ± 1.10
GS.D-zD10[1]	03:32:27.916	-27:45:42.72	> 29.28	27.24 ± 0.17	26.9 ± 0.14	27.80 ± 0.47	> 2.04	0.34	$-5.8 \pm 2.1^{*}$
GS.D-zD11[1]	03:32:19.938	-27:47:10.57	29.01 ± 1.05	27.04 ± 0.10	26.95 ± 0.13	27.59 ± 0.35	1.97	0.09	-4.7 ± 1.6
GS.D-zD12[1]	03:32:47.638	-27:48:29.21	28.98 ± 0.93	27.17 ± 0.11	27.07 ± 0.15	27.66 ± 0.39	1.81	0.1	-4.5 ± 1.8
GS.D-zD13	03:32:12.512	-27:47:56.86	28.12 ± 0.37	27.22 ± 0.12	27.14 ± 0.16	27.87 ± 0.46	0.9	0.08	-5.1 ± 2.1
GS.D-zD14[1]	03:32:37.230	-27:45:38.41	28.05 ± 0.44	27.02 ± 0.10	27.15 ± 0.15	27.36 ± 0.26	1.03	−0.13	-2.9 ± 1.3
GS.D-zD15[1]	03:32:30.793	-27:50:27.19	> 29.03	27.46 ± 0.17	27.17 ± 0.15	27.56 ± 0.32	> 1.57	0.29	-3.7 ± 1.6
GS.D-zD16	03:32:16.057	-27:47:57.72	28.09 ± 0.44	27.3 ± 0.13	27.21 ± 0.16	27.70 ± 0.37	0.79	0.09	-4.1 ± 1.8
GS.D-zD17	03:32:35.067	-27:46:34.96	28.35 ± 0.52	27.51 ± 0.15	27.22 ± 0.15	27.89 ± 0.44	0.84	0.29	$-4.8 \pm 2.0^{*}$

[1] in W11 selection.; [2] not selected using B11 criteria.; * outside the colour–colour selection window employed by Wilkins et al. (2011b) for a clean selection of z-drops for analysis of spectral slope, β.

Table 3.1: z'-band drop out candidate at $z \approx 7$ meeting either of the selection criteria described. Objects are ordered by apparent J_{AB} magnitude. Where quoted, limits are 1σ

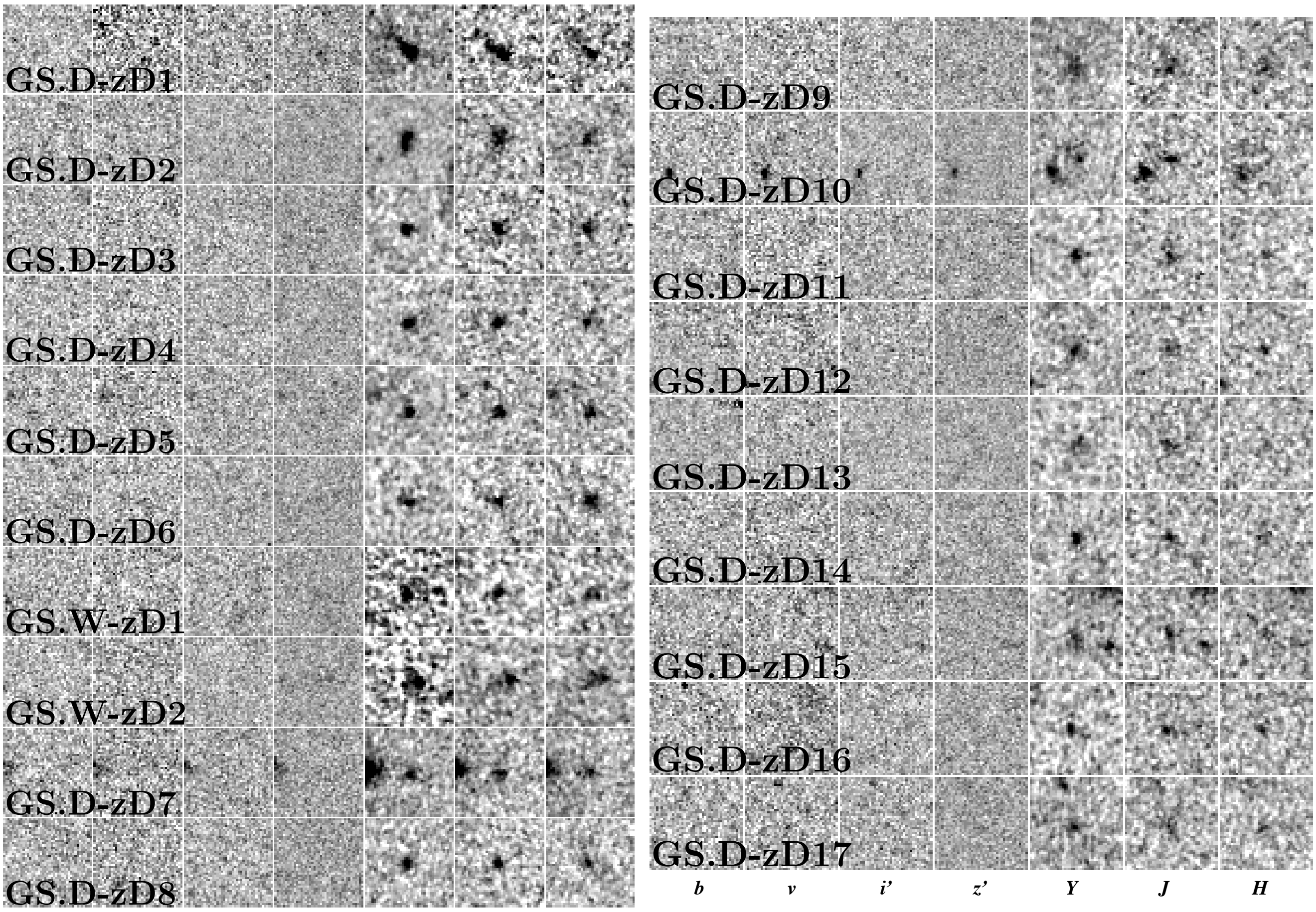

Figure 3.6: $2\farcs4 \times 2\farcs4$ $bvizYJH$ thumbnail images of potential $z \approx 7$ objects (z'-drops) meeting our selection criteria in CANDELS GOODS-South field, ordered by J-band magnitude (brightest at the top).

magnitude would locate them just below the selection colour – colour window. Even with the 2σ limit these objects would be fully consistent with falling within the selection window: the $Y - J$ colour used to locate these objects in the colour – colour diagram would still be a lower limit, and deeper Y-band imaging could unambiguously move them into the selection window. Candidate ERS.YD8 is still in the contamination area using the 1σ limit, but still compatible with the adopted selection criteria. Object P34.YD5 in P34 is flagged because it has a

$\sim 2\sigma$ detection in the z-band. There are no detections in v-, i- and Y -bands (no b-band is available for the P34 field), though, so it is still a likely high-redshift ($z > 6$) object, as the z'-band flux might be statistical fluctuation.

Two potential high redshift galaxies in field UDF-P12 are also flagged, on the grounds that the short exposure time of the H-band image in this field made the measured H-band magnitudes very noisy and unreliable. At the time of the data analysis that led to Lorenzoni et al. (2011), the WFC3 Illingworth programme (see Section 2.2) was not complete, and only 4 exposures (out of a total 26) were available for the P12 H-band. The reasons why we decided to include them in the Y-drop list despite being detected in the J-band only are here explained. The upper limits on the $J-H$ colours place them well away from the red contaminants region (Figure 3.4), but the UV luminosity in the H-filter (uncontaminated by the effects of Lyman-α forest absorption) is required to infer the absolute UV magnitude (as described in Section 3.2.2).

The possibility of these single-band detections being due to transients is considered (such as is the case for the likely supernova in the WFC3 images of the HUDF, object zD0 in Bunker et al. 2010). The P12 field was observed in J-band in two observing blocks, with 8 frames taken on U.T. 2009 November 02, and the other 16 frames taken over U.T. 2009 November 10-15. As a check, the two different epochs are separately combined with MULTIDRIZZLE: the magnitude of P12.YD1 is consistent between the two epochs, with $J_{AB} = 28.07 \pm 0.25 (4.3\sigma)$ and $J_{AB} = 27.95 \pm 0.16\,(6.8\sigma)$ respectively. However, P12.YD2 might show some variability in the J-band with $J_{AB} = 27.36 \pm 0.13\,(8.3\sigma)$ for the first block of data and $J_{AB} = 28.14 \pm 0.19\,(5.8\sigma)$ for the second. Hence it is plausible that P12.YD2 might be a transient rather than a high-redshift Y-drop.

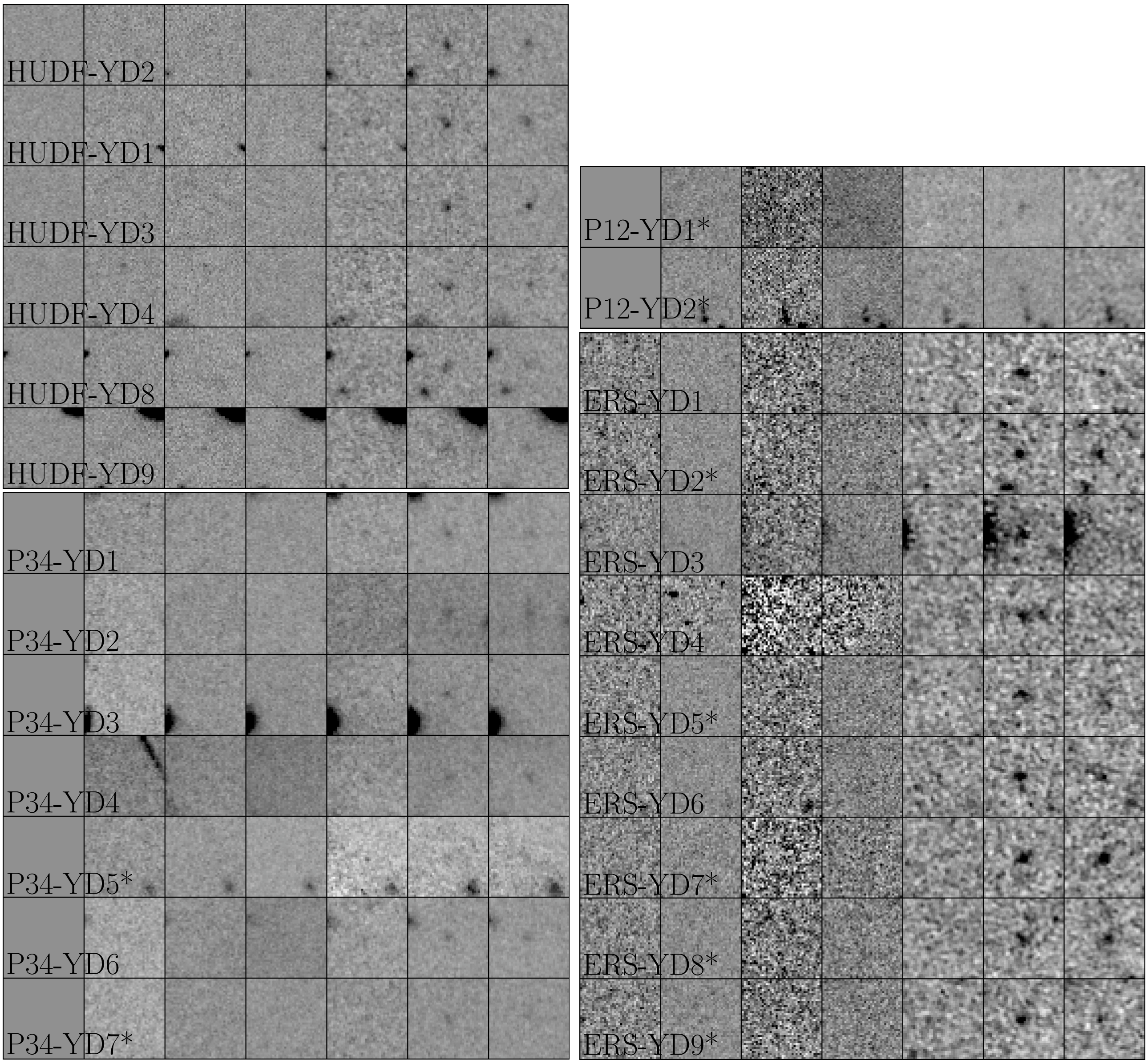

Figure 3.7: $2\farcs4 \times 2\farcs4$ $(b)vizYJH$ thumbnail images of Y-drops meeting our selection criteria in the HUDF, UDF-P12, UDF-P34 and ERS fields. Within each field they are ordered by H-band magnitude (brightest at the top). Objects marked with * are more marginal candidates, see Section 3.2.3. The fields UDF-P12 and UDF-P34 do not have ACS b-band imaging.

ID	RA	Dec	$Y_{\rm AB}$	$J_{\rm AB}$ (significance, σ)	$H_{\rm AB}$	$(Y-J)_{AB}$	$(J-H)_{AB}$
HUDF.YD2	03:32:37.796	-27:46:00.12	> 29.76	28.08 ± 0.12 (8.9σ)	28.20 ± 0.14	> 1.66	-0.12
HUDF.YD1	03:32:42.873	-27:46:34.58	29.25 ± 0.37	28.15 ± 0.13 (8.3σ)	28.15 ± 0.13	1.10	0.00
HUDF.YD3	03:32:38.135	-27:45:54.03	29.79 ± 0.61	28.18 ± 0.13 (8.1σ)	28.10 ± 0.13	1.61	0.08
HUDF.YD4	03:32:33.130	-27:46:54.49	29.85 ± 0.65	28.32 ± 0.15 (7.1σ)	29.29 ± 0.38	1.53	-0.97
HUDF.YD8	03:32:43.082	-27:46:27.75	29.75 ± 0.59	28.45 ± 0.17 (6.3σ)	28.84 ± 0.25	1.30	-0.39
HUDF.YD9	03:32:36.360	-27:46:23.35	29.78 ± 0.61	28.50 ± 0.18 (6.1σ)	28.43 ± 0.17	1.28	0.07
P34.YD1	03:33:00.340	-27:51:20.97	29.71 ± 0.68	27.94 ± 0.12 (9.1σ)	28.27 ± 0.19	1.77	-0.33
P34.YD2	03:33:09.657	-27:51:16.45	29.89 ± 0.81	27.95 ± 0.12 (9.0σ)	27.61 ± 0.10	1.94	0.34
P34.YD3	03:33:07.474	-27:51:14.89	29.85 ± 0.78	28.07 ± 0.14 (8.1σ)	28.86 ± 0.33	1.78	-0.79
P34.YD4	03:33:04.857	-27:51:38.28	29.36 ± 0.50	27.89 ± 0.11 (9.5σ)	27.83 ± 0.13	1.47	0.06
P34.YD5*	03:33:06.596	-27:52:48.95	> 30.20	28.29 ± 0.17 (6.6σ)	28.20 ± 0.18	> 1.91	0.09
P34.YD6	03:33:06.901	-27:51:32.54	29.69 ± 0.67	28.35 ± 0.18 (6.2σ)	28.03 ± 0.15	1.34	0.32
P34.YD7*	03:33:09.286	-27:51:32.22	> 29.91	28.38 ± 0.18 (6.1σ)	28.85 ± 0.32	> 1.53	-0.47
P12.YD1*	03:33:03.034	-27:41:57.00	29.64 ± 0.84	28.01 ± 0.14 (7.9σ)	> 28.98	1.63	< -0.97
P12.YD2*	03:33:00.545	-27:41:46.80	29.25 ± 0.59	28.03 ± 0.14 (7.8σ)	> 28.44	1.22	< -0.41
ERS.YD1	03:32:23.369	-27:43:26.53	> 28.77	26.98 ± 0.15 (7.3σ)	27.87 ± 0.43	> 1.79	-0.89
ERS.YD2*	03:32:02.986	-27:43:51.95	> 28.39	26.98 ± 0.15 (7.3σ)	26.86 ± 0.17	> 1.41	0.12
ERS.YD3	03:32:29.790	-27:43:01.09	> 28.77	27.03 ± 0.16 (7.0σ)	27.83 ± 0.42	> 1.74	-0.80
ERS.YD4	03:32:40.904	-27:40:12.37	> 28.77	27.06 ± 0.16 (6.8σ)	27.96 ± 0.47	> 1.71	-0.90
ERS.YD5*	03:32:18.414	-27:43:45.99	> 28.77	27.06 ± 0.16 (6.8σ)	27.35 ± 0.27	> 1.71	-0.29
ERS.YD6	03:32:05.022	-27:45:53.93	28.61 ± 0.91	27.19 ± 0.18 (6.1σ)	27.38 ± 0.28	1.42	-0.19
ERS.YD7*	03:32:41.676	-27:41:27.48	> 28.03	26.95 ± 0.14 (7.6σ)	26.56 ± 0.13	> 1.08	0.39
ERS.YD8*	03:32:37.927	-27:42:20.78	> 28.14	27.14 ± 0.17 (6.3σ)	26.89 ± 0.18	> 1.00	0.25
ERS.YD9*	03:32:27.014	-27:44:31.29	> 28.57	27.20 ± 0.18 (6.0σ)	27.85 ± 0.43	> 1.37	-0.65

Table 3.2: Y-band drop out candidate $z \approx 8-9$ galaxies meeting our selection criteria in the HUDF, P12, P34 and ERS fields. Objects are divided by field and then ordered by apparent J_{AB} magnitude. Where the measured flux is $< 1\,\sigma$, an upper limit at the $1\,\sigma$ level is quoted. The significance of the J-band detection is shown in parentheses after the magnitude. Objects marked with * are more marginal candidates, see Section 3.2. The ERS field uses the narrower Y-band filter F098M, and the other fields use F105W. For the P34 field, we introduce a small offset to the astrometry in the HST image headers (given in Lorenzoni et al. http://arxiv.org/abs/1006.3545v1) of $\Delta RA = 0.03s$ to match the astrometry from GSC-2 and 2MASS.

$z \approx 8$

ID	RA	Dec	Y_{AB}	J_{AB}	H_{AB}	$(Y-J)_{AB}$	$(J-H)_{AB}$	$B11$	$L11$
GS.D-YD1	03:32:48.921	-27:47:07.36	27.0 ± 0.11	26.18 ± 0.063	26.17 ± 0.077	0.82	0.01	✓	
GS.D-YD2	03:32:14.135	-27:48:28.96	28.18 ± 0.3	26.94 ± 0.12	26.8 ± 0.13	1.24	0.14	✓	✓
GS.D-YD3	03:32:25.330	-27:48:54.07	27.18 ± 0.11	26.59 ± 0.086	26.9 ± 0.13	0.59	-0.31	✓	
GS.D-YD4	03:32:44.018	-27:47:27.23	27.8 ± 0.19	27.01 ± 0.13	26.97 ± 0.16	0.79	0.04	✓	
GS.D-YD5	03:32:40.257	-27:44:09.84	27.61 ± 0.18	27.09 ± 0.14	27.02 ± 0.16	0.52	0.07	✓	
GS.D-YD6	03:32:20.979	-27:48:53.46	29.04 ± 0.64	27.0 ± 0.13	27.05 ± 0.16	2.04	-0.05	✓	✓

Table 3.3: Y-band drop out candidate at $z \approx 8$ meeting either of the selection criteria described. Objects are ordered by apparent H_{AB} magnitude.

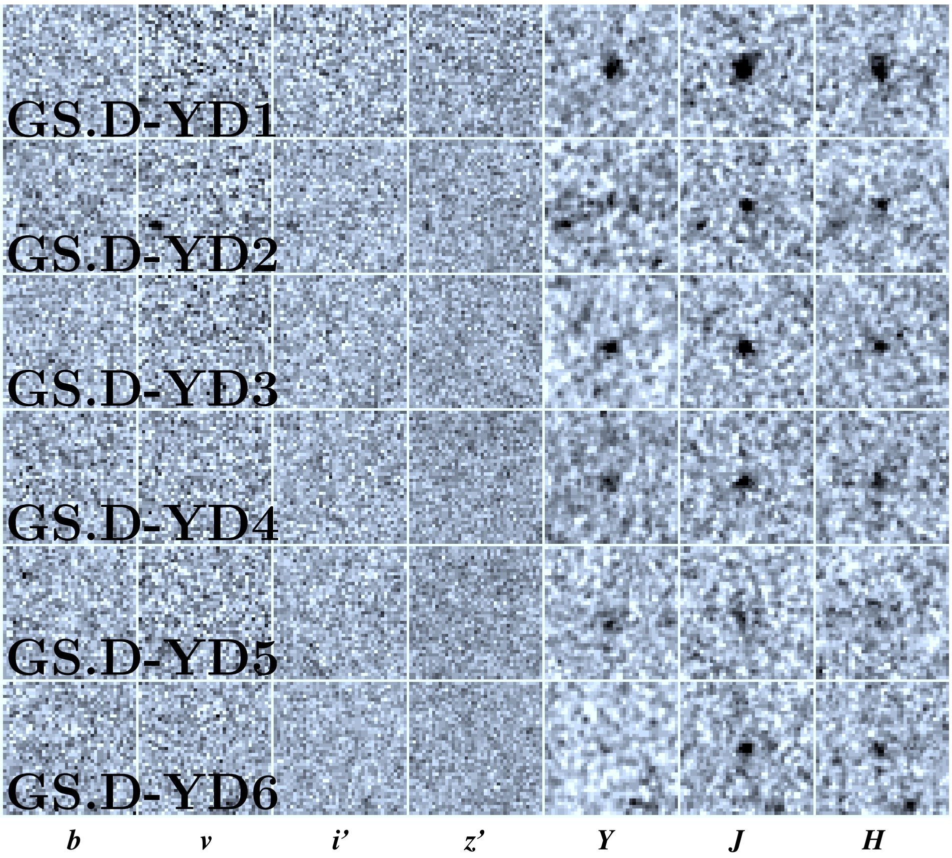

Figure 3.8: $2\farcs4 \times 2\farcs4$ $bvizYJH$ thumbnail images of potential $z \approx 8$ objects (Y-drops) meeting our selection criteria in CANDELS GOODS-South field, ordered by H-band magnitude (brightest at the top).

Now that the programme is complete, the UDF-P12 H-band is 1 magnitude deeper, and P12.YD1 and P12.YD2 are detected in that band at 3.7σ and 4.3σ, respectively. A further search on the complete Illingworth data has not been done yet (even though the images have been reduced and registered and are ready for inspection) because the programme was largely complete at the time of the original analysis, and the results would improve only marginally.

In the CANDELS-Deep field, 6 candidates have been found, all with colours compatible with Bouwens' selection window, with 2 of them also included in our more conservative window. No robust candidates were found in the CANDELS-Wide area.

3.2.4 Comparisons With Other Studies

In this section the list of high-redshift galaxy candidates is compared to the results from other groups.

3.2.4.1 z'-drops

The z'-drops found in the HUDF can be compared to several other results by Bunker et al. (2010), Oesch et al. (2010), Finkelstein et al. (2010), McLure et al. (2010) and Yan et al. (2010). Even though these works are based on the same data, different reduction techniques may result in slightly different final images; in addition, photometry is measured with different apertures and the selection criteria also vary. All the HUDF z'-drops found in Wilkins et al. (2011a) are selected by at least two other groups, however due to the differences just mentioned there are some candidates in the lists from other groups that were not selected by our criteria. Most of these objects lie outside the colour selection window used here, although some of them would satisfy our criteria if the photometry of the original study is adopted (rather than the photometry we measure in our reduction of the images). Other candidates are instead too faint for our brightness cut. Please refer to Wilkins et al. (2011a) for a detailed and exhaustive comparison with others groups' candidates in the HUDF.

At the time of submitting the paper on the CANDELS data analysis (Lorenzoni et al. 2012, *in press*), other groups had not published lists of z'-drops on the full GOODS-South data. Recently, Finkelstein et al. (2012) and Grazian et al.

(2012) have published their own z'-drops lists. The comparison of our candidates with theirs is not fully complete at the time of submission of this thesis and will be presented in future publications.

3.2.4.2 Y-drops

The list of Y-drops within the HUDF field from Lorenzoni et al. (2011) is now compared with other groups previous studies (Oesch et al. 2010, Bouwens et al. 2010a, McLure et al. 2010, Yan et al. 2010 and Finkelstein et al. 2010), and particularly with the first analysis of WFC3 data of the HUDF by our group (Bunker et al. 2010). A matched catalog between the Bunker et al. (2010), McLure et al. (2010) and Bouwens et al. (2010a) samples has already been presented in Bunker & Wilkins (2009).

The refined HUDF sample presented in Lorenzoni et al. (2011) and here, based on a MULTIDRIZZLE reduction of the HUDF data, has 6 Y-band drop-outs. In Bunker et al. (2010) a list of 7 Y-drop candidates within the HUDF field was presented, the brightest four (in J-band) of which are reproduced with the new selection (HUDF-YD1,2,3 & 4). Of the 3 other Y-drops from Bunker et al. (2010), one (YD5) has a discrepant $Y_{105w} - J_{125w} = 0.2$ colour in the new data reduction, much bluer than the adopted selection criteria of $Y_{105w} - J_{125w} > 0.9$. The faintest Y-drop in Bunker et al. (2010), YD7, is marginally too faint ($J = 28.65$) in the new reduction of the HUDF images to enter the new sample. However, applying our new colour selection criteria to the old photometry (where J = 28.44) would have resulted in the selection of YD7. The remaining one (YD6) is only marginally too blue for the Lyman-break selection in the newly-reduced data, with$Y_{105w} - J_{125w} = 0.89$, very close to the colour cut. This object also has slight ($\sim 2\sigma$) detections in the ACS bands, and lies in the corner cut out from the colour – colour selection box (i.e. it does not meet the selection criterion $(Y_{105w} - J_{125w}) > 0.73 \times (J_{125w} - H_{160w}) + 0.9$). Moreover, no other group has found or listed this object as a candidate.

Two objects in the new catalog (HUDF.YD8 and HUDF.YD9) were not found in Bunker et al. (2010); our previous study of Y-drops in the HUDF used slightly different magnitude and colour cuts ($J_{AB} < 28.5$ and $(Y - J)_{AB} > 1.0$), and an older reduction and photometric zeropoints. These two objects were slightly too faint in the previous version of our HUDF reductions ($J = 28.59$ and $J = 28.55$, respectively) and slightly too blue ($Y_{105w} - J_{125w} = 0.77, 0.92$ respectively) to be selected with the original criteria in Bunker et al. (2010). The new candidate HUDF.YD8 lies only 1 arcsec from the z'-drop zD5 in Bunker et al. (2010), and it is conceivable that both objects might be physically associated and might have similar redshifts at $z \approx 8$. We note that no other group has identified HUDF.YD9 as a candidate.

In Table 3.4 the Y-drop galaxy candidates from our HUDF catalog which have been previously reported with their corresponding catalog names from other groups are shown, while Table 3.5 presents all the objects found by these groups with colours or photometric redshifts compatible with being in our Y-drop redshift range, but which do not appear in our new catalog. Candidates that would be within our selection window if the photometry originally presented in the discovery papers was adopted are marked with a †.

Most of the other HUDF candidates from different groups do not meet our selection criteria both because they are too faint in the J-band (class 'A' in the Table 3.5) and because they are too blue, $(Y_{105w} - J_{125w}) < 0.9$ (class 'B' in

ID	Bo10	Bu10	M10	Y10	F10
HUDF-YD2	UDFy-37796000	YD2	1939y	z8-B117	200
HUDF-YD1	UDFy-42886345	YD1	1765y	z8-B092	819
HUDF-YD3	UDFy-38135539	YD3	1721y	z8-B115	125
HUDF-YD4	-	YD4	2487	-	-
HUDF-YD8	UDFy-43086276	-	2841y	z8-B088	653

Table 3.4: A list of Y-drops in the HUDF appearing in the catalogs of all previous analyses. We show in columns the different candidate ID used in this paper, in Bo10 (Bouwens et al. 2010a), Bu10 (Bunker et al. 2010), M10 (McLure et al. 2010), Y10 (Yan et al. 2010) and F10 (Finkelstein et al. 2010).

the Table 3.5). One candidate (z8-SB27 in Yan et al. 2010) meets our selection criteria for brightness in the J-band and the $(Y_{105w} - J_{125w})$ colour, but is rejected on the basis of its location in the the $(J - H)$ - $(Y - J)$ colour – colour plane as a likely lower redshift Balmer-break galaxy (see Figure 3.2). This galaxy is classified with letter ‘C’ in the table. It is noted that Bouwens’ candidate UDFy-37636015 (YD7 in Bunker et al. (2010)) has inconsistent photometry presented in Bouwens et al. (2009) and Bouwens et al. (2010a) – adopting the more recent photometric values from Bouwens et al. (2010a), YD7 would enter our Y-drop selection (Table 3.5).

In summary, our latest reduction of the WFC3 images of the HUDF allows us to reproduce 4 of the 7 Y-band dropout galaxies first reported in Bunker et al. (2010); of two additional Y-drops in the new analysis, one has been reported elsewhere and one is a new discovery in the HUDF field. Remeasuring the photometry of Y-drop candidates presented elsewhere by other groups, most would not enter our selection as they are too faint in J-band and/or are too blue in $(Y - J)$, and hence are not as robust candidate $z \approx 8 - 9$ galaxies as our core sample.

Bunker '10	M10	F10	Y10	Bo10	Class
YD5†	-	-	z8-SD24	-	AB
YD6†	-	-	-	-	
YD7†	2079y	213	z8-B114	y37636015	AB
-	1107z**	-	-		B
-	1422	2055	z8-B041c†		B
-	-	800*	-		B
-	-	3022	-		AB
-	-	640	-		B
-	-	-	z8-B094†		
-	-	-	z8-B087†		
-	-	-	z8-SB27		C
-	-	-	z8-SB30		B
-	-	-	z8-SD05		AB
-	-	-	z8-SD02		AB
-	-	-	z8-SD15		AB
-	-	-	z8-SD52		AB

† Object that would meet our selection criteria, assuming original photometry.

* Object 800 appears in versions 1,2 & 3 of the arXiv:0912.1338 version of Finkelstein et al. (2010), but is absent from version 4 and the Astrophysical Journal paper.

** Object also found by Oesch et al. (2009), named UDFz-44716442 and classified as a z'-drop. We included this object in our table since McLure et al. (2010) quote a photometric redshift of 7.60, on the edge of our selection range.

Table 3.5: List of candidates from other studies of the HUDF (see Table 3.4) quoted by respective authors to be either a Y-drop or in our redshift range ($7.6 < z < 9.8$, see Section 3) but that we do not recover. Class A denotes objects too faint in J-band ($J_{AB} > 28.51$). Class B means that the colour selection criterion $(Y_{105w} - J_{125w}) > 0.9$. was not met. Class C is where the $(J - H)$:$(Y - J)$ colour:colour rules out selection (i.e., $(Y_{105w} - J_{125w}) > 0.73 \times (J_{125w} - H_{160w}) + 0.9$ is not met). Objects marked † would meet our selection criteria if we adopt the original photometry (but which do not make our selection if we use the photometry from our new reduction of the imaging data).

Both the 'deep' and 'wide' CANDELS observations of GOODS-S have been recently searched for $Y_{105\mathrm{w}}$-drop candidates by both Oesch et al. (2012b, hereafter O12) and Yan et al. (2011, hereafter Y11), resulting in 11 and 8 high redshift galaxy candidates respectively.

Only 3 of the 11 O12 sources are matched by our 6 candidates. Another object in our sample (GS.D-YD3) is also flagged as a *potential* candidate by O12 (CAND-2253348542) though is dismissed by O12 on the grounds of its stellar-like profile. An additional 2 of the candidates presented in Lorenzoni et al. (2012, in press) and here match with the 8 Y11 sources, thus all the candidates presented also exist in either O12 or Y11 (see Table 3.6).

However, there are no matches in common between all three candidate lists, so it is useful to examine each of the O12 and Y11 candidates in turn to identify why they were not selected by us.

Of the 8 O12 sources not selected here as candidates, 2 objects, CANDY-2499448181 (which is also 048 in Y11) and CANDY-2209651371, are detected at $> 2\sigma$ in a single optical band (at $< 3\sigma$).

One object (CANDY-2320345371) is excluded because its $(Y_{125\mathrm{w}} - J_{160\mathrm{w}})$ colour is slightly bluer than our selection window, while a further 4 sources fail to meet the S/N$>$ 5 criterion though do appear to be real objects (all detected at $> 4\sigma$ in both $J_{125\mathrm{w}}$ and $H_{160\mathrm{w}}$). A single source (CANDY-219147298) is not matched within $0.5''$ of an object in our catalogue. Of the 6 Y11 sources not matched to our candidates the two brightest (048 and 100) are excluded on the basis of weak (2 to 3σ) optical detections in a single band. The 4 remaining objects are excluded on the basis of S/N concerns (in that they fall below S/N$=$ 5 in one or both bands); in three cases (094, 035, 043) the source is detected at $> 4\sigma$ in both $J_{125\mathrm{w}}$ and $H_{160\mathrm{w}}$ while the final object (085) is only detected at $2 - 3\sigma$ and has colours inconsistent with our selection window.

There are then two principal reasons for the Y11 and O12 objects being excluded from our candidate lists; at the bright-end 2 objects in each study (with 1 in common) are excluded due to weak (2 to 3σ) optical detections in single band; while at the faint end several sources are excluded on the basis of our S/N criteria. In all but one case (Y11: 085) these objects are detected at $> 4\sigma$ in both $J_{125\mathrm{w}}$ and $H_{160\mathrm{w}}$ and have observed colours consistent with our selection window. It then seems possible that some of the additional Y11 and O12 candidates are potential high-redshift star forming galaxies. However, these objects are nevertheless excluded from the subsequent analysis of the rest-frame UV luminosity function, as we want a robust sample. The computation of the effective volume takes into account the more conservative selection criteria used in this work, which should lead to the accurate luminosity function being recovered.

Lorenzoni '12	Oesch '12	Yan '11	Class
GS.D-YD1	-	064	
GS.D-YD2	CANDY-2141348289	-	
GS.D-YD3	CANDY-2253348542	-	
GS.D-YD4	CANDY-2440247273	-	
GS.D-YD5	-	107	
GS.D-YD6	CANDY-2209848535	-	
-	CANDY-2499448181	048	O
-	CANDY-2320345371	-	W
-	CANDY-2209651371	-	O
-	CANDY-2350049216	035	F
-	CANDY-2192147298	-	?
-	CANDY-2181852456	-	F
-	CANDY-2379552208	-	F
-	CANDY-2408551569	-	F
-	-	100	O
-	-	094	F
-	-	043	F
-	-	085	F, W

F - Object too faint in $J-$ and/or $H-$band for our selection criteria.
O - Detection of more than $2\,\sigma$ in at least one of the optical bands.
W - Object outside our colour-colour selection windows.
? - Object not picked up by SExtractor.

Table 3.6: We list here candidates identified by Oesch et al. (2012) and Yan et al. (2011), second and third column respectively, and match them with ours when possible (first coloumn) or give the reason why we do not find them (fourth coloumn).

Chapter 4

Analysis - Luminosity function derivation

From the observed surface density of drop-outs as a function of magnitude, the luminosity function of $z \approx 7$ and $z \approx 8$ galaxies in the rest-frame ultraviolet (observed by the WFC3 near-infrared filters) can be recovered. In order to do that, the probability of recovering a high-redshift galaxy as a function of redshift and magnitude is calculated. This probability is integrated to obtain the effective volume probed, and a Schechter LF can be then fitted to the data.

The sensitivity over the redshift range probed by the Lyman-break technique is not uniform: some of the galaxies at the lower end of this range could be missed because of photometric scatter (carrying them out of the colour selection window), while in the same way, some galaxies with a lower redshift than that probed could be included in the sample. This effect is stronger if the filters between which the drop is expected are overlapping. At the higher redshift end a different effect influences the sensitivity: the higher the redshift, the more the Lyman-α forest absorption affects the filter longwards of the break (Y-band filter for z'-drops, J-band filter for Y-drops) meaning that only the most UV-luminous galaxies will have enough flux in this band to satisfy the $z-Y$ or $Y-J$ (for z'-drops and and Y-drops respectively) selection criterion. As a result, apart for the very bright objects, the sensitivity will drop towards the higher redshift end of the probed range, this drop being more significant for fainter sources. Photometric scatter will affect this end of the range as well.

4.1 Completeness simulations

The probability of recovering a high-redshift galaxy as a function of redshift and rest frame UV luminosity can be found with simulations: artificial sources with properties similar to those of the galaxies observed at high-redshift (i.e. compact with half-light radii $r_{hl} \approx 0.''1$, large Lyman-α forest decrement of $D_A \approx 0.99$ and blue rest-frame UV colours) are added to the images and the selection process is applied to these modified frames, making it possible to evaluate the percentage of recovered sources. The fake galaxies used in this work are Gaussian profiles have FWHM varying between $0.''1$ and $0.''3$, and a Gaussian distribution of spectral slopes, $\langle\beta\rangle = -2.2$ and $\sigma(\beta) = 0.5$, reflecting the generally blue spectral slopes observed in Lyman-break galaxies at $z \geq 6$ (Stanway, McMahon & Bunker 2005; Bouwens et al. 2010b; Wilkins et al. 2011b; Bunker et al. 2010).

The deduction of the expected colours is described in section 3.2. The fake sources are introduced with a range of different magnitudes in random positions in the images, although avoiding bright objects and areas were the image is not as deep as the average (mainly edges). SExtractor is then run in the exact same way as for the candidate selection, and the photometry of the objects picked up by the program in the locations where the fake galaxies were inserted are compared to their original synthetic photometry. The probability $p(M, z)$ of finding a galaxy with absolute magnitude M and redshift z can be determined (Figure 4.1), and the effective volume V_{eff} probed can be calculated with the approach used in Steidel et al. (1999) and Stanway, Bunker & McMahon (2003), where the volume is given by:

$$V_{eff}(M) \propto \int dz\, p(M, z)\, \frac{dV}{dz} \tag{4.1}$$

where $dz\, \frac{dV}{dz}$ is the comoving volume per unit solid angle in a slice dz at redshift z. Since the effective volume is a function of the absolute magnitude M, it can be calculated for different magnitude bins, and the observed surface density of objects can be converted to a number density, allowing a stepwise luminosity function to be built.

4.2 Luminosity function fitting

The best-fit to this stepwise luminosity function can then be determined. A Schechter luminosity function is assumed, for which the number density of galaxies between luminosity L and $L + dL$ is:

$$\phi(L)dL = \phi^* \left(\frac{L}{L^*}\right)^{\alpha} e^{(-L/L^*)}\, d(L/L^*) \tag{4.2}$$

where ϕ^* is the normalisation parameter, L^* the characteristic luminosity at the knee of the function and α is the slope of the faint end of the function. Given that

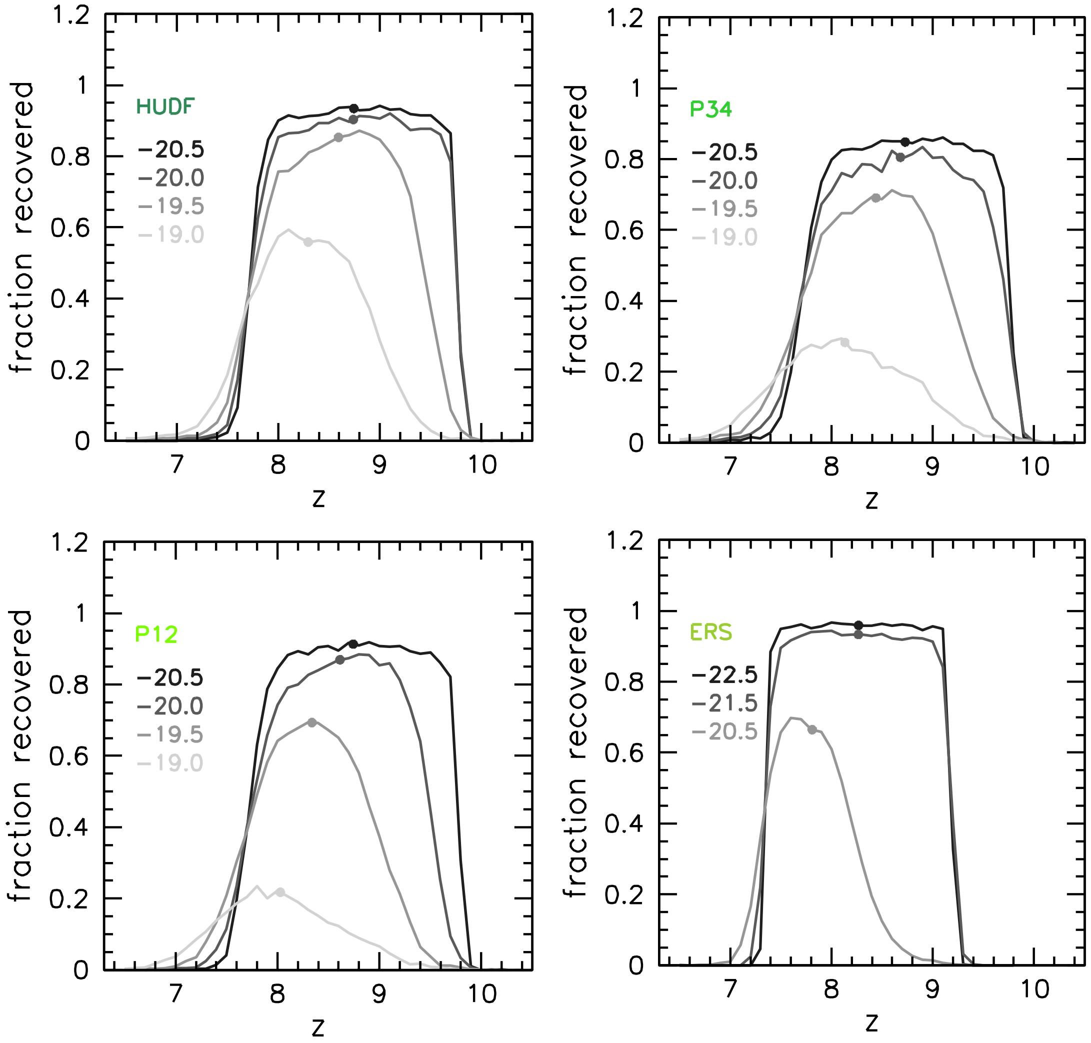

Figure 4.1: The probability of recovering simulated galaxies as a function of redshift z for a number of absolute rest-UV magnitudes (M_{1600}) for HUDF, UDF-P34, UDF-P12 and ERS. The mean redshift is denoted by a dot.

the only light we observe is the UV light, the luminosity functions presented here are in fact UV luminosity functions. The Schechter function can be written as a function of absolute magnitude instead of luminosity, considering the relations:

$$\phi(M)dM = \phi(L)d(-L) \tag{4.3}$$

and

$$M - M^* = -2.5\,log\left(\frac{L}{L^*}\right) \tag{4.4}$$

and substituting them into equation 4.2:

$$\phi(M)dM = (0.4\,ln10)\,\phi^*\,10^{0.4(\alpha+1)(M^*-M)}\,e^{-10^{0.4(M^*-M)}}dM \tag{4.5}$$

with M^* the corresponding absolute magnitude to the luminosity L^*.

Given the faintness of galaxies below L^* at the redshifts probed in this study, it is not possible to strongly constraint the faint-end slope of the Schechter LF, α, so the fit to the data has been performed with ϕ^* and M^* as free parameters for different fixed values of α. The values used in the analysis of the fields ERS, HUDF and flanking fields are -1.5, -1.7 and -1.9: these values were selected as they bracket the value $\alpha = -1.73$ derived by Bouwens et al. (2006) for the i-drops at $z = 6$ and for the $z = 3$ U-drops (Reddy & Steidel 2009). For the analysis of the CANDELS area, the value -2.1 for α was also considered for ease of comparison, as other groups (Trenti et al. 2011, Bouwens et al. 2011, Oesch et al. 2012b, Bradley et al. 2012) seem to favour an α of around -2. We note that faint end slopes steeper than $\alpha = -2$ result in divergent luminosity densities (i.e. infinite if integrated down to zero luminosity). It is still unclear what lower luminosity limit should be taken for the Schechter function integral.

4.2.1 HUDF, P34, ERS

Not all of the Y-drops listed in Table 3.2 are used to calculate the luminosity function: while all these candidates are good targets for spectroscopy, the sample used for determining the luminosity function was restricted to only the most

α	M^*_{1600} [AB mag]	ϕ^* [Mpc^{-3}]
-1.5	-19.34	0.00117
-1.7	-19.5	0.00093
-1.9	-19.66	0.00070

Table 4.1: The best fit values of M^*_{1600} and ϕ^* for a Schechter function assuming fixed $\alpha \in \{-1.5, -1.7, -1.9\}$ at redshift $z \approx 8$.

reliable sources to minimize biases through contamination by photometric scatter. Only the candidates detected at $\geq 7\sigma$ in the J-band were included in the LF derivation, with the exception of ERS.YD2 and ERS.YD7 (both marked as marginal, see Chapter 3) and of the two candidates found in the P12 flanking field due to the shallow H-band imaging.

The data from ERS and HUDF fields were fitted with the reduced-χ^2, χ^2_{red}, method:

$$\chi^2_{red} = \frac{1}{K} \sum_{i=1}^{n} \frac{(x_i - \mu_i)^2}{\sigma^2} \tag{4.6}$$

where x_i is the observed value for the ith bin, μ_i the expected value for the ith bin, n is the number of bins, σ^2 is the variance and K the number of degrees of freedom. $K = n - v - 1$, with v number of free parameters estimated to determine the best fitting distribution, two in our case (M^* and ϕ^*).

The parameters values minimising χ^2_{red} for the different values of α are shown in Table 4.1. Figure 4.2 shows the fitted luminosity function and the data points used in its derivation compared to lower redshift results, while Figure 4.3 shows the significance contours for the reduced χ^2 fits of the UV luminosity function at $z \approx 7$ (Wilkins et al. 2011a, blue line) and $z \approx 8$ (green contours).

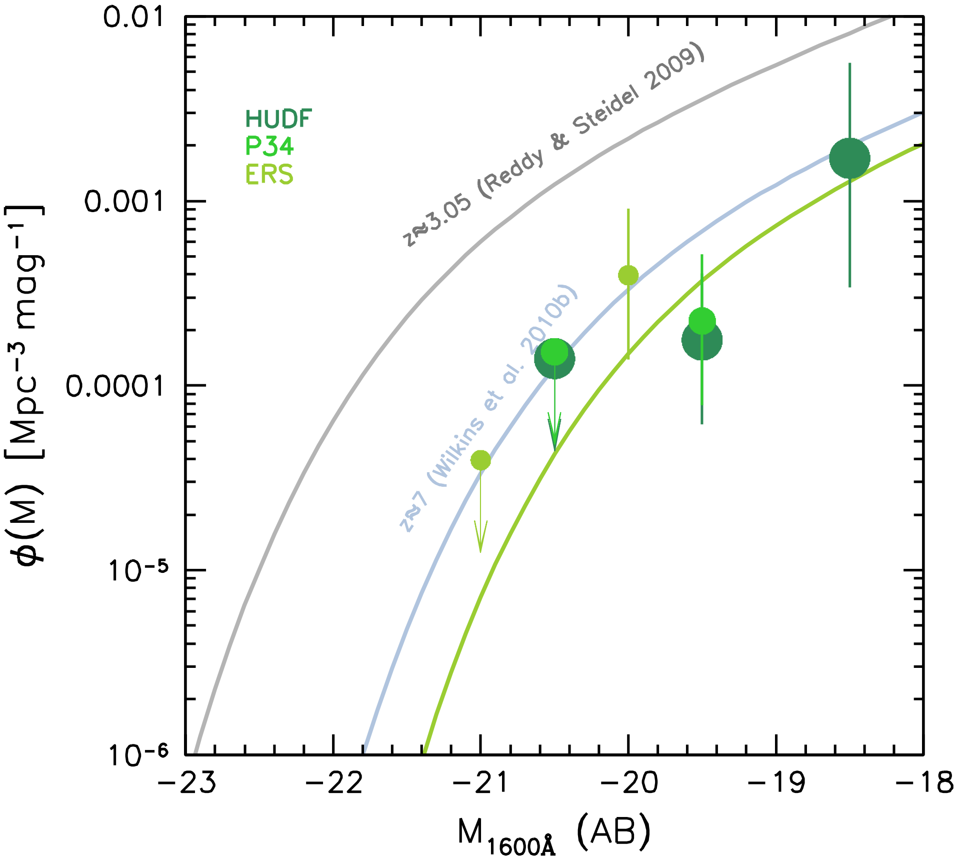

Figure 4.2: The $z \approx 8-9$ rest-frame UV (1600Å) luminosity function (green line) derived from HUDF, UDF-P34 and ERS WFC3 fields together with contemporary and lower-redshift comparisons. Grey and blue lines denote the luminosity function at $\langle z \rangle \approx 3.05$ (Reddy & Steidel 2009) and $\langle z \rangle \approx 7.0$ (Wilkins et al. 2011a).

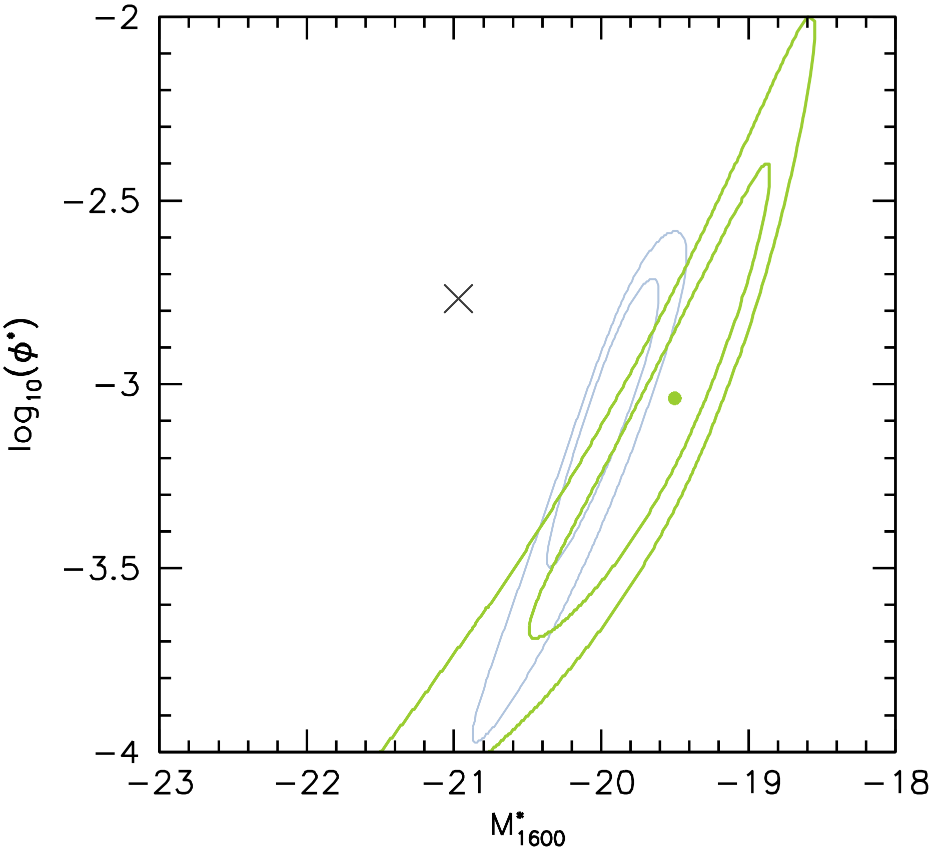

Figure 4.3: The significance contours for the reduced-χ^2 fits of the Schechter UV luminosity function for the Y-drops (green contours on right, signifying reduced-$\chi^2 = 1$ and 2 for the inner and outer). A faint end slope of $\alpha = -1.7$ has been assumed, and the dot is the formal best fit, with $M^*_{1600} = -19.5$ (AB). The blue contours (to the left of the $z = 8$ contours) denote the $z = 7$ luminosity function derived by Wilkins et al. (2011a) from the z'-drops in the same WFC 3 fields as analysed here. The cross (on the left) denotes the best fit Schechter parameters for Lyman-break galaxies at $z = 3$ (Reddy & Steidel 2009). Evolution predominantly in M^* is most consistent with the observational data.

4.2.2 CANDELS

For the CANDELS data set, the maximisation of Poissonian log-likelihood was used instead of the reduced χ^2: because of the small number of expected observations, especially for the Y-drops, the Poissonian distribution is better suited to describe the statistics of the counts than the normal distribution.

The probability of obtaining a certain number of events in the ith bin is given by:

$$P_i(x_i; \mu_i) = \frac{\mu_i^{x_i} e^{-\mu_i}}{x_i} \tag{4.7}$$

with x_i the observed value for the ith bin and μ_i the expected value for the ith bin. The joint probability is therefore

$$\mathcal{L} = \prod_{i=1}^{n} P_i = \prod_{i=1}^{n} \frac{\mu_i^{x_i} e^{-\mu_i}}{x_i!} \tag{4.8}$$

For computational reasons, it is convenient to take the logarithm of the likelihood so that the product becomes a sum:

$$\ln \mathcal{L} = \sum_{i=1}^{n} \ln \left(\frac{\mu_i^{x_i} e^{-\mu_i}}{x_i!} \right) = \sum_{i=1}^{n} (x_i \ln \mu_i - \mu_i - \ln(x_i!)) \tag{4.9}$$

this quantity, generally negative, is easier to maximise than the non-logarithmic likelihood. In case of a high number counts ($x_i \geq 15$) the Stirling approximation $\ln(n!) = n \cdot \ln(n) - n$ is used for the last term.

The maximization of the log-likelihood (or rather the minimization of its inverse, $-\ln \mathcal{L}$) has been performed for both z'- and Y-drops and for both the selection windows employed in each case. The best fit parameters for fixed values of α used are shown in Tables 4.2 and 4.3 for $z \approx 7$ and $z \approx 8$ respectively.

$\mathbf{z \approx 7}$

	W11		B11z	
α	M^*_{1600} [AB mag]	ϕ^* [Mpc^{-3}]	M^*_{1600} [AB mag]	ϕ^* [Mpc^{-3}]
-1.5	-19.75	0.00152	-19.75	0.00159
-1.7	-19.95	0.00110	-19.93	0.00119
-1.9	-20.19	0.00072	-20.14	0.00081
-2.1	-20.51	0.00039	-20.40	0.00049

Table 4.2: The best fit values for M^*_{1600} and ϕ^* at $z \approx 7$ for a Schechter function assuming fixed $\alpha \in \{-1.5, -1.7, -1.9, -2.1\}$ for both the W11 (columns 2 and 3) and B11z (columns 4 and 5) selection windows.

$\mathbf{z \approx 8}$

	L11		B11Y	
α	M^*_{1600} [AB mag]	ϕ^* [Mpc^{-3}]	M^*_{1600} [AB mag]	ϕ^* [Mpc^{-3}]
-1.5	-19.10	0.00143	-19.42	0.00088
-1.7	-19.23	0.00119	-19.53	0.00075
-1.9	-19.37	0.00095	-19.66	0.00060
-2.1	-19.54	0.00069	-19.80	0.00046

Table 4.3: The best fit values for M^*_{1600} and ϕ^* at $z \approx 8$ for a Schechter function assuming fixed $\alpha \in \{-1.5, -1.7, -1.9, -2.1\}$ for both the L11 (columns 2 and 3) and B11Y (columns 4 and 5) selection windows.

In Figures 4.4 and 4.5 the obtained data points at $z \approx 7$ and $z \approx 8$, respectively, are plotted against several previous estimates of luminosity functions at the same redshifts. The figures show the number densities obtained with both W11/L11 (open circles) and B11z/B11Y (filled circles) selection windows. The agreement of the two sets of data is good, implying that the simulations and volume calculations are accurate and do account for the use of different colour selection windows. The best fit values for the Schechter parameters at $z \approx 7$ obtained with the different colour selections are also in very good agreement: for α values of -1.5, -1.7 and -1.9, M^* values of the different selections are within 0.05 magnitudes, and ϕ^* is within 10%, while in the case of $\alpha = -2.1$ there is a difference of 0.1 magnitudes for M^* and about 20% for ϕ^*. The 68% and 95% likelihood contours of the values of M^* and ϕ^* obtained for the B11z/B11Y selection windows for $z \approx 7$ (dashed) and $z \approx 8$ (solid) are shown in Figure 4.6.

At $z \approx 8$ there is less good agreement between the results obtained with the two windows. This is due to the extremely small number of populated bins (3) in the Schechter LF fit to the data for the L11 selection window.

4.3 Comparison with other studies

There are several independent derivations of luminosity function in the literature at $z \approx 7$ and $z \approx 8$ to which the results presented here can be compared.

4.3.1 $z \approx 7$

In Figure 4.4 the data from this work are compared to two previous estimates of the $z \approx 7$ luminosity function, Wilkins et al. (2011a) and Bouwens et al. (2011),

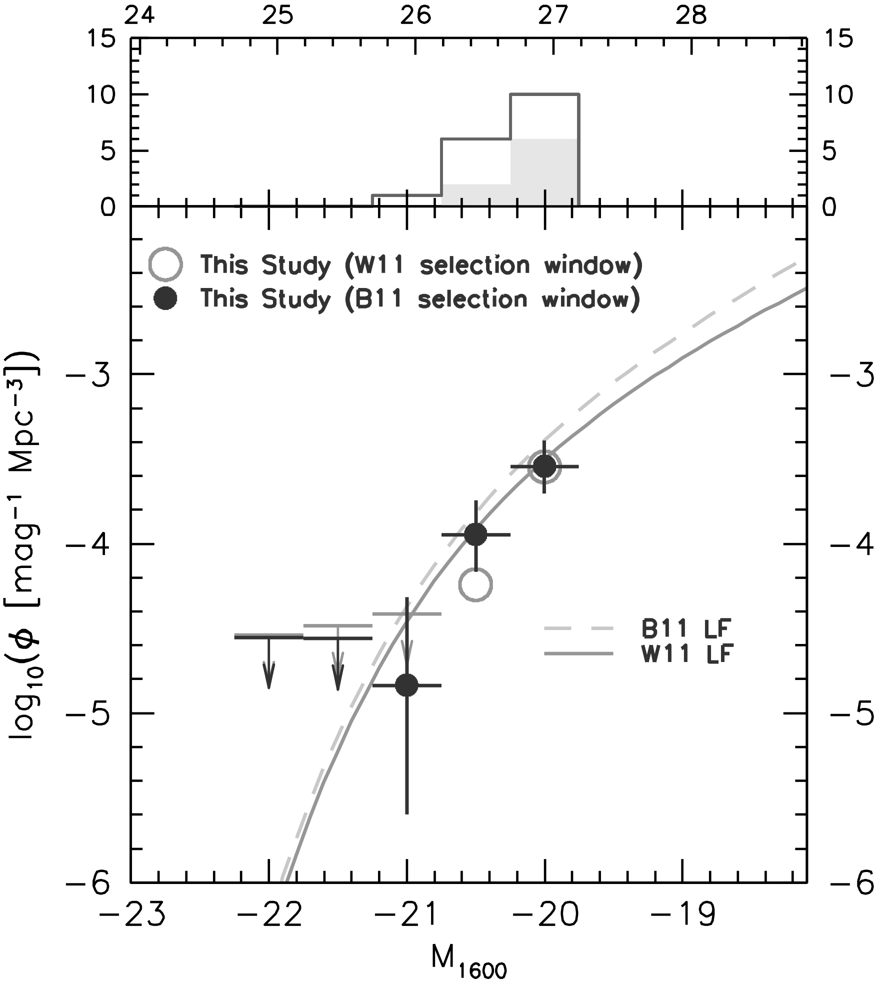

Figure 4.4: Top panel: the luminosity distribution of the selected candidates. The grey area represents the W11 selection. Bottom panel: luminosity function of z'-drop selected sources at $z \approx 7$. Our datapoints are plotted against Wilkins et al. (2011a, solid line) and Bouwens et al. (2011, dashed line) luminosity functions. The uncertainty bars represent the 68.2% poissonian confidence interval of the number density ϕ. The upper limits denote the maximum value of the 68.2% confidence interval with $n = 0$ observations. This corresponds roughly to $n = 1.84$, i.e. the for an observed $n = 0$ there is a 68.2% chance the true value is < 1.84.

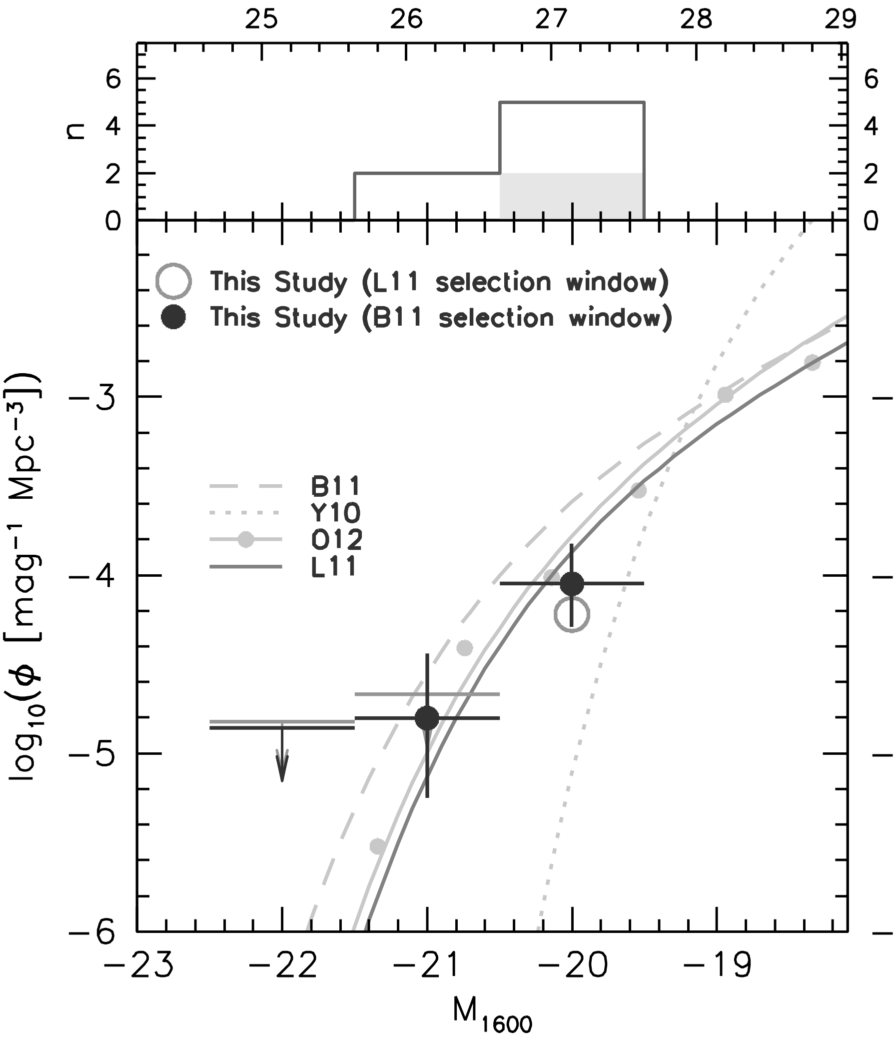

Figure 4.5: Top panel: the luminosity distribution of the selected candidates. The grey area represents the L11 selection. Bottom panel: luminosity function of Y-drop selected sources at $z \approx 8$. Our datapoints are plotted against several luminosity functions: Lorenzoni et al. (2011, solid dark line), Oesch et al. (2012b, solid light line), Bouwens et al. (2011, dashed line) and Yan et al. (2010, dotted line). The uncertainty bars represent the 68.2% poissonian confidence interval of the number density ϕ. The upper limits denote the maximum value of the 68.2% confidence interval with $n = 0$ observations. This corresponds roughly to $n = 1.84$, i.e. the for an observed $n = 0$ there is a 68.2% chance the true value is < 1.84.

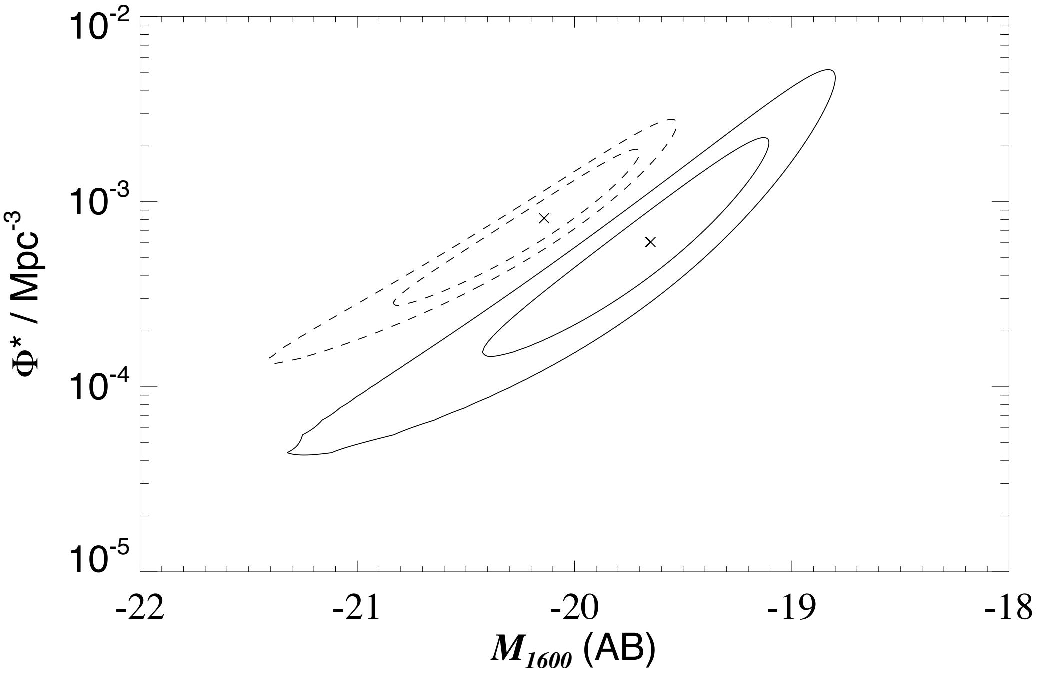

Figure 4.6: The likelihood contours for the luminosity function of z'-drops (dashed lines) and Y-drops (solid lines), showing the correlation between the fitted M^* and ϕ^* parameters for a Schechter function fit, using our sample of galaxies from the B11 colour selection. A faint-end slope of $\alpha = -1.9$ is adopted here. The 68% (inner) and 95% (outer) likelihood contours are shown. The cross represents the best-fit parameter values.

both from the HUDF and ERS data described earlier, showing good agreement. Table 4.4 shows the best fit Schechter LF parameters of Wilkins et al. (2011a), Bouwens et al. (2011), McLure et al. (2010), obtained from the same data, Ouchi et al. (2009), from *Subaru* Suprime-Cam wide field observations of the Subaru Deep Field (SDF, Kashikawa et al. 2004) and GOODS-North, and Castellano et al. (2010), using VLT Hawk-I data of the GOODS-South.

The results obtained with the whole data set presented in this work are in very good agreement with Wilkins et al. (2011a), and also with Bouwens et al. (2011)

Comparison of $z \approx 7$ LF Determinations in the Literature

Ref.	α	M^*_{1600} [AB mag]	ϕ^* $[10^{-3}\mathrm{Mpc}^{-3}]$
This work	-1.7 (fixed)	-19.93	1.19
Wilkins et al. (2011a)	-1.7 (fixed)	-19.9	1.06
Bouwens et al. (2011)	-2.01 ± 0.21	-20.14 ± 0.26	$0.86^{+0.70}_{-0.39}$
McLure et al. (2010)	-1.72	-20.11	0.7
Ouchi et al. (2009)	-1.72 ± 0.65	-20.10 ± 0.76	$0.69^{+2.62}_{-0.55}$
Castellano et al. (2010)	-1.71 (fixed)	-20.24 ± 0.45	$0.35^{+0.16}_{-0.11}$

Table 4.4: Our best-fit parameters for a Schechter LF at $z \approx 8$ are compared with other groups results at the same redshift.

considering our best fit parameters for $\alpha = -1.9$ (Table 4.2). The McLure et al. (2010) best fit parameters, especially ϕ^*, are a bit different from ours, although well within the 1σ confidence contour (inner blue line in Figure 4.3). Since the other two LF estimations come from wider surveys apt to detect brighter candidates, it is therefore more useful to compare their stepwise LF determinations to the LF derived here. Doing so, both Ouchi et al. (2009) and Castellano et al. (2010) LF determinations are in agreement with the luminosity function derived in this work.

4.3.2 $z \approx 8$

In Figure 4.5 our recent data are compared to several previous luminosity functions obtained in recent years by us and other groups: Lorenzoni et a. (2011), Oesch et al. (2012b), Bouwens et al. (2011) and Yan et al. (2010). In Table 4.5 the best fit Schechter parameters from these publications are listed, along with the McLure et al. (2010) and Bradley et al. (2012) estimations.

All the estimations used for comparison come from the HUDF and ERS fields

Comparison of $z \approx 8$ LF Determinations in the Literature

Ref.	α	M^*_{1600} [AB mag]	ϕ^* [10^{-3}Mpc^{-3}]
This work	-1.9 (fixed)	-19.66	0.60
Lorenzoni et al. (2011)	-1.9 (fixed)	-19.66	0.70
Oesch et al. (2012b)	$-2.06^{+0.35}_{-0.28}$	-20.04 ± 0.26	$0.50^{+0.70}_{-0.33}$
Bouwens et al. (2011)	-1.91 ± 0.32	-20.10 ± 0.52	$0.59^{+1.01}_{-0.37}$
Yan et al. (2010)	-1.80	-17.80	7.6
McLure et al. (2010)	-1.71 (fixed)	-20.04 (fixed)	0.35
Bradley et al. (2012)	$-1.98^{+0.23}_{-0.22}$	$-20.26^{+0.29}_{-0.34}$	$0.43^{+0.35}_{-0.21}$

Table 4.5: Our best-fit parameters for a Schechter LF at $z \approx 8$ are compared with other groups results at the same redshift.

apart from the Bradley et al. work, which combines their data from BoRG with the data from Bouwens et al. (2011).

With the exception of Yan et al. (2010), all works show a broad agreement, even though the results presented here tend to favour a slightly fainter M^* than the other groups. However, the degeneracy between M^* and ϕ^* and the large uncertainties (Figure 4.6) make this result compatible (within 1σ) with the others. On the other hand, the Yan et al. (2010) LF is strongly ruled out: with respect to the results of this thesis, Yan et al.'s M^* is 2 magnitudes fainter and ϕ^* a factor of ten higher. It seems likely that Yan et al. (2010) recorded erroneously large numbers of very faint objects, which are either spurious or the extended haloes of brighter extended lower-redshift objects which were mis-identified as separate sources through S-Extractor deblending (see Bouwens et al. 2011 for a critique)

4.4 LF evolution

There are clear signs of evolution of the UV luminosity function of galaxies at redshift $z \approx 3$ (Reddy & Steidel, 2009) to redshift 6 (Stanway, Bunker & McMahon 2003, Bunker et al. 2004, Bouwens et al. 2007). All the works at $z \approx 7$ presented in Table 4.4 agree in finding evolution of the LF from various estimates at $z \approx 6$, for example the Bouwens et al. (2007) i-drop LF at $z \approx 6$ has best fit Schechter parameters $\alpha = -1.74 \pm 0.16$, $M^* = -20.24 \pm 0.19$, $\phi^* = 1.4^{+0.6}_{-0.4} \times 10^{-3}$ Mpc^{-3}. M^* is fainter at higher redshifts, implying a smaller number of bright galaxies, and ϕ^* is smaller, indicating lower number densities over the whole magnitude range. The groups fitting for α favour a very steep faint-end slope, reaching values of ~ -2. For $\alpha \leq -2$ the Schechter function would diverge, giving an infinite luminosity density, if integrated to zero luminosty; however, galaxies are not expected to form at indefinitely faint magnitudes.

The determination of α from the observations available to date is affected by very large uncertainties (compatible with no evolution from $z \approx 3$) as this parameter is derived from its weak effect on the bright end of the LF, while it characterises the faint end. Given the empirical nature of the Schechter LF, it is not obvious that the parameter that fits well the faint end slope for $M >> M^*$ is significant at the bright end as well, even though it formally influences it.

At $z \approx 8$, the results shown in Table 4.5 suggest further evolution from $z \approx 7$ (ignoring the discrepant result of Yan et al.). In Figures 4.2 and 4.3 can be seen, along with the clear evolution from $z \approx 3$ (Reddy & Steidel 2009) to $z \approx 7$ (Wilkins et al. 2011a), that even considering the large error bars/contours it is likely that evolution continues to $z \approx 8$. The estimations of this work are entirely consistent with an evolution mainly in M^* (even from $z \approx 3$), with only a modest change in ϕ^* (consistent with no change in ϕ^*). A pure ϕ^* evolution from $z \approx 7$ to $z \approx 8$ is however marginally consistent within 1σ.

Chapter 5

Implications for reionization

By integrating the luminosity function, the ultraviolet luminosity density can be obtained, which is directly connected with the star formation rate density. The SFR density obtained from observations can then be compared to that required for reionization.

5.0.1 The Star Formation Rate Density at $z \approx 7$ and $z \approx 8$

The UV continuum emission of a star-forming galaxy is dominated by main sequence O and B stars. These are massive stars ($\gtrsim 10 M_\odot$) with short lifetimes (main sequence time, $t_{MS} \lesssim 2 \times 10^7$ years), so the observed UV luminosity L_{UV} is proportional to the stellar birthrate. When the UV flux reaches a steady state ($t >> t_{MS}$), in the absence of extinction by dust the following relation (Madau, Pozzetti & Dickinson, 1998) is valid:

$$L_{UV} = \text{const} \cdot \frac{\text{SFR}}{M_\odot \ \text{yr}^{-1}} \ \text{ergs s}^{-1} \ \text{Hz}^{-1} \tag{5.1}$$

where const is a constant equal to 8.0×10^{27} for UV emission at 1500 Å (restframe), which is the light that is observed in the J- and H-band for objects at $z \approx 7-8$, respectively. This value assumes a Salpeter (1955) IMF, while for a Scalo (1986) IMF const $= 3.5 \times 10^{27}$ at the same wavelength, meaning that for the same observed L_{UV} a Scalo IMF would imply a higher SFR of a factor of ~ 2. Both IMFs used in Madau, Pozzetti & Dickinson (1998) are truncated at 0.1 and $125 M_{\odot}$, and the metallicity is fixed to solar values. The constant is also quite insensitive to the past star formation history. The relation 5.1 is comparable to the relation derived from the models of Leitherer & Heckman (1995) and Kennicutt (1998).

The UV luminosity density can be derived from the integration of the Schechter luminosity function:

$$\rho_{UV} = \int_{L_{lim}}^{\infty} L \cdot \phi_{UV}(L) dL \tag{5.2}$$

where L_{lim} is the luminosity limit down to which the LF is integrated. Through the linear relation 5.1, the UV luminosity density can be converted to the star formation rate density. In Tables 5.1 and 5.2 the UV luminosity densities and star formation rates for the different values of α and L_{lim} at $z \approx 7$ and $z \approx 8$, respectively, are shown. In Figures 5.1 and 5.2 the same quantities are plotted against the lower luminosity limit. The grey-shaded boxes in these figures delimit the magnitude range probed by observations: it is clear that α does not affect the SFR density determination for integrations down to the observable limit (as can be seen in the aforementioned tables too), while its influence increases as the extrapolation is pushed towards fainter magnitudes. It is still not clear what L_{lim}

α	$\rho_{1600}\,[10^{25}\,\mathrm{erg\,s^{-1}\,Mpc^{-3}\,Hz^{-1}}]$ ($\dot{\rho}_*\,[\mathrm{M_\odot\,yr^{-1}\,Mpc^{-3}}]$)		
	$M_{1600} < -18.5$ (SFR $> 1.5\,\mathrm{M_\odot\,yr^{-1}}$)	< -13 ($> 0.01\,\mathrm{M_\odot\,yr^{-1}}$)	< -8 ($> 10^{-4}\,\mathrm{M_\odot\,yr^{-1}}$)
-1.5	4.15 (0.0052)	9.24 (0.0115)	9.68 (0.0121)
-1.7	4.24 (0.0053)	12.12 (0.0151)	13.90 (0.0174)
-1.9	4.32 (0.0054)	17.35 (0.0217)	25.00 (0.0313)
-2.1	4.45 (0.0056)	27.96 (0.0350)	63.54 (0.0794)

Table 5.1: UV luminosity densities (and star formation rate densities in parentheses) determined by integrating the derived $z \approx 7$ Schechter luminosity function down to various limiting absolute magnitudes assuming fixed $\alpha \in \{-1.5, -1.7, -1.9, -2.1\}$.

α	$\rho_{1600}\,[10^{25}\,\mathrm{erg\,s^{-1}\,Mpc^{-3}\,Hz^{-1}}]$ ($\dot{\rho}_*\,[\mathrm{M_\odot\,yr^{-1}\,Mpc^{-3}}]$)		
	$M_{1600} < -18.5$ (SFR $> 1.5\,\mathrm{M_\odot\,yr^{-1}}$)	< -13 ($> 0.01\,\mathrm{M_\odot\,yr^{-1}}$)	< -8 ($> 10^{-4}\,\mathrm{M_\odot\,yr^{-1}}$)
-1.5	1.41 (0.0018)	3.74 (0.0047)	3.95 (0.0049)
-1.7	1.45 (0.0018)	5.16 (0.0064)	6.03 (0.0075)
-1.9	1.49 (0.0019)	7.81 (0.0098)	11.62 (0.0145)
-2.1	1.56 (0.0020)	13.34 (0.0167)	31.52 (0.0394)

Table 5.2: UV luminosity densities (and star formation rate densities in parentheses) determined by integrating the derived $z \approx 8$ Schechter luminosity function down to various limiting absolute magnitudes assuming fixed $\alpha \in \{-1.5, -1.7, -1.9, -2.1\}$.

to adopt, with two possible values being the luminosity of a single OB star or of a typical HII region. As mentioned earlier, for $\alpha < -2$ the integral is divergent and would give an infinite luminosity density if integrated down to zero luminosity. Since such steep faint end slopes have been suggested (see Chapter 4), the right luminosity limit would be crucial to correctly calculate luminosity densities and SFR densities.

Figure 5.3 shows the well known Madau-Lilly diagram (Madau et al. 1996, Lilly et al. 1996) which shows the evolution of the SFR density with redshift. The results presented here at $z \approx 7 - 8$ are compared with lower redshift estimations

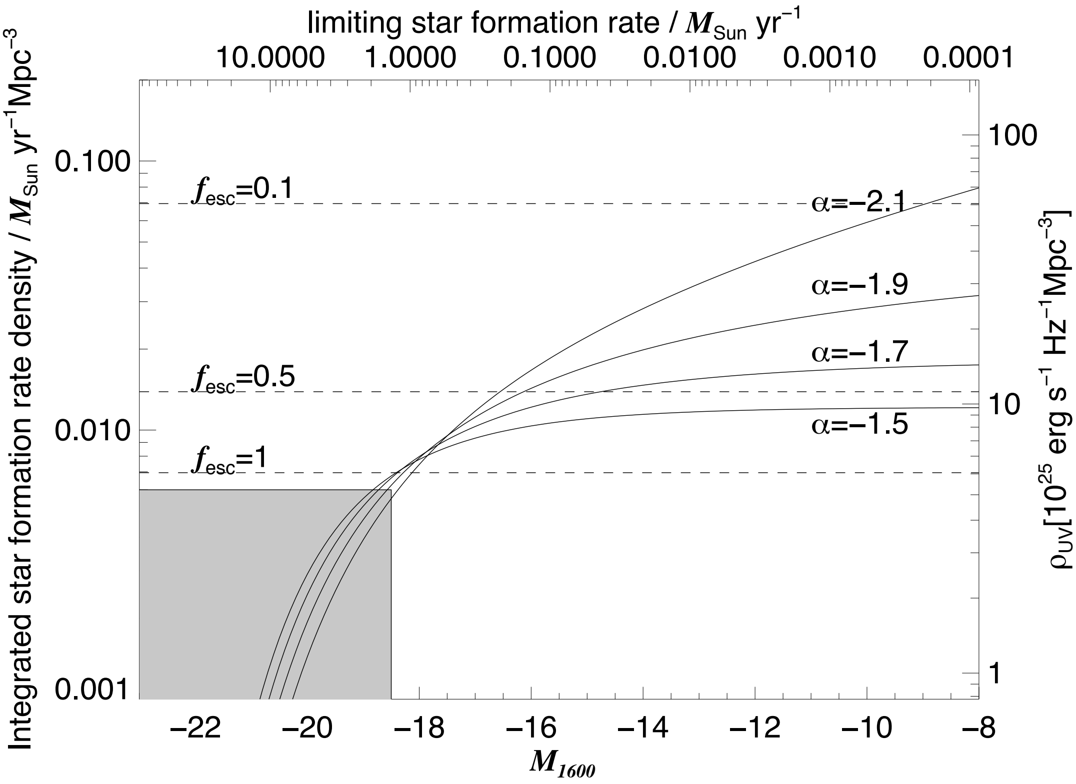

Figure 5.1: The solid lines are the total star formation rate density (left axis) or ionising flux density (right axis) inferred from the luminosity function fits for our z'-drop sample (for faint end slopes $\alpha = [-1.5, -1.7, -1.9, -2.1]$), integrating down to the limiting absolute magnitude in the rest-frame UV shown on the lower x-axis (in AB magnitudes); the upper x-axis shows the equivalent unobscured star formation rate. The dashed lines show the requirement to keep the Universe ionised at $z = 7$, using the relation from Madau, Haardt & Rees (1999) and assuming a low clumping factor of $C = 5$. We show the requirements for escape fractions of $f_{\rm esc} = 0.1$, 0.5 & 1. Where the solid lines cross the dashed lines, reionzation can be achieved. The shaded region is where the current deepest observations probe (the HUDF).

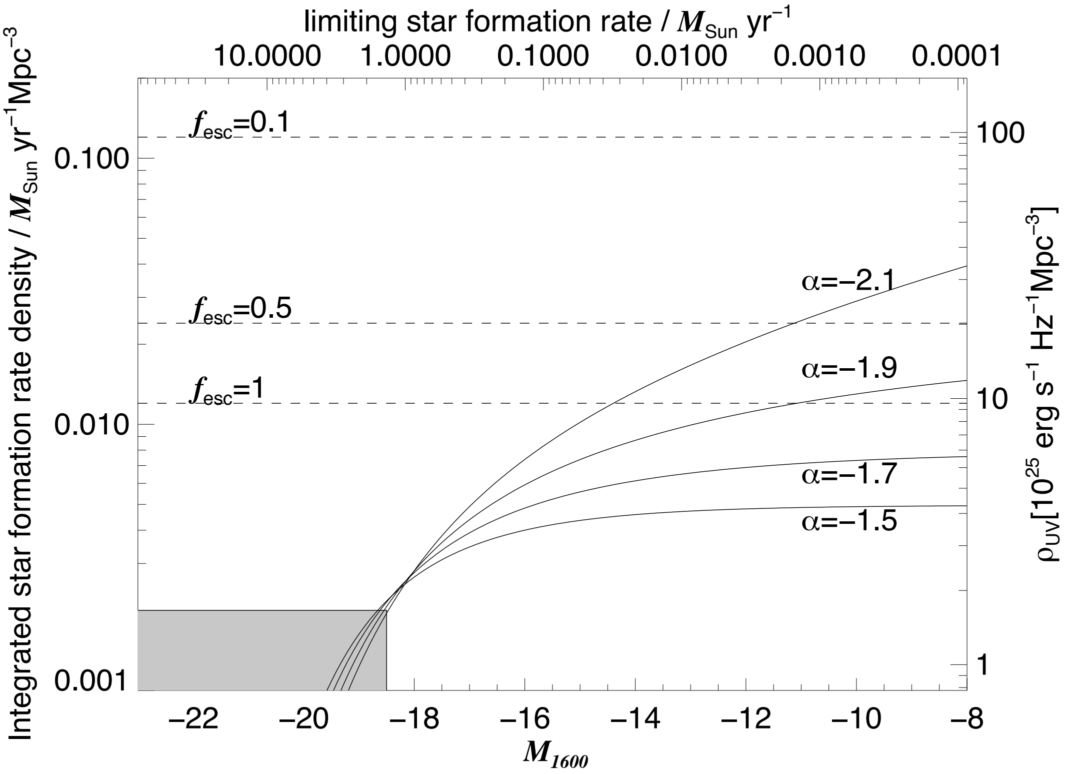

Figure 5.2: The solid lines are the total star formation rate density (left axis) or ionising flux density (right axis) inferred from the luminosity function fits for our Y-drop sample (for faint end slopes $\alpha = [-1.5, -1.7, -1.9, -2.1]$), integrating down to the limiting absolute magnitude in the rest-frame UV shown on the lower x-axis (in AB magnitudes); the upper x-axis shows the equivalent unobscured star formation rate. The dashed lines show the requirement to keep the Universe ionised at $z = 8.6$, using the relation from Madau, Haardt & Rees (1999) and assuming a low clumping factor of $C = 5$. We show the requirements for escape fractions of $f_{\rm esc} = 0.1$, 0.5 & 1. Where the solid lines cross the dashed lines, reionzation can be achieved. The shaded region is where the current deepest observations probe (the HUDF).

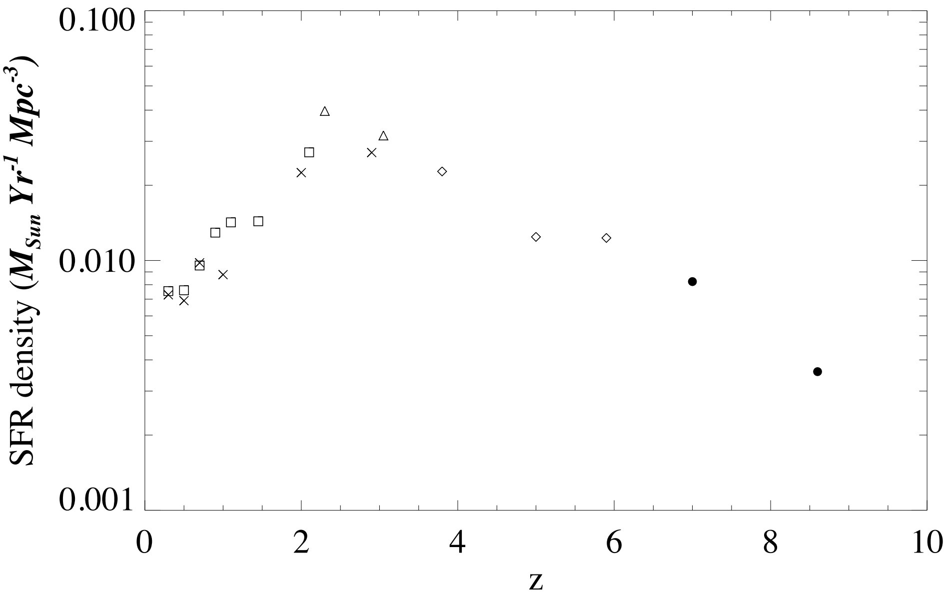

Figure 5.3: The star-formation rate density evolution with redshift. Filled circles denote the results obtained with this work, while the lower redshift estimates are derived by integrating to $0.1 \times L^*$ the UV LFs proposed by Arnouts et al. 2005 (crosses), Cucciati et al. 2012 (open squares), Reddy & Steidel 2009 (open triangles) and Bouwens et al. 2007 (open diamonds)

in the literature (Arnouts et al. 2005, Cucciati et al. 2012, Reddy & Steidel 2009 and Bouwens et al. 2007). The UV luminosity functions considered are integrated down to $0.1 \times L^*$ (where L^* is the value determined at that redshift, not the current L^* at z=0) and the $z \approx 7$ and $z \approx 8$ SFR density estimations are based on our $\alpha = -1.7$ LF determinations. From the peak between $z = 2$ and $z = 3$, the data suggest a steady decline of the SFR density with the increasing redshift (a decline in SFR density from $z \approx 3$ to $z \approx 6$ was discovered by Stanway et al. 2003) up to $z \approx 8$, where the SFR density is one order of magnitude lower than at the peak. This result is also consistent (within the considerable uncertainties) with the results of Oesch et al. (2012b), who suggest a drop in SFR density between $z \approx 8$ and $z \approx 10$.

5.0.2 Reionization

The ionizing UV (or Lyman continuum, LyC) photons produced by the most massive (OB) stars might be critical in reionization and keeping the Universe ionized at $z \approx 6 - 11$. However, work at $z \approx 6$ has shown that under standard assumptions of the IMF, escape fraction and clumping of the gas, the observed population of Lyman break galaxies produce insufficient flux down to $AB \approx 28.5\,\mathrm{mag}$ (Bunker et al. 2004).

The measured star formation rates presented earlier at $z \approx 7$ and $z \approx 8$ can be compared to those required to ionize the universe at the same redshifts. Madau, Haardt & Rees (1999) give the density of star formation required for reionization (assuming the same Salpeter IMF as used in this thesis). For this work, equation 27 of Madau, Haardt & Rees (1999) has been updated for a more recent concordance cosmology estimate of the baryon density from Larson et al. (2011), $\Omega_b\, h_{100}^2 = 0.022622$, and assumes the form:

$$\dot{\rho}_{\mathrm{SFR}} \approx \frac{0.012\, M_\odot\, \mathrm{yr}^{-1}\, \mathrm{Mpc}^{-3}}{f_{\mathrm{esc}}} \left(\frac{1+\langle z\rangle}{1+8.6}\right)^3 \left(\frac{\Omega_b\, h_{70}^2}{0.0462}\right)^2 \left(\frac{C}{5}\right) \tag{5.3}$$

Since the number of photons needed for reionization rises as $(1+z)^3$, the requirement at $z \approx 8.6$ is a factor of 2.5 times higher than that at $z \approx 6$ and 1.7 higher than at $z \approx 7$. In the above equation, $\langle z\rangle$ is the average redshift probed, 7.0 for z'-drops and 8.6 for Y-drops, and C is the clumping factor of neutral hydrogen, $C = \langle \rho_{\mathrm{HI}}^2\rangle \langle \rho_{\mathrm{HI}}\rangle^{-2}$. Early simulations suggested $C \approx 30$ (Gnedin & Ostriker 1997), but more recent work including the effects of reheating implies a lower concentration factor of $C \approx 5$ (Pawlik et al. 2009). The escape fraction of ionizing photons (f_{esc}) for high-redshift galaxies is highly uncertain (e.g., Steidel, Pettini & Adelberger 2001, Shapley et al. 2006). In the local Universe, the value of f_{esc} is low, just a few percent ($\lesssim 5\%$), but there is evidence for higher values at redshifts up to $z \approx 3$ (Inoue et al. 2006, Siana et al. 2010). f_{esc} is often measured relative to the number of escaping photons at $\lambda_{rest} = 1500$ Å (Steidel, Pettini & Adelberger 2001):

$$f_{\mathrm{esc,rel}} = \frac{(f_{1500}/f_{\mathrm{LyC}})_{\mathrm{int}}}{(f_{1500}/f_{\mathrm{LyC}})_{\mathrm{obs}}} \times \exp\left(\tau_{\mathrm{IGM}}\right) \tag{5.4}$$

where $(f_{1500}/f_{\mathrm{LyC}})_{\mathrm{int}}$ is the intrinsic ratio of non-ionizing to ionizing specific intensities, from spectral synthesis models, $(f_{1500}/f_{\mathrm{LyC}})_{\mathrm{obs}}$ is the observed flux ratio and τ_{IGM} is the IGM optical depth (for LyC photons). The relation between $f_{\mathrm{esc,rel}}$ and f_{esc} is:

$$f_{\mathrm{esc}} = f_{\mathrm{esc,rel}} \times 10^{-0.4\,A_{1500}} \tag{5.5}$$

where A_{1500} is the dust absorption at 1500Å (Vanzella et al. 2010).

Theoretical work (Hayes et al. 2011, Mitra, Ferrara & Choudhury, 2012) suggest f_{esc} values of $\sim 40\%$ at $z \approx 6$ and beyond, supporting its evolution with redshift. The escape fraction also depends on halo mass, with massive galaxies having lower escape fractions (Ricotti & Shull 2000, Wise & Cen 2009), although some other works (Gnedin et al. 2008) disagree, predicting lower f_{esc} for less massive values, and depending on other factors like morphology and star formation history. Observational determinations of Lyman continuum escape fractions are particularly difficult as expensive UV data are needed locally, and objects at high redshift are generally faint and only a few bright objects spectra can be observed. It is possible that the escape fraction of ionising photons may be linked to the escape fraction of Lyman-α photons (Stark et al. 2010), which may mean that high escape fractions could be tested through future line emission searches with spectroscopy and narrow-band imaging.

5.0.2.1 The ionizing photon density at $z \approx 7$

The star formation rate density $\dot{\rho}_{\rm SFR}$ inferred from the z'-drop selection presented in this work integrating the LF down to the approximate observation limit, $M_{UV} = -18.5$, is $\dot{\rho}_{\rm SFR} = 0.0053 M_\odot\,{\rm yr}^{-1}\,{\rm Mpc}^{-3}$ for $\alpha = -1.7$, (see Table 5.1, Figure 5.2), about 4/5 of the required $\dot{\rho}_{\rm SFR} = 0.0069 M_\odot\,{\rm yr}^{-1}\,{\rm Mpc}^{-3}$ to reionize the Universe assuming $f_{\rm esc} = 1$ (no absorption by H I). For a more reasonable value of $f_{\rm esc}$ like 0.5, the required $\dot{\rho}_{\rm SFR}$ doubles ($\sim 0.0140 M_\odot\,{\rm yr}^{-1}\,{\rm Mpc}^{-3}$) and reionization is achievable with a faint end slope $\alpha = -1.7$ (the same faint end slope found at redshifts $z = 3-6$) integrating to $M_{UV} = -13$ (i.e., extrapolating the Schechter function to ≈ 100 times fainter than our observed limit). For lower escape fractions, steeper faint end slopes and/or LF integrations to fainter cut-off luminosities are needed for reionization.

5.0.2.2 The ionizing photon density at $z \approx 8$

Even considering the implausible upper limit of $f_{\rm esc} = 1$ and a very low clumping factor, the required total star formation rate density for reionization is $0.012\,M_\odot\,{\rm yr}^{-1}\,{\rm Mpc}^{-3}$. This is a factor of ~ 5 higher than the measured star formation density at $z \approx 8-9$ from Y-drop galaxies brighter than $M_{UV} = -18.5$. As shown in Table 5.2 and Figure 5.2, the required UV luminosity density can only just be achieved (if $f_{\rm esc} = 1$) by integrating down to $M_{UV} = -13$ and then only for a steeper faint end slope of $\alpha = -1.9$ rather than $\alpha = -1.7$ (as observed at lower redshifts).

Adopting a value of $f_{\rm esc} = 0.5$ the required total star formation rate density for reionization would be $0.024\,M_\odot\,{\rm yr}^{-1}\,{\rm Mpc}^{-3}$, then the Y-drop population can only provide sufficient ionizing photons if the faint end slope is very steep ($\alpha < -1.9$) and the Schechter function is integrated down below $M_{UV} = -8$ (corresponding to a star formation rate of only $10^{-4}\,M_\odot\,{\rm yr}^{-1}$). Recent theoretical works indicate that the reionization process itself may have been "photon-starved" (e.g., Bolton & Haehnelt 2007), consistent with the extrapolation of the observational constraints presented here. It is somehow suspect that the steep UV LF faint end slopes which seem to be required at $z \geq 7$ evolve rapidly into well-constrained $\alpha = -1.7$ at $z = 3 - 6$.

Reionization by star-forming galaxies looks plausible at $z \approx 7$, where it can be achieved by reasonable values of $f_{\rm esc}$ (≤ 0.5) without invoking a very steep faint end slope for the LF ($\alpha \gtrsim -1.9$). At $z \approx 8$ it seems more complicated, as both high escape fractions and extremely steep faint end slopes are required. However, the assumption of a solar metallicity Salpeter IMF may be flawed: the colours of $z \sim 6$ i'-band drop-outs are very blue (Stanway, McMahon & Bunker 2005), with $\beta < -2$, and the recent WFC3 J- and H-band images show that the $z \approx 7$ z'-drops also have blue colours on average (Bunker et al. 2010; Bouwens et al. 2010b; Wilkins et al. 2011b). Continuous star formation with a Salpeter IMF produces a UV spectral slope of $\beta \approx -2$ if there is no dust reddening. The fact that even bluer slopes than this ($\beta < -2$) are observed could be explained through low metallicity, or a top-heavy IMF, which can produce between 3 and 10 times as many ionizing photons for the same 1600 Å UV luminosity (Schaerer 2003 – see also Stiavelli, Fall & Panagia 2004). Alternatively, some of the objects in this sample could be galaxies at the onset of star formation, or with a rising star formation rate (Verma et al. 2007), which would also lead to an underestimate of the true star formation rate from the rest-UV luminosity. The implications of the blue UV spectral slopes in $z \geq 6$ galaxies are thoroughly investigated in Wilkins et al. (2011b).

Chapter 6

Conclusions

In this thesis I have presented a list of candidate high-redshift star-forming galaxies ($z \approx 7-8$) identified with the Lyman break technique using *HST*/WFC3 near-infrared data at different depths from several recent programmes covering ~ 150 arcmin^2 in the GOODS-South area. These candidates are compared to independently derived catalogues from other groups in the same fields. In the CANDELS field, objects were selected using two different sets of colour critera to investigate the effects of the selection window choice on the final result, finding that it does not heavily influence the LF determinations. The variety of the data available, going from small, deep fields to wider and relatively shallower ones, is ideal to identify candidates over a wide range of brightness: the bright high redshift galaxy candidates found in the wider fields serve to better constrain the bright end of the luminosity function at those redshifts, and may also be more amenable to spectroscopic confirmation than the fainter ones from deep fields, which in turn allow us to put constraints on the LF at lower luminosities, although not faint enough to strongly constraint the faint end slope α.

It is confirmed that there is large evolution from $z = 3$, particularly in the bright end of the luminosity function, in the sense that there are far fewer UV-bright galaxies at $z \approx 8-9$ than in the more recent past. There is also evidence for evolution from $z = 6-7$ to $z = 8-9$, with this being consistent with most of the change occurring in M^* rather than ϕ^*, with M^* being fainter at higher redshift. A good constraint on the faint-end slope α which will potentially require deeper data over a wider field (as might be provided by NIRCAM on the James Webb Space Telescope).

The LF results at $z \approx 7$ and $z \approx 8$ are compared with previous LFs derived from WFC3 drop-out counts, finding a generally good agreement, one exception being the Yan et al. (2010) LF, which is strongly ruled out.

The candidate $z \approx 7-9$ galaxies detected have insufficient flux to reionize the Universe, and it is probable that galaxies below our detection limit provide significant UV contribution. Adopting a similar faint-end slope to that determined at $z = 3-6$ ($\alpha = -1.7$) and a Salpeter IMF, reionization can be achieved at $z \approx 7$ for $f_{\rm esc} = 0.5$ integrating down to $M_{UV} = -15$. However at $z \approx 8$, with the same values of α and $f_{\rm esc}$, the ioniziong photon budget falls short even integrating down to $M_{UV} = -8$. A steeper faint end slope and a low-metallicity population (or a top-heavy IMF) might still provide sufficient photons for star-forming galaxies to reionize the Universe, but confirmation of this might have to await the *James Webb Space Telescope.*

Bibliography

Arnouts, S.; Schiminovich, D.; Ilbert, O.; Tresse, L.; Milliard, B.; Treyer, M.; Bardelli, S.; Budavari, T.; Wyder, T. K.; Zucca, E.; Le Fvre, O.; Martin, D. C.; Vettolani, G.; Adami, C.; Arnaboldi, M.; Barlow, T.; Bianchi, L.; Bolzonella, M.; Bottini, D.; Byun, Y.-I.; Cappi, A.; Charlot, S.; Contini, T.; Donas, J.; Forster, K.; Foucaud, S.; Franzetti, P.; Friedman, P. G.; Garilli, B.; Gavignaud, I.; Guzzo, L.; Heckman, T. M.; Hoopes, C.; Iovino, A.; Jelinsky, P.; Le Brun, V.; Lee, Y.-W.; Maccagni, D.; Madore, B. F.; Malina, R.; Marano, B.; Marinoni, C.; McCracken, H. J.; Mazure, A.; Meneux, B.; Merighi, R.; Morrissey, P.; Neff, S.; Paltani, S.; Pell, R.; Picat, J. P.; Pollo, A.; Pozzetti, L.; Radovich, M.; Rich, R. M.; Scaramella, R.; Scodeggio, M.; Seibert, M.; Siegmund, O.; Small, T.; Szalay, A. S.; Welsh, B.; Xu, C. K.; Zamorani, G.; Zanichelli, A., 2005, ApJ, 619, L43

Becker, Robert H.; Fan, Xiaohui; White, Richard L.; Strauss, Michael A.; Narayanan, Vijay K.; Lupton, Robert H.; Gunn, James E.; Annis, James; Bahcall, Neta A.; Brinkmann, J.; Connolly, A. J.; Csabai, Istvn; Czarapata, Paul C.; Doi, Mamoru; Heckman, Timothy M.; Hennessy, G. S.; Ivezi?, ?eljko; Knapp, G. R.; Lamb, Don Q.; McKay, Timothy A.; Munn, Jeffrey A.; Nash, Thomas; Nichol, Robert; Pier, Jeffrey R.; Richards, Gordon T.; Schneider, Donald P.; Stoughton, Chris; Szalay, Alexander S.; Thakar, Aniruddha R.; York, D. G., 2001, AJ, 122, 2850

Beckwith, Steven V. W.; Stiavelli, Massimo; Koekemoer, Anton M.; Caldwell, John A. R.; Ferguson, Henry C.; Hook, Richard; Lucas, Ray A.; Bergeron, Louis E.; Corbin, Michael; Jogee, Shardha; Panagia, Nino; Robberto, Massimo; Royle, Patricia; Somerville, Rachel S.; Sosey, Megan, 2006, AJ, 132, 1729

Bertin, E., & Arnouts, S. 1996, AAPS, 117, 393

Bolton J. S.; Haehnelt M. G. 2007, MNRAS, 382, 325

Bouwens, R. J.; Illingworth, G. D.; Thompson, R. I.; Blakeslee, J. P.; Dickinson, M. E.; Broadhurst, T. J.; Eisenstein, D. J.; Fan, X.; Franx, M.; Meurer, G.; van Dokkum, P.,s 2004, ApJ, 606, L25

Bouwens R. J. Illingworth G. D. Blakeslee J. P.; Franx M., 2006, ApJ, 653, 53

Bouwens R. J.; Illingworth G. D.; Franx M.; Ford H., 2007, ApJ, 670, 928

Bouwens, R. J.; Illingworth, G. D.; Oesch, P. A.; Stiavelli, M.; van Dokkum, P.; Trenti, M.; Magee, D.; Labb, I.; Franx, M.; Carollo, C. M.; Gonzalez, V., 2010a, ApJ, 709, L133

Bouwens, Rychard J.; Illingworth, Garth D.; Gonzlez, Valentino; Labb, Ivo; Franx, Marijn; Conselice, Christopher J.; Blakeslee, John; van Dokkum, Pieter; Holden, Brad; Magee, Dan; Marchesini, Danilo; Zheng, Wei, 2010b, ApJ, 708, L69

Bouwens, R. J.; Illingworth, G. D.; Labbe, I.; Oesch, P. A.; Trenti, M.; Carollo, C. M.; van Dokkum, P. G.; Franx, M.; Stiavelli, M.; Gonzlez, V.; Magee, D.; Bradley, L. 2011, Nature, 469, 504

Bradley, L. D.; Trenti, M.; Oesch, P. A.; Stiavelli, M.; Treu, T.; Bouwens, R. J.; Shull, J. M.; Holwerda, B. W.; Pirzkal, N., 2012, ApJ, 760, 108

Bunker A. J., Stanway E. R., Ellis R. S., McMahon R. G., 2004, MNRAS, 355, 374

Bunker A., Wilkins S., 2009, arXiv:0912:1351

Bunker, Andrew J.; Wilkins, Stephen; Ellis, Richard S.; Stark, Daniel P.; Lorenzoni, Silvio; Chiu, Kuenley; Lacy, Mark; Jarvis, Matt J.; Hickey, Samantha, 2010, MNRAS, 409, 855

Casertano, Stefano; de Mello, Dulia; Dickinson, Mark; Ferguson, Henry C.; Fruchter, Andrew S.; Gonzalez-Lopezlira, Rosa A.; Heyer, Inge; Hook, Richard N.; Levay, Zolt; Lucas, Ray A.; Mack, Jennifer; Makidon, Russell B.; Mutchler, Max; Smith, T. Ed; Stiavelli, Massimo; Wiggs, Michael S.; Williams, Robert E., 2000, AJ, 120, 2747

Capak, Peter L.; Riechers, Dominik; Scoville, Nick Z.; Carilli, Chris; Cox, Pierre; Neri, Roberto; Robertson, Brant; Salvato, Mara; Schinnerer, Eva; Yan, Lin; Wilson, Grant W.; Yun, Min; Civano, Francesca; Elvis, Martin; Karim, Alexander; Mobasher, Bahram; Staguhn, Johannes G., 2011, Nature, 470, 233

Castellano, M.; Fontana, A.; Paris, D.; Grazian, A.; Pentericci, L.; Boutsia, K.; Santini, P.; Testa, V.; Dickinson, M.; Giavalisco, M.; Bouwens, R.; Cuby, J.-G.;

Mannucci, F.; Clment, B.; Cristiani, S.; Fiore, F.; Gallozzi, S.; Giallongo, E.; Maiolino, R.; Menci, N.; Moorwood, A.; Nonino, M.; Renzini, A.; Rosati, P.; Salimbeni, S.; Vanzella, E., 2010, AAP, 524, A28

Cirasuolo, M.; McLure, R. J.; Dunlop, J. S.; Almaini, O.; Foucaud, S.; Smail, Ian; Sekiguchi, K.; Simpson, C.; Eales, S.; Dye, S.; Watson, M. G.; Page, M. J.; Hirst, P., 2007, MNRAS, 380, 585

Cucciati, O.; Tresse, L.; Ilbert, O.; Le Fvre, O.; Garilli, B.; Le Brun, V.; Cassata, P.; Franzetti, P.; Maccagni, D.; Scodeggio, M.; Zucca, E.; Zamorani, G.; Bardelli, S.; Bolzonella, M.; Bielby, R. M.; McCracken, H. J.; Zanichelli, A.; Vergani, D., 2012, AAP, 539, A31

Davis, M.; Guhathakurta, P.; Konidaris, N. P.; Newman, J. A.; Ashby, M. L. N.; Biggs, A. D.; Barmby, P.; Bundy, K.; Chapman, S. C.; Coil, A. L.; Conselice, C. J.; Cooper, M. C.; Croton, D. J.; Eisenhardt, P. R. M.; Ellis, R. S.; Faber, S. M.; Fang, T.; Fazio, G. G.; Georgakakis, A.; Gerke, B. F.; Goss, W. M.; Gwyn, S.; Harker, J.; Hopkins, A. M.; Huang, J.-S.; Ivison, R. J.; Kassin, S. A.; Kirby, E. N.; Koekemoer, A. M.; Koo, D. C.; Laird, E. S.; Le Floc'h, E.; Lin, L.; Lotz, J. M.; Marshall, P. J.; Martin, D. C.; Metevier, A. J.; Moustakas, L. A.; Nandra, K.; Noeske, K. G.; Papovich, C.; Phillips, A. C.; Rich, R. M.; Rieke, G. H.; Rigopoulou, D.; Salim, S.; Schiminovich, D.; Simard, L.; Smail, I.; Small, T. A.; Weiner, B. J.; Willmer, C. N. A.; Willner, S. P.; Wilson, G.; Wright, E. L.; Yan, R, 2007, ApJ, 660, L1

Dunkley, J.; Spergel, D. N.; Komatsu, E.; Hinshaw, G.; Larson, D.; Nolta, M. R.; Odegard, N.; Page, L.; Bennett, C. L.; Gold, B.; Hill, R. S.; Jarosik, N.;

Weiland, J. L.; Halpern, M.; Kogut, A.; Limon, M.; Meyer, S. S.; Tucker, G. S.; Wollack, E.; Wright, E. L., 2009, ApJS, 180, 306

Fan, Xiaohui; Narayanan, Vijay K.; Lupton, Robert H.; Strauss, Michael A.; Knapp, Gillian R.; Becker, Robert H.; White, Richard L.; Pentericci, Laura; Leggett, S. K.; Haiman, Zoltn; Gunn, James E.; Ivezic, Zeljko; Schneider, Donald P.; Anderson, Scott F.; Brinkmann, J.; Bahcall, Neta A.; Connolly, Andrew J.; Csabai, Istvn; Doi, Mamoru; Fukugita, Masataka; Geballe, Tom; Grebel, Eva K.; Harbeck, Daniel; Hennessy, Gregory; Lamb, Don Q.; Miknaitis, Gajus; Munn, Jeffrey A.; Nichol, Robert; Okamura, Sadanori; Pier, Jeffrey R.; Prada, Francisco; Richards, Gordon T.; Szalay, Alex; York, Donald G., 2001, AJ, 122, 2833

Fan, Xiaohui; Strauss, Michael A.; Becker, Robert H.; White, Richard L.; Gunn, James E.; Knapp, Gillian R.; Richards, Gordon T.; Schneider, Donald P.; Brinkmann, J.; Fukugita, Masataka, 2006, AJ, 132, 117

Ferguson, Henry C.; Dickinson, Mark; Giavalisco, Mauro; Kretchmer, Claudia; Ravindranath, Swara; Idzi, Rafal; Taylor, Edward; Conselice, Christopher J.; Fall, S. Michael; Gardner, Jonathan P.; Livio, Mario; Madau, Piero; Moustakas, Leonidas A.; Papovich, Casey M.; Somerville, Rachel S.; Spinrad, Hyron; Stern, Daniel, 2004, ApJ, 600, 107

Finkelstein, S. L., Papovich, C., Giavalisco, M., Reddy, N. A., Ferguson, H. C., Koekemoer, A. M., & Dickinson, M. 2010, ApJ, 719, 1250

Finkelstein, Steven L.; Papovich, Casey; Ryan, Russell E.; Pawlik, Andreas H.; Dickinson, Mark; Ferguson, Henry C.; Finlator, Kristian; Koekemoer, Anton

M.; Giavalisco, Mauro; Cooray, Asantha; Dunlop, James S.; Faber, Sandy M.; Grogin, Norman A.; Kocevski, Dale D.; Newman, Jeffrey A., 2012, ApJ, 758, 93

Fioc, M., & Rocca-Volmerange, B. 1997, AAP, 326, 950

Fruchter, A., & Hook, R. N. 1997, SPIE, 3164, 120

Giacconi, Riccardo; Zirm, Andrew; Wang, JunXian; Rosati, Piero; Nonino, Mario; Tozzi, Paolo; Gilli, Roberto; Mainieri, Vincenzo; Hasinger, Guenther; Kewley, Lisa; Bergeron, Jacqueline; Borgani, Stefano; Gilmozzi, Roberto; Grogin, Norman; Koekemoer, Anton; Schreier, Ethan; Zheng, Wei; Norman, Colin, 2002, ApJS, 139, 369

Giavalisco, M.; Dickinson, M.; Ferguson, H. C.; Ravindranath, S.; Kretchmer, C.; Moustakas, L. A.; Madau, P.; Fall, S. M.; Gardner, Jonathan P.; Livio, M.; Papovich, C.; Renzini, A.; Spinrad, H.; Stern, D.; Riess, A., 2004, ApJ, 600, L103

Gilliland, R. L. 2005, Instrument Science Report TEL 2005-02, 23 pages, 2

Gnedin, N. Y., & Ostriker, J. P. 1997, ApJ, 486, 581

Gnedin, N. Y., Kravtsov, A. V., & Chen, H.-W. 2008, ApJ, 672, 765

Grazian, A.; Castellano, M.; Fontana, A.; Pentericci, L.; Dunlop, J. S.; McLure, R. J.; Koekemoer, A. M.; Dickinson, M. E.; Faber, S. M.; Ferguson, H. C.; Galametz, A.; Giavalisco, M.; Grogin, N. A.; Hathi, N. P.; Kocevski, D. D.; Lai, K.; Newman, J. A.; Vanzella, E., 2012, AAP, 547, A51

Grogin, Norman A.; Kocevski, Dale D.; Faber, S. M.; Ferguson, Henry C.; Koekemoer, Anton M.; Riess, Adam G.; Acquaviva, Viviana; Alexander, David M.; Almaini, Omar; Ashby, Matthew L. N.; Barden, Marco; Bell, Eric F.; Bournaud, Frdric; Brown, Thomas M.; Caputi, Karina I.; Casertano, Stefano; Cassata, Paolo; Castellano, Marco; Challis, Peter; Chary, Ranga-Ram; Cheung, Edmond; Cirasuolo, Michele; Conselice, Christopher J.; Roshan Cooray, Asantha; Croton, Darren J.; Daddi, Emanuele; Dahlen, Tomas; Dav, Romeel; de Mello, Dulia F.; Dekel, Avishai; Dickinson, Mark; Dolch, Timothy; Donley, Jennifer L.; Dunlop, James S.; Dutton, Aaron A.; Elbaz, David; Fazio, Giovanni G.; Filippenko, Alexei V.; Finkelstein, Steven L.; Fontana, Adriano; Gardner, Jonathan P.; Garnavich, Peter M.; Gawiser, Eric; Giavalisco, Mauro; Grazian, Andrea; Guo, Yicheng; Hathi, Nimish P.; Hussler, Boris; Hopkins, Philip F.; Huang, Jia-Sheng; Huang, Kuang-Han; Jha, Saurabh W.; Kartaltepe, Jeyhan S.; Kirshner, Robert P.; Koo, David C.; Lai, Kamson; Lee, Kyoung-Soo; Li, Weidong; Lotz, Jennifer M.; Lucas, Ray A.; Madau, Piero; McCarthy, Patrick J.; McGrath, Elizabeth J.; McIntosh, Daniel H.; McLure, Ross J.; Mobasher, Bahram; Moustakas, Leonidas A.; Mozena, Mark; Nandra, Kirpal; Newman, Jeffrey A.; Niemi, Sami-Matias; Noeske, Kai G.; Papovich, Casey J.; Pentericci, Laura; Pope, Alexandra; Primack, Joel R.; Rajan, Abhijith; Ravindranath, Swara; Reddy, Naveen A.; Renzini, Alvio; Rix, Hans-Walter; Robaina, Aday R.; Rodney, Steven A.; Rosario, David J.; Rosati, Piero; Salimbeni, Sara; Scarlata, Claudia; Siana, Brian; Simard, Luc; Smidt, Joseph; Somerville, Rachel S.; Spinrad, Hyron; Straughn, Amber N.; Strolger, Louis-Gregory; Telford, Olivia; Teplitz, Harry I.; Trump, Jonathan R.; van der Wel, Arjen; Villforth, Carolin; Wechsler, Risa H.; Weiner, Benjamin J.; Wiklind, Tommy; Wild, Vivienne; Wilson, Grant; Wuyts, Stijn; Yan, Hao-Jing; Yun, Min S., 2011, ApJS, 197, 35

Guhathakurta, P., Tyson, J. A., & Majewski, S. R. 1990, ApJ, 357, L9

Gunn, J. E., & Peterson, B. A. 1965, ApJ, 142, 1633

Hayes, Matthew; Schaerer, Daniel; stlin, Gran; Mas-Hesse, J. Miguel; Atek, Hakim; Kunth, Daniel, 2011, ApJ, 730, 8

Inoue, A. K., Iwata, I., & Deharveng, J.-M. 2006, MNRAS, 371, L1

Kashikawa, Nobunari; Shimasaku, Kazuhiro; Yasuda, Naoki; Ajiki, Masaru; Akiyama, Masayuki; Ando, Hiroyasu; Aoki, Kentaro; Doi, Mamoru; Fujita, Shinobu S.; Furusawa, Hisanori; Hayashino, Tomoki; Iwamuro, Fumihide; Iye, Masanori; Karoji, Hiroshi; Kobayashi, Naoto; Kodaira, Keiichi; Kodama, Tadayuki; Komiyama, Yutaka; Matsuda, Yuichi; Miyazaki, Satoshi; Mizumoto, Yoshihiko; Morokuma, Tomoki; Motohara, Kentaro; Murayama, Takashi; Nagao, Tohru; Nariai, Kyoji; Ohta, Kouji; Okamura, Sadanori; Ouchi, Masami; Sasaki, Toshiyuki; Sato, Yasunori; Sekiguchi, Kazuhiro; Shioya, Yasunori; Tamura, Hajime; Taniguchi, Yoshiaki; Umemura, Masayuki; Yamada, Toru; Yoshida, Makiko, 2004, PASJ, 56, 1011

Kennicutt, R. C., 1998, ARA&A, 36, 189

Koekemoer, A. M., Fruchter, A. S., Hook, R. N., & Hack, W. 2003, HST Calibration Workshop : Hubble after the Installation of the ACS and the NICMOS Cooling System, 337

Koekemoer, Anton M.; Faber, S. M.; Ferguson, Henry C.; Grogin, Norman A.; Kocevski, Dale D.; Koo, David C.; Lai, Kamson; Lotz, Jennifer M.; Lucas, Ray A.; McGrath, Elizabeth J.; Ogaz, Sara; Rajan, Abhijith; Riess, Adam G.; Rodney, Steve A.; Strolger, Louis; Casertano, Stefano; Castellano, Marco; Dahlen, Tomas; Dickinson, Mark; Dolch, Timothy; Fontana, Adriano; Giavalisco, Mauro; Grazian, Andrea; Guo, Yicheng; Hathi, Nimish P.; Huang, Kuang-Han; van der Wel, Arjen; Yan, Hao-Jing; Acquaviva, Viviana; Alexander, David M.; Almaini, Omar; Ashby, Matthew L. N.; Barden, Marco; Bell, Eric F.; Bournaud, Frdric; Brown, Thomas M.; Caputi, Karina I.; Cassata, Paolo; Challis, Peter J.; Chary, Ranga-Ram; Cheung, Edmond; Cirasuolo, Michele; Conselice, Christopher J.; Roshan Cooray, Asantha; Croton, Darren J.; Daddi, Emanuele; Dav, Romeel; de Mello, Duilia F.; de Ravel, Loic; Dekel, Avishai; Donley, Jennifer L.; Dunlop, James S.; Dutton, Aaron A.; Elbaz, David; Fazio, Giovanni G.; Filippenko, Alexei V.; Finkelstein, Steven L.; Frazer, Chris; Gardner, Jonathan P.; Garnavich, Peter M.; Gawiser, Eric; Gruetzbauch, Ruth; Hartley, Will G.; Hussler, Boris; Herrington, Jessica; Hopkins, Philip F.; Huang, Jia-Sheng; Jha, Saurabh W.; Johnson, Andrew; Kartaltepe, Jeyhan S.; Khostovan, Ali A.; Kirshner, Robert P.; Lani, Caterina; Lee, Kyoung-Soo; Li, Weidong; Madau, Piero; McCarthy, Patrick J.; McIntosh, Daniel H.; McLure, Ross J.; McPartland, Conor; Mobasher, Bahram; Moreira, Heidi; Mortlock, Alice; Moustakas, Leonidas A.; Mozena, Mark; Nandra, Kirpal; Newman, Jeffrey A.; Nielsen, Jennifer L.; Niemi, Sami; Noeske, Kai G.; Papovich, Casey J.; Pentericci, Laura; Pope, Alexandra; Primack, Joel R.; Ravindranath, Swara; Reddy, Naveen A.; Renzini, Alvio; Rix, Hans-Walter; Robaina, Aday R.; Rosario, David J.; Rosati, Piero; Salimbeni, Sara; Scarlata, Claudia; Siana, Brian; Simard, Luc; Smidt, Joseph; Snyder, Diana; Somerville, Rachel S.; Spinrad, Hyron; Straughn, Amber N.; Telford, Olivia; Teplitz, Harry I.; Trump, Jonathan R.; Vargas, Carlos; Villforth, Carolin; Wagner, Cory R.; Wandro, Pat; Wechsler, Risa H.; Weiner, Benjamin J.; Wiklind, Tommy; Wild, Vivienne; Wilson, Grant; Wuyts, Stijn; Yun, Min S., 2011, ApJS, 197, 36

Knapp, G. R.; Leggett, S. K.; Fan, X.; Marley, M. S.; Geballe, T. R.; Golimowski, D. A.; Finkbeiner, D.; Gunn, J. E.; Hennawi, J.; Ivezi?, Z.; Lupton, R. H.; Schlegel, D. J.; Strauss, M. A.; Tsvetanov, Z. I.; Chiu, K.; Hoversten, E. A.; Glazebrook, K.; Zheng, W.; Hendrickson, M.; Williams, C. C.; Uomoto, A.; Vrba, F. J.; Henden, A. A.; Luginbuhl, C. B.; Guetter, H. H.; Munn, J. A.; Canzian, B.; Schneider, Donald P.; Brinkmann, J., 2004, AJ, 127, 3553

Larson, D.; Dunkley, J.; Hinshaw, G.; Komatsu, E.; Nolta, M. R.; Bennett, C. L.; Gold, B.; Halpern, M.; Hill, R. S.; Jarosik, N.; Kogut, A.; Limon, M.; Meyer, S. S.; Odegard, N.; Page, L.; Smith, K. M.; Spergel, D. N.; Tucker, G. S.; Weiland, J. L.; Wollack, E.; Wright, E. L., 2011, ApJS, 192, 16

Lawrence, A.; Warren, S. J.; Almaini, O.; Edge, A. C.; Hambly, N. C.; Jameson, R. F.; Lucas, P.; Casali, M.; Adamson, A.; Dye, S.; Emerson, J. P.; Foucaud, S.; Hewett, P.; Hirst, P.; Hodgkin, S. T.; Irwin, M. J.; Lodieu, N.; McMahon, R. G.; Simpson, C.; Smail, I.; Mortlock, D.; Folger, M., 2007, MNRAS, 379, 1599

Leitherer, C., & Heckman, T. M. 1995, ApJS, 96, 9

Leitherer, Claus; Schaerer, Daniel; Goldader, Jeffrey D.; Gonzlez Delgado, Rosa

M.; Robert, Carmelle; Kune, Denis Foo; de Mello, Dulia F.; Devost, Daniel; Heckman, Timothy M., 1999, ApJS, 123, 3

Lilly, S. J., Le Fevre, O., Hammer, F., & Crampton, D. 1996, ApJ, 460, L1

Lorenzoni, Silvio; Bunker, Andrew J.; Wilkins, Stephen M.; Stanway, Elizabeth R.; Jarvis, Matt J.; Caruana, Joseph, 2011, MNRAS, 414, 1455

Lorenzoni, Silvio; Bunker, Andrew J.; Wilkins, Stephen M.; Caruana, Joseph; Stanway, Elizabeth R.; Jarvis, Matt J., 2012, MNRAS *in press*

Madau, P. 1995, ApJ, 441, 18

Madau, Piero; Ferguson, Henry C.; Dickinson, Mark E.; Giavalisco, Mauro; Steidel, Charles C.; Fruchter, Andrew, et al. 1996, MNRAS, 283, 1388

Madau P., Pozzetti L., Dickinson M., 1998, ApJ, 498, 106

Madau P., Haardt F., Rees M., 1999, ApJ, 514, 648

McLure, R. J., Dunlop, J. S., Cirasuolo, M., Koekemoer, A. M., Sabbi, E., Stark, D. P., Targett, T. A., & Ellis, R. S. 2010, MNRAS, 403, 960

Mitra, S., Ferrara, A., & Choudhury, T. R. 2012, MNRAS, L1

Oke J. B., Gunn J. E., 1983, ApJ, 266, 713

Oesch, P. A.; Stiavelli, M.; Carollo, C. M.; Bergeron, L. E.; Koekemoer, A. M.; Lucas, R. A.; Pavlovsky, C. M.; Trenti, M.; Lilly, S. J.; Beckwith, S. V. W.; Dahlen, T.; Ferguson, H. C.; Gardner, Jonathan P.; Lacey, C.; Mobasher, B.; Panagia, N.; Rix, H.-W., 2007, ApJ, 671, 1212

Oesch, P. A.; Carollo, C. M.; Stiavelli, M.; Trenti, M.; Bergeron, L. E.; Koekemoer, A. M.; Lucas, R. A.; Pavlovsky, C. M.; Beckwith, S. V. W.; Dahlen, T.; Ferguson, H. C.; Gardner, Jonathan P.; Lilly, S. J.; Mobasher, B.; Panagia, N., 2009, ApJ 690, 1350

Oesch, P. A.; Bouwens, R. J.; Carollo, C. M.; Illingworth, G. D.; Trenti, M.; Stiavelli, M.; Magee, D.; Labb, I.; Franx, M., 2010, ApJ, 709, L21

Oesch, P. A.; Bouwens, R. J.; Illingworth, G. D.; Labb, I.; Trenti, M.; Gonzalez, V.; Carollo, C. M.; Franx, M.; van Dokkum, P. G.; Magee, D.,2012, ApJ, 745, 110

Oesch, P. A.; Bouwens, R. J.; Illingworth, G. D.; Gonzalez, V.; Trenti, M.; van Dokkum, P. G.; Franx, M.; Labb, I.; Carollo, C. M.; Magee, D., 2012, ApJ, 759, 135

Ouchi, Masami; Mobasher, Bahram; Shimasaku, Kazuhiro; Ferguson, Henry C.; Fall, S. Michael; Ono, Yoshiaki; Kashikawa, Nobunari; Morokuma, Tomoki; Nakajima, Kimihiko; Okamura, Sadanori; Dickinson, Mark; Giavalisco, Mauro; Ohta, Kouji, 2009, ApJ, 706, 1136

Pawlik, A. H., Schaye, J., & van Scherpenzeel, E. 2009, MNRAS, 394, 1812

Reddy, N. A., & Steidel, C. C. 2009, ApJ, 692, 778

Ricotti, M., & Shull, J. M. 2000, ApJ, 542, 548

Salpeter E. E., 1955, ApJ, 121, 161

Scalo, J. M. 1986, Fundamentals of Cosmic Physics, 11, 1

Schaerer, D., 2003, A&A, 397, 527

Schechter, P. 1976, ApJ, 203, 297

Schlegel D. J., Finkbeiner D. P., Davis M., 1998, ApJ, 500, 525

Scoville, N.; Aussel, H.; Brusa, M.; Capak, P.; Carollo, C. M.; Elvis, M.; Giavalisco, M.; Guzzo, L.; Hasinger, G.; Impey, C.; Kneib, J.-P.; LeFevre, O.; Lilly, S. J.; Mobasher, B.; Renzini, A.; Rich, R. M.; Sanders, D. B.; Schinnerer, E.; Schminovich, D.; Shopbell, P.; Taniguchi, Y.; Tyson, N. D., 2007, ApJS, 172, 1

Shapley, A. E., Steidel, C. C., Pettini, M., Adelberger, K. L., & Erb, D. K. 2006, ApJ, 651, 688

Siana, Brian; Teplitz, Harry I.; Ferguson, Henry C.; Brown, Thomas M.; Giavalisco, Mauro; Dickinson, Mark; Chary, Ranga-Ram; de Mello, Duilia F.; Conselice, Christopher J.; Bridge, Carrie R.; Gardner, Jonathan P.; Colbert, James W.; Scarlata, Claudia, 2010, ApJ, 723, 241

Stanway E. R., Bunker A. J., McMahon R. G., 2003, MNRAS, 342, 439

Stanway, Elizabeth R.; Bunker, Andrew J.; McMahon, Richard G.; Ellis, Richard S.; Treu, Tommaso; McCarthy, Patrick J., 2004, ApJ, 607, 704

Stanway E. R., McMahon R. G., Bunker A. J., 2005, MNRAS, 359, 1184

Stark, D. P., Ellis, R. S., Chiu, K., Ouchi, M., Bunker, A. J. 2010 arXiv:1003.5244

Steidel, C. C., & Hamilton, D. 1992, AJ, 104, 941

Steidel C. C., Giavalisco M., Pettini M., Dickinson M., Adelberger K. L., 1996, ApJ, 462, 17

Steidel C. C., Adelberger K. L., Giavalisco M., Dickinson M., Pettini M., 1999, ApJ, 519, 1

Steidel, C. C., Pettini, M., & Adelberger, K. L. 2001, ApJ, 546, 665

Stiavelli, M., Fall, S. M., & Panagia, N. 2004, ApJ, 610, L1

Tanvir, N. R.; Fox, D. B.; Levan, A. J.; Berger, E.; Wiersema, K.; Fynbo, J. P. U.; Cucchiara, A.; Krhler, T.; Gehrels, N.; Bloom, J. S.; Greiner, J.; Evans, P. A.; Rol, E.; Olivares, F.; Hjorth, J.; Jakobsson, P.; Farihi, J.; Willingale, R.; Starling, R. L. C.; Cenko, S. B.; Perley, D.; Maund, J. R.; Duke, J.; Wijers, R. A. M. J.; Adamson, A. J.; Allan, A.; Bremer, M. N.; Burrows, D. N.; Castro-Tirado, A. J.; Cavanagh, B.; de Ugarte Postigo, A.; Dopita, M. A.; Fatkhullin, T. A.; Fruchter, A. S.; Foley, R. J.; Gorosabel, J.; Kennea, J.; Kerr, T.; Klose, S.; Krimm, H. A.; Komarova, V. N.; Kulkarni, S. R.; Moskvitin, A. S.; Mundell, C. G.; Naylor, T.; Page, K.; Penprase, B. E.; Perri, M.; Podsiadlowski, P.; Roth, K.; Rutledge, R. E.; Sakamoto, T.; Schady, P.; Schmidt, B. P.; Soderberg, A. M.; Sollerman, J.; Stephens, A. W.; Stratta, G.; Ukwatta, T. N.; Watson, D.; Westra, E.; Wold, T.; Wolf, C., 2009, Nature, 461, 1254

Trenti, M.; Bradley, L. D.; Stiavelli, M.; Oesch, P.; Treu, T.; Bouwens, R. J.; Shull, J. M.; MacKenty, J. W.; Carollo, C. M.; Illingworth, G. D., 2011, ApJ, 727, L39

Vanzella, E.; Giavalisco, M.; Inoue, A. K.; Nonino, M.; Fontanot, F.; Cristiani, S.; Grazian, A.; Dickinson, M.; Stern, D.; Tozzi, P.; Giallongo, E.; Ferguson, H.; Spinrad, H.; Boutsia, K.; Fontana, A.; Rosati, P.; Pentericci, L., 2010, ApJ, 725, 1011

Wilkins, S. M., Bunker, A. J., Ellis, R. S., Stark, D., Stanway, E. R., Chiu, K., Lorenzoni, S., & Jarvis, M. J. 2010a, MNRAS, 403, 938

Wilkins, S. M., Bunker, A. J., Lorenzoni, S., & Caruana, J., 2010b, arXiv:1002.4866

Wilkins, S. M., Bunker, A. J., Lorenzoni, S., & Caruana, J. 2011, MNRAS, 411, 23

Wilkins, S. M., Bunker, A. J., Stanway, E., Lorenzoni, S., & Caruana, J. 2011, MNRAS, 417, 717

Wise, J. H., & Cen, R. 2009, ApJ, 693, 984

Woosley, S. E., & Bloom, J. S. 2006, ARAA, 44, 507

Yan, H., Windhorst, R., Hathi, N., Cohen, S., Ryan, R., O'Connell, R., & McCarthy, P. 2010, RAA, 10, 867

Yan, H., & Project, H. 2011, Bulletin of the American Astronomical Society, 43, #128.05

Yan, Haojing; Finkelstein, Steven L.; Huang, Kuang-Han; Ryan, Russell E.; Ferguson, Henry C.; Koekemoer, Anton M.; Grogin, Norman A.; Dickinson, Mark; Newman, Jeffrey A.; Somerville, Rachel S.; Dave, Romeel; Faber, S. M.; Papovich, Casey; Guo, Yicheng; Giavalisco, Mauro; Lee, Kyoung-soo; Reddy, Naveen; Cooray, Asantha R.; Siana, Brian D.; Hathi, Nimish P.; Fazio, Giovanni G.; Ashby, Matthew; Weiner, Benjamin J.; Lucas, Ray A.; Dekel, Avishai; Pentericci, Laura; Conselice, Christopher J.; Kocevski, Dale D.; Lai, Kamson, 2011, arXiv:1112.6406

Verma, A., Lehnert, M. D., Förster Schreiber, N. M., Bremer, M. N., & Douglas, L. 2007, MNRAS, 377, 1024